EFFECT OF MODIFICATION METHODS ON USY ZEOLITE PROPERTIES AND ITS HYDROCRACKING PERFORMANCE

JOSE LUIS AGUDELO VALDERRAMA

UNIVERSIDAD INDUSTRIAL DE SANTANDER
ESCUELA DE INGENIERIA QUIMICA
CENTRO DE INVESTIGACIONES EN CATALISIS (CICAT)
BUCARAMANGA
2015

EFFECT OF MODIFICATION METHODS ON USY ZEOLITE PROPERTIES AND ITS HYDROCRACKING PERFORMANCE

JOSE LUIS AGUDELO VALDERRAMA

Submitted to the School of Chemical Engineering in partial fulfillment of the requirements for the degree of Doctor in Chemical Engineering

Director
Prof. Sonia A. Giraldo Duarte
Universidad Industrial de Santander
Codirector
Dr. Luis Javier Hoyos Marín
Instituto Colombiano del Petróleo

UNIVERSIDAD INDUSTRIAL DE SANTANDER
ESCUELA DE INGENIERIA QUIMICA
CENTRO DE INVESTIGACIONES EN CATALISIS (CICAT)
BUCARAMANGA
2015

DEDICATION

To my loved family: my mother Rosalba, my father Manuel (in heaven), my brothers Wbeimar, Armando and Andres, and my sister Leidy. They create the force that moves me.

ACKNOWLEDGMENTS

This PhD thesis has implied a meaningful life experience to me. Some people were directly and indirectly involved in this process giving me their support. The following few words are to express my gratitude to them.

I thank Professor Sonia A. Giraldo for her guidance along these four years and for her respectful treat to me. She is an admirable woman. I thank Professor Aristóbulo Centento (R.I.P) for encouraging me at the beginning of my PhD studies. I will never forget his instructions and advices. I also thank Doctor Luis Javier Hoyos for his technical advises and critical comments along the project.

I thank Professor Emiel Hensen for giving me the opportunity to carry out my doctoral stay at his group. I strongly appreciate his assistance and professionalism. The time in Eindhoven was highly fruitful for my thesis. The help given by Christiaan, Brahim, Lingqian, Xiaochun, Lennard, Tiny and the others colleagues form the TUE group is deeply acknowledged. I also thank the friendship shared by Xuefang, Guanna, Yi, Giri, Kaitu and Xiaoming.

The help provided by the people from the Pilots Plants and the laboratories of the Colombian Institute of Petroleum is appreciated. In particular, I thank Saidé, Sergio, Reynaldo, Luz Marina, Liney, Jhon Vallejo, Ingrid Bibiana Ramírez, Jaqueline Saavedra, Carlos Medina, Marisol Villamizar, Angélica Carreño, Beatriz Murcia, Maribel Castañeda, Alexander Guzman and David Pérez.

I thank my PhD partners Yuly, Diana, Kelly and Carlos for all their help and advice along the whole process. I also thank the CICAT groupmates for their permanent support, in particular to Edwing, Ivan, Mauricio and Victor.

I acknowledge the financial support provided by COLCIENCIAS and ECOPETROL S.A. for the development of the present thesis.

Finally, I thank all my friends from Piedecuesta and my relatives that continuously encouraged me to persevere in this journey.

TABLE OF CONTENTS

Pag.

2.3.7.2. UV–Vis DRS……..……...……...50
2.3.7.3. Laser Raman spectroscopy (LRS)……..…….…….....51
2.3.7.4. XPS spectroscopy of sulfided NiMoP catalysts..……..…..…….53
2.3.8. Hydrocracking activity of NiMoP-supported catalysts……..…..……..56
2.4. CONCLUSIONS……..…...…59
REFERENCES……..…..….59

3. EFFECT OF EDTA TREATMENT ON THE ACIDIC PROPERTIES OF USY ZEOLITE AND ITS PERFORMANCE IN VACUUM GAS OIL HYDROCRACKING…..……..……..……..……..……..……...……64
Summary…….……..…….....64
3.1. INTRODUCTION…….……...…..…65
3.2. EXPERIMENTAL……...…….……...…65
3.2.1. Preparation of zeolites and hydrocracking catalysts ……..…….…….....65
3.2.2. Characterization methods…….……..…66
3.2.2.1. Textural properties and crystal morphology…….…….....……66
3.2.2.2. Bulk, surface and framework composition…….……..…….…….66
3.2.2.3. Acid properties……..……..…….....67
3.2.2.4. Nuclear Magnetic Resonance…….…….……...68
3.2.3. Activity evaluation…….……..69
3.2.3.1. Zeolite acid activity tests…….……..…...…..69
3.2.3.2. Cracking activity of the extruded supports…….…….....69
3.2.3.3. Activity evaluation of hydrocracking catalysts.…….…….....…..…77
3.3. RESULTS AND DISCUSSION…….……..…..…70
3.3.1. XRD patterns ……..…….…….……..…70
3.3.2. Textural properties of the modified zeolites…….……..…...……71
3.3.3. Morphological characterization ……..……..……73
3.3.4. ^{29}Si MAS NMR characterization ……..……...…….74
3.3.5. Compilation of the main physicochemical properties of the modified zeolites…….……..….....76
3.3.6. Al speciation by ^{27}Al MQ MAS NMR ……..……...…78
3.3.7. Quantification of Al species with ^{27}Al MAS NMR…….……..…....80
3.3.8. Acidic properties of the modified zeolites…….……..…...83
3.3.8.1. Hydroxyl group speciation…….…….....83
3.3.8.2. Ammonia TPD…….……...85
3.3.8.3. Pyridine FTIR ……..…..86
3.3.9. Propane conversion and cracking of 1,3,5-tri-isopropylbenzene…….....…87
3.3.10. Properties of NiMoP supported catalysts……...……..….....89
3.3.11. Hydrocracking performance of NiMoP-supported catalysts……..…….....90
3.4. CONCLUSIONS……..……...…93
REFERENCES…….……..…94

4. EFFECT OF USY ZEOLITE CHEMICAL TREATMENT WITH AMMONIUM NITRATE ON ITS VGO HYDROCRACKING PERFORMANCE…….……..…..…..…

LIST OF TABLES

Pag.

LIST OF FIGURES

Pag.

LIST OF APPENDICES

Pag.

RESUMEN

TITULO: Efecto de los métodos de modificación en las propiedades de la zeolita USY y su desempeño en hidrocraqueo.*

AUTOR: José Luis Agudelo Valderrama**

PALABRAS CLAVES: Hidrocraqueo, Zeolita USY, Acidez, Aluminio extra-red, Desaluminización, Gasóleo de vacío, Tratamiento hidrotérmico, Lavado ácido, EDTA, Destilados medios.

DESCRIPCION:

Esta tesis doctoral contribuyó a mejorar el entendimiento de la relación entre las propiedades de la zeolita USY y su reactividad en hidrocraqueo. Estudios sobre el efecto del grado de desaluminización, el contenido de especies de aluminio no estructural, EFAl (Extraframework aluminum) y la mesoporosidad en el desempeño en hidrocraqueo de una carga real se llevaron a cabo con catalizadores a base de zeolitas USY modificadas. Se usó un conjunto amplio de técnicas para caracterizar las propiedades de las zeolitas y los catalizadores de hidrocraqueo, incluyendo XRD, análisis elemental, XPS, fisisorción de N_2, HRTEM, RMN de estado sólido de ^{29}Si y ^{27}Al, NH_3-TPD, FTIR de piridina adsorbida, UV-Vis DRS y Raman.

Los resultados indican que a menor contenido de aluminio en la estructura, menor actividad de hidrocraqueo. Tratamientos químicos moderados con ácido o con Na_2H_2-EDTA de la zeolita USY mostraron ser benéficos para incrementar la actividad de hidrocraqueo debido al mejoramiento del acceso a los sitios ácidos después de la remoción de especies EFAl aglomeradas. Sin embargo, la presencia de ciertas especies EFAl es necesaria para obtener alta actividad en hidrocraqueo de cargas reales. La remoción severa de especies EFAl es perjudicial para la producción de destilados medios dado que conduce a la exposición de sitos ácidos Brønsted fuertes, los cuales tienden a sobrecraquear la carga. La combinación de diferentes métodos de tratamiento resulta en catalizadores basados en zeolitas USY con actividad hacia destilados medios mejorada.

Esta tesis fue financiada por ECOPETROL S.A. y desarrollada en el Instituto Colombiano del Petróleo en colaboración con la Universidad Industrial de Santander dentro del convenio de cooperación tecnológica No. 03-2011. Parte de la experimentación fue realizada en la Universidad Tecnológica de Eindhoven (Holanda) durante la pasantía doctoral.

---

* Tesis para optar al título de Doctor en Ingeniería Química

** Facultad de Ingenieras Fisicoquímicas, Escuela de Ingeniería Química, Directora Prof. Sonia A. Giraldo, Codirector Dr. Luis Javier Hoyos.

ABSTRACT

TITLE: Effect of modification methods on USY zeolite properties and its hydrocracking performance.*

AUTHOR: José Luis Agudelo Valderrama**

KEYWORDS: Hydrocracking, USY zeolite, Acidity, Extraframework aluminum, dealumination, Vacuum gas oil, Hydrothermal treatment, Acid leaching, EDTA, middle distillates

DESCRIPTION:

This thesis attempted to contribute to the better understanding of the relationship between USY properties and hydrocracking reactivity. Systematic studies about the effect of the dealumination degree, the EFAl (Extraframework aluminum) content and the mesoporosity on the hydrocracking behavior of a real feedstock were performed with catalysts based on modified USY zeolites. A wide set of techniques including XRD, elemental analysis, XPS, N_2 physisorption, HRTEM, ^{29}Si and ^{27}Al solid-state NMR, ammonia TPD and FTIR spectroscopy of adsorbed pyridine, UV-Vis DRS and Raman were employed to characterize the physicochemical properties of the zeolites and hydrocracking catalysts.

Results indicate that a direct association exists between the degree of the framework dealumination and hydrocracking activity for the catalysts based on steam treated zeolites. The lower the framework aluminum content, the lower the hydrocracking catalytic activity. Mild chemical treatments with acid or Na_2H_2-EDTA to the USY zeolite showed to be beneficial to improve the hydrocracking activity because of the enhanced access to acid sites after the removal of agglomerated EFAl species. Nevertheless, the presence of certain EFAl species is necessary to achieve high hydrocracking activity of real feedstocks. The severe removal of EFAl is detrimental to middle distillates production as it results in the exposure of strong Brønsted acid sites, which tend to overcrack the feedstock. The combination of different treatment methods results in USY-based catalysts with enhanced activity and middle distillates selectivity in the hydrocracking of real feedstocks.

The financial support for the development of the present thesis was provided by ECOPETROL S.A. It was developed at the *Instituto Colombiano del Petróleo* in collaboration with the *Universidad Industrial de Santander* under the technological cooperation agreement 03-2011. Part of the experimentation was performed at the Eindhoven University of Technology (The Netherlands) during the doctoral stay.

---

* Thesis to obtain the degree of Doctor in Chemical Engineering.

** Faculty of Physicochemical Engineerings, School of Chemical Engineering. Director Prof. Sonia A. Giraldo, Codirector Dr. Luis Javier Hoyos.

1. GENERAL INTRODUCTION

1.1. OIL REFINING SCENARIO

At present, oil refiners are facing several important challenges to produce transportation fuels. They have to process high specific gravity/lower quality feeds because of the continuous depletion of conventional light/sweet crudes (especially in Latin American countries), they have to fulfill more stringent automotive fuels quality specifications (e.g. sulfur and aromatics content in diesel), and to satisfy the growing demand for middle distillates [1, 2]. Middle distillates refer to a range of refined products situated between lighter fractions, such as liquefied petroleum gas (LPG) or gasoline, and heavier products such as fuel oil. Typically they include jet fuel, heating kerosene, and diesel. Several processing options such as Fluid Catalytic Cracking (FCC), Coking and Hydrocracking (HCK) can be implemented to convert heavy feedstocks to middle distillates. The first two processes function basically by rejecting carbon from the feed molecules; in contrast, hydrocracking combines the molecular weight reduction with an increase of the hydrogen-to-carbon ratio. Due to this fact, hydrocracking technology stands out among all processes due to its superior versatility to produce high-quality finished products from even the most difficult-to-refine feeds. The wide variety of feedstocks that can be processed in hydrocrackers includes atmospheric gas oils, catalytically cracked light and heavy cycle oils, vacuum gas oils, coker or thermally cracked gas oils and deasphalted oil. In modern refineries FCC and hydrocracking units work as a team. The catalytic cracker takes the more easily cracked paraffinic atmospheric and vacuum gas oils (VGO) as feedstocks, while the hydrocracker uses more aromatic cycle oils and coker distillates as feedstocks. Accordingly, the world hydrocracking capacity is steadily growing. In Colombia, for instance, two new hydrocracking projects are in development to cope with the above mentioned market requirements. Consequently, gaining deeper knowledge about the hydrocracking process is of significant importance for local refiners and researchers.

1.2. HYDROCRACKING PROCESS

The hydrocracking process takes place in a hydrogen-rich atmosphere at elevated temperatures (260 – 425 °C) and pressures (35 – 200 bar) in the presence of catalysts specially tailored for the purpose [3, 4]. In hydrocracking, the high partial pressure of hydrogen also prevents condensation of alkenes, reducing coke formation. As a result, the catalyst functions virtually at its activity for long-stream times without the need for regeneration. There are two levels of hydrocracking severity: mild and conventional. In mild hydrocracking the process is run at less severe operating conditions and is attempted to operate existing VGO hydrodesulfurization (HDS) units. Hydrocracking, as the name implies, is a catalytic process combining hydrogenation and cracking reactions occurring either simultaneously or sequentially. Basically, the process cracks the high-boiling, high molecular weight hydrocarbons into lower-boiling, lower molecular weight olefinic and aromatic hydrocarbons and then hydrogenates them. The mechanism is basically that of catalytic cracking with the addition of hydrogenation and isomerization. For the hydrocracking of a paraffin, for instance, the initial step is its dehydrogenation to an olefin followed by adsorption on an acid site and conversion to a carbonium ion. The ion rearranges to a more stable form which can either rehydrogenate to give back an isomerized paraffin or it can crack into lighter fragments of an olefin and an ion (cation) which are hydrogenated up to the paraffins. Any sulfur and nitrogen compound present in the hydrocracking feedstock are, to a large extent, also hydrogenated and form gaseous hydrogen sulfide (H_2S) and ammonia (NH_3), which are subsequently removed [5]. The result is that the hydrocracking products are essentially free of sulfur and nitrogen impurities and consist mostly of paraffinic hydrocarbons. Hydrocracking can be suited to produce jet and diesel fractions with sulphur contents below 20 ppm and very good combustion properties (diesel cetane numbers above 55). Hydrocracking is also used to isomerize paraffins, to diminish the jet freeze point and to increase the kerosene smoke point. The product yields and product properties are determined by the feedstock, the cracking catalyst selectivity and the process conditions [1, 4, 6, 7].

1.3. HYDROCRACKING PROCESS CONFIGURATIONS

Different process and reactor configurations have been developed to carry out the hydrocracking process [8]. Typical hydrocracking configurations are presented in **Figure 1.1.**

Figure 1.1. Hydrocracking configurations [9]

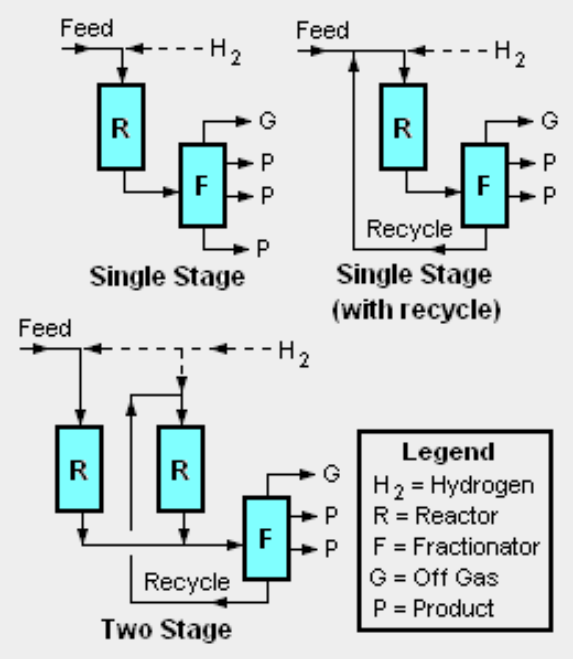

In general, the type of feedstock and desired range of products determine to a large extent the type of processing used. The most common hydrocracking configurations are single stage and two-stage. In single-stage hydrocrackers, the catalysts are contained in a single reactor (once through) or series reactors (series-flow) [5]. This configuration finds application in cases where only moderate degree of conversion (say 60% or less) is required. A single catalyst type might be employed or a stacked-bed arrangement of two different catalysts might be used. In single stage or series-flow hydrocracking all catalysts are exposed to high levels of H_2S and NH_3 that are generated during removal of organic sulfur and nitrogen from the feed. This ammonia interferes with the acidic activity of the catalyst. The single stage configuration can be implemented in recycle mode (single stage with recycle). The uncracked residual hydrocarbon oil from the bottom of the fractionation tower can be recycled back into the single reactor for further cracking. This kind of configuration is the most commonly used. The two stage

hydrocracking configuration, in turn, is implemented when high/full conversion is required. This configuration uses two reactors with inter-stage product separation. The residual hydrocarbon oil from the bottom of the fractionation tower is recycled back to either the pretreat (first stage) or the cracking reactors (second stage). Since the first stage reactor accomplishes both hydrotreating and hydrocracking, the second stage reactor feed is virtually free of ammonia and hydrogen sulfide. This permits the use of high performance noble metal (palladium, platinum) catalysts, which are susceptible to poisoning by sulfur or nitrogen compounds [10].

1.4. HYDROCRACKING CATALYST

Hydrocracking catalysts are bifunctional systems, having a cracking function and a hydrogenation-dehydrogenation function [11, 12]. The cracking function is provided by an acidic support, while the hydrogenation-dehydrogenation function is provided by metals or metal sulfides. There should be a rapid molecular transfer between the metallic site and acidic sites in order to avoid undesirable secondary reactions and coke formation. Therefore, the balance between the (de)hydrogenation and cracking functions is very important to get suitable performance. The composition of a hydrocracking catalyst depends on the mode of the operation (one or two-stage), the characteristics of the feedstock and on the final product requirements.

1.4.1. Dehydrogenation-hydrogenation function

The metals providing the hydrogenation–dehydrogenation function can be noble metals (Pd, Pt) or non-noble metal sulfides from Group VI.A (Mo, W) and group VIII.A (Co, Ni). These metals catalyze the hydrogenation of the feedstock, making it more reactive for cracking, heteroatom removal and reducing the coking rate. They also initiate the cracking by forming a reactive olefin intermediate via dehydrogenation. **Table 1.1** presents a guideline of hydrocracking catalysts composition depending on the application type. The metal sulfide catalysts are most common and noble metal based catalysts are used in sulfur-free systems only in cases where a very hydrogenated product is desired. Since in hydrocracking organo-nitrogen compounds are the most deleterious, NiMo-based catalysts are the usual catalysts of choice because of their

superior HDN activity. NiW sulfides are applied where hydrogenation performance is of top importance [5].

1.4.2. Cracking function

Besides cracking, ring opening and isomerization reactions also take place on the acidic support. Early generation catalysts for hydrocracking were generally based on amorphous silica aluminas (ASA). Later, zeolitic hydrocracking catalysts were developed. Catalysts with amorphous supports are still in commercial use, primarily where maximizing the production of middle distillates is the objective (**Table 1.1**).

Several zeolite types such as Beta [13-15], ITQ-2 [16], and other materials such as MCM-41 [17], or MCM-48 [18] and zeolite composites [19-21] have been proposed to be good hydrocracking carriers. However, mostly Y zeolite (FAU-type structure) in its ultra-stable form (USY) has found application in hydrocracking [22-27].

Table 1.1. Types of catalysts used in different hydrocracking processes [9].

Application type	Process type (# stages)	Hydrogenerating function			Acid function	
		Pd	Ni–Mo	Ni–W	Y-type zeolite	SiO_2/Al_2O_3 amorphous
Max. Naphtha	One	xxx	x	x	xxx	
Max. Naphtha	Two	xxx			xxx	
Max. Kerosene	One		xxx	x	xxx	
Max. Kerosene	Two	x	x	x	x	x
Max. Diesel oil	One		x	x	x	x
Max. Diesel oil	Two		x	x		x
Max. Lube oils	One		x	x	x	x

x represents frequency of use

1.4.3 The Zeolite Y

The faujasite framework consists of sodalite cages which are connected through hexagonal prisms (doble 6-rings). The pores are arranged perpendicular to each other. The pore, which is formed by a 12-membered ring, has a relatively large diameter of 7.4 Å. The inner cavity has a diameter of 12 Å and is surrounded by 10 sodalite cages. The unit cell is cubic; Pearson symbol cF576, symmetry Fd3m, No.227 [28], lattice constant

24.7 Å. Zeolite Y has a void fraction of 48% and a Si/Al ratio of 2.43. **Figure 1.2** presents a representation of the Y zeolite structure EFAl species are represented as clusters.

Figure 1.2. Representation of the Y zeolite structure.

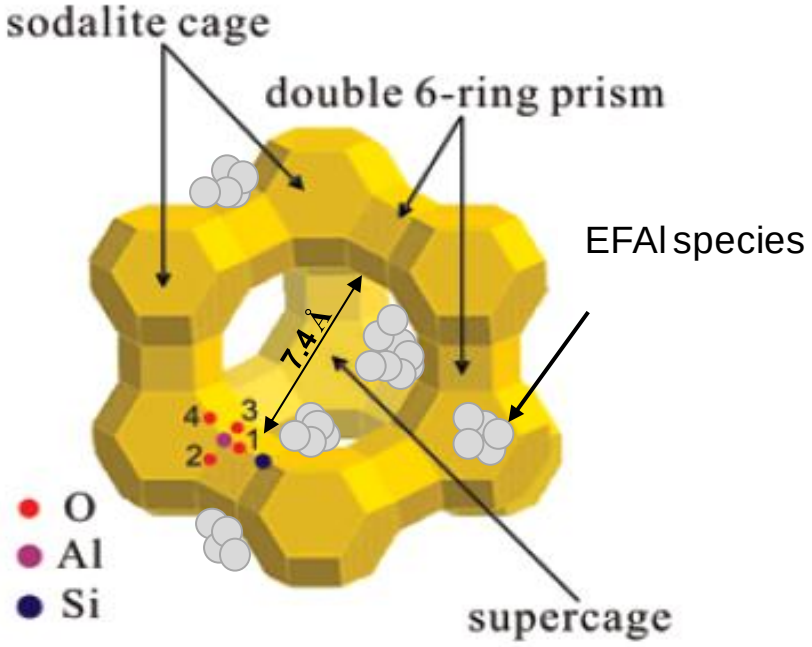

1.4.4. Use of USY zeolite in hydrocracking

USY zeolites provide by far the highest cracking activity and organic nitrogen tolerance. Compared to ASAs they also show a more stable performance. On the other hand, they may suffer from mass transport limitations, leading to lower selectivities to desired products and/or increased gas make. High molecular weight molecules with over 25 carbon atoms per molecule, such polycyclic aromatics and polycyclic naphthenes, do not enter the USY pores due to steric hindrance, while paraffinic compounds can more easily reach them. The selectivity of Y-type zeolite toward middle distillates is lower than that of amorphous material at the same conversion level because of the overcracking of middle distillates to naphtha and gases.

USY zeolites can be modified and tailored to particular hydrocracking applications. Modification techniques usually involve some combination of hydrothermal treatment (steaming), ion-exchange and leaching processes with mineral or organic acids, bases, salts and chelating agents [11]. Hydrothermal treatment results in dislodgement of Al

atoms from the framework into extraframework positions and these dislodged Al atoms (EFAl species) are usually concentrated near the surface of the crystal. Framework dealumination by steaming is also accompanied by loss of crystallinity and the creation of a secondary pore system (mesoporosity). Combined modification techniques provide a means of controlling the amount of aluminum located in the tetrahedral framework sites (the primary Brønsted acid sites), but also the amount of extra-framework aluminum and the mesopores that are created during the dealumination process.

USY zeolites are also used in the Fluid Catalytic Cracking process (FCC). Therefore, a plethora of studies have been carried out during the last decades with the objective to better understand aspects related to the performance of USY zeolite in FCC [29]. Comparatively, there has been less attention to the role and optimization of USY zeolite in hydrocracking. Although hydrocracking is a mature process, still new developments are coming out, stimulated by a steady growth of the market and environmental pressures on product qualities. Nowadays, efforts are directed towards the development of new generation types of zeolite Y-based hydrocracking catalysts with optimum number and strength of acid sites and suitable pore structure with high activity tailored to desired selectivity [30]. A general aim is to maximize the production of middle distillates. In recent works, activity of zeolite-containing catalyst and their selectivity to middle distillates have been enhanced by decreasing the USY zeolite crystal size [25], increasing the proximity between the hydrogenation/dehydrogenation function and the acid sites of the zeolite [24], and by combining several modification methods [26, 27, 30].

1.5. MOTIVATION OF THE THESIS

From the scientific point of view, despite several hydrocracking studies often using model feedstocks such as short alkanes or aromatics, there is still a lack of systematical studies using real feedstocks [31]. The role of extraframework Al species, the relationship between Brønsted and Lewis acid sites and the effect of the method employed to create mesoporosity and/or to dealuminate the USY zeolite have been scarcely investigated for hydrocracking applications in a systematical way, in particular when maximum middle distillates yield is required. The present thesis is a contribution in that direction.

1.6. SCOPE OF THE THESIS

The main goal of the present thesis was to determine how systematic changes in the properties of USY zeolite would affect the vacuum gasoil (VGO) hydrocracking performance. Hydrothermal treatment was coupled to three different chemical modification methods to obtain USY zeolites with diverse properties. Hydrocracking catalysts were prepared from alumina and the modified USY zeolites and then loaded with a P-promoted NiMo-sulfide phase. Their performance was evaluated in the hydrocracking of a heavy VGO under conditions close to the industrial practice. A wide set of techniques including XRD, elemental analysis, XPS, N_2 physisorption, HRTEM, ^{29}Si and ^{27}Al solid-state NMR, ammonia TPD, FTIR spectroscopy of adsorbed pyridine, UV-Vis DRS, Laser Raman Spectroscopy, were employed to characterize the physicochemical properties of the zeolites and hydrocracking catalysts.

1.7. ORGANIZATION OF THE THESIS

In chapter 2 hydrothermal treatment coupled to mild acid leaching with HCl were selected as modification methods to obtain USY zeolites with diverse properties. The influence of the dealumination degree of USY zeolite by changing the steaming temperature and the removal of EFAl species by acid treatment with HCl on the zeolites properties and their hydrocracking performance was studied. In chapter 3 hydrothermal treatment was coupled to Na_2H_2-EDTA leaching. The focus of chapter 3 was on the role of the EFAl species. EDTA-modified zeolites were obtained with different severity of treatment by varying the concentration of the leaching agent. In that way, three zeolites with decreasing content of EFAl species were obtained. Chapter 4 deals with hydrothermal treatment coupled to ammonium nitrate (AN) treatment. This treatment was selected with the aim of studying the effect of the enhancement in the mesoporosity of a steam-treated USY zeolite in the VGO hydrocracking performance. Ammonium nitrate treated zeolites were obtained by varying the temperature of treatment. Finally, in chapter 5 the main effects of each method on the properties of the USY zeolites are summarized and the impacts of the treatments on VGO hydrocracking activity and middle distillates yield are compared. General conclusions are presented in chapter 6. With the aim of providing a coherent understanding of the characterization results presented in chapters 2, 3 and 4, **Appendix A** contains a full description of the

characterization techniques that were used to assess the properties of the modified zeolite and the hydrocracking catalysts.

REFERENCES

[1] J.A.R. van Veen, J.K. Minderhoud, L.G. Huve, W.H.J. Stork, Handbook of Heterogeneous Catalysis, Wiley-VCH Verlag GmbH & Co. KGaA, 2008.

[2] A. Stanislaus, A. Marafi, M.S. Rana, Catalysis Today 153 (2010) 1–68.

[3] L. Lloyd, Handbook of industrial catalysts, Springer, 2011.

[4] A. Gruia, Practical Advances in Petroleum Processing, Springer, 2006, pp. 219-255.

[5] A. Gruia, Handbook of Petroleum Processing, Springer, 2006, pp. 287-320.

[6] P.R. Robinson, G.E. Dolbear, Hydroprocessing of Heavy Oils and Residua (2007) 281.

[7] J.G. Speight, The chemistry and technology of petroleum, CRC press, 2014.

[8] J.G. Speight, The refinery of the future, William Andrew, 2010.

[9] M.A. Fahim, T.A. Al-Sahhaf, A. Elkilani, Fundamentals of petroleum refining, Elsevier, 2009.

[10] J.G. Speight, The chemistry and technology of petroleum, CRC Press/Taylor and Francis, 2007.

[11] J. Scherzer, Hydrocracking Science and Technology, Marcel Dekker, New York, 1995.

[12] S. Mohanty, D. Kunzru, D. Saraf, Fuel 69 (1990) 1467-1473.

[13] S. Chen, Y. Yang, K. Zhang, J. Wang, Catalysis Today 116 (2006) 2-5.

[14] M. Camblor, A. Corma, A. Martınez, V. Martınez-Soria, S. Valencia, Journal of Catalysis 179 (1998) 537-547.

[15] A. Hassan, S. Ahmeda, M.A. Ali, H. Hamida, T. Inui, Applied Catalysis A: General 220 (2001) 59–68.

[16] A. Corma, A. Martınez, V. Martınez-Soria, Journal of Catalysis 200 (2001) 259-269.

[17] A. Corma, A. Martinez, V. Martinezsoria, J.B. Monton, Journal of Catalysis 153 (1995) 25-31.

[18] A.M. Alsobaai, R. Zakaria, B.H. Hameed, Chemical Engineering Journal 132 (2007) 173–181.

[19] X. Zhang, Q. Guo, B. Qin, Z. Zhang, F. Ling, W. Sun, R. Li, Catalysis Today 149 (2010) 212–217.

[20] Q. Zhao, B. Qin, J. Zheng, Y. Du, W. Sun, F. Ling, X. Zhang, R. Li, Chemical Engineering Journal 257 (2014) 262-272.

[21] X. Zhang, F. Zhang, X.Y.Z. Zhang, F. Sun, Z.W.D. Zhao, J Porous Mater 15 (2008) 145–150.

[22] Q. Cui, Y. Zhou, Q. Wei, G. Yu, L. Zhu, Fuel Processing Technology 106 (2013) 439-446.

[23] J.W. Ward, Fuel Processing Technology 35 (1993) 55-85.

[24] J. Francis, E. Guillon, N. Bats, C. Pichon, A. Corma, L. Simon, Applied Catalysis A: General 409 (2011) 140-147.

[25] Q. Cui, Y. Zhou, Q. Wei, X. Tao, G. Yu, Y. Wang, J. Yang, Energy & Fuels 26 (2012) 4664-4670.

[26] H. Shimada, K. Sato, K. Honna, T. Enomoto, N. Ohshio, Catalysis Today 141 (2009) 43–51.

[27] X.-w. Chang, L.-f. He, H.-n. Liang, X.-m. Liu, Z.-f. Yan, Catalysis Today 158 (2010) 198-204.

[28] J. Hriljac, M. Eddy, A. Cheetham, J. Donohue, G. Ray, Journal of Solid State Chemistry 106 (1993) 66-72.

[29] M.S. Rigutto, R. van Veen, L. Huve, Studies in surface science and catalysis 168 (2007) 855-XXVI.

[30] K.P. de Jong, J. Zečević, H. Friedrich, P.E. De Jongh, M. Bulut, S. Van Donk, R. Kenmogne, A. Finiels, V. Hulea, F. Fajula, Angewandte Chemie 122 (2010) 10272-10276.

[31] E. Benazzi, L. Leite, N. Marchal-George, H. Toulhoat, P. Raybaud, Journal of Catalysis 217 (2003) 376–387.

2. INFLUENCE OF HYDROTHERMAL TREATMENT AND ACID LEACHING ON THE VGO HYDROCRACKING PERFORMANCE OF USY ZEOLITE*

SUMMARY

The effect of hydrothermal treatment and acid leaching with HCl on the physico-chemical properties of zeolite Y and its vacuum gas oil hydrocracking performance were investigated. Ultra-stabilized Y (USY) zeolites were obtained by steam-calcination at 500, 600 and 700 °C. Steam-treated zeolites were further subjected to a mild acid leaching treatment. Steam-calcination at increasing severity resulted in progressive framework dealumination and decreasing micropore surface area. At the same time, the Al content at the zeolite crystal surface increased. Acid leaching with HCl improved the pore accessibility and acid properties of the USY zeolites due to the extraction of extraframework Al species (EFAl). NiMoP-based hydrocracking catalysts were prepared from the modified USY zeolites with alumina as binder. Hydrocracking activities correlated with the acidity of the zeolites. Too severe steam treatment led to depopulation of acid sites and lowered the hydrocracking performance. Hydrocracking catalysts based on the acid leached zeolites were more active than those based on the corresponding steam-treated zeolites. It is based on the removal of agglomerated extraframework Al species that block the access to some of the micro- and mesopores. This study points out that, aside from the acidity, also other parameters such as pore accessibility and the presence of EFAl have considerable influence on the hydrocracking of the heavy molecules in a gas oil feed.

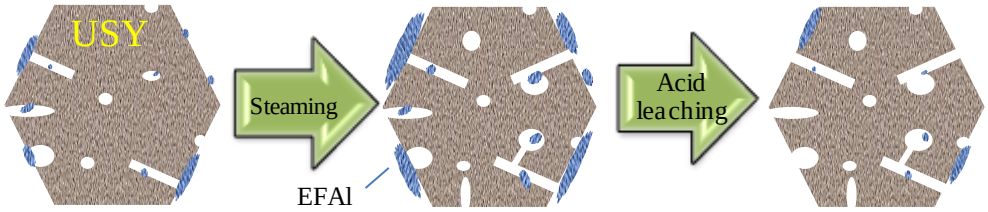

* The content of this chapter was published as*: Influence of steam-calcination and acid leaching treatment on the VGO hydrocracking performance of faujasite zeolite.* J.L. Agudelo, E.J.M. Hensen, S.A. Giraldo, L.J. Hoyos. *Fuel Processing Technology* 133 (2015) 89–96.

2.1. INTRODUCTION

In hydrocracking technology the catalyst plays a key role in determining the product distribution [1]. Amorphous silica-alumina (ASA) and ultra-stabilized Y (USY) zeolite are commonly used as acidic supports in hydrocracking catalysts. Hydrocracking uses framework-dealuminated USY zeolites. Zeolite Y is dealuminated to limit its hydrogen transfer activity. In this way, its propensity to coke deactivation is diminished. In addition, dealumination is needed to convert the initially weakly acidic Y zeolite with low framework Si/Al ratio into the highly acidic ultra-stabilized Y zeolite. The activity and selectivity in hydrocracking is mainly determined by the Brønsted acidity of the support, which closely correlates to the framework Si to Al ratio. For zeolite Y, the higher the degree of framework dealumination, the higher the middle distillates selectivity [2]. Highly dealuminated Y zeolites have comparable acidity to amorphous silica-alumina supports and, accordingly, offer similar high middle distillates selectivity. The low acidity of such materials results in low reaction rates, which needs to be compensated by higher reaction temperature. Tuning the acidity of Y zeolite, therefore, remains a major topic in the design of active hydrocracking catalysts for middle distillates production. The approach is to use moderately dealuminated zeolites and optimize their acid and textural properties to obtain satisfactory conversion levels and middle distillates yield [3].

Typically, USY zeolites are dealuminated by hydrothermal treatment (steam calcination). The removal of framework Al atoms by hydrothermal treatment generates extraframework aluminum species (EFAl). The amount and nature of the EFAl species formed depend on the severity of the hydrothermal treatment [4]. The presence of large amounts of EFAl formed during hydrothermal treatment has a detrimental effect on catalytic and transport properties so that it is common to extract the EFAl by subsequent chemical attack procedures. On the other hand, it is known that some EFAl species are important to enhance the intrinsic acidity in USY zeolites [5]. The improved cracking activity of USY zeolites is believed to be influenced by synergistic interactions between framework acid sites and cationic EFAl species [6]. This topic has been subject of active debate in literature [7-10]. Hydrothermal treatment also results in loss of crystallinity and the development of a secondary pore system, partially reducing mass transport limitations and offering the possibility to convert a higher fraction of the feedstock.

Hydrothermal treatment is commonly combined with chemical modification methods. These methods are designed to improve the zeolite properties such as mesoporosity and acid strength and density. Many modifying agents have been employed for this purpose including mineral and organic acids, $(NH_4)_2SiF_6$, bases such as NaOH (desilication), gaseous reactants such as $SiCl_4$ and chelating agents such as EDTA [4, 11-15]. Some of these agents have been employed with success to obtain zeolites with suitable properties to be the acidic component in hydrocracking catalysts [14, 16-19].

Although a significant body of knowledge exists in the field of modifying Y zeolite, there are relatively few studies that determine the influence of changes in the Y zeolite structure and acidity on the hydrocracking performance. Additionally, despite several hydrocracking studies often using model feedstocks such as short alkanes or aromatics [20-22], there is still a lack of studies using real/heavy feedstocks [23, 24]. The role of extraframework Al species, the relationship between Brønsted and Lewis acid sites and the effect of the method employed to dealuminate the USY zeolite have not been systematically investigated in hydrocracking, in particular when maximum middle distillates yield is required.

The main goal of the present chapter was to determine how systematic changes in the properties of the acid function of the hydrocracking catalyst would affect catalytic behavior under conditions close to industrial practice. The influence of the dealumination degree of USY zeolite on its hydrocracking performance was studied. A subsequent mild acid leaching treatment was used to remove some of the deleterious EFAl species. Hydrocracking catalysts were prepared from the steam-treated and acid-leached USY zeolites by loading a P-promoted NiMo-sulfide phase. Their performance was evaluated in the hydrocracking of a heavy vacuum gas oil. Although acidity is one of the main catalyst parameters, the results show that small variations in other properties will strongly affect the performance in the conversion of heavy feedstock molecules present in a VGO feed.

2.2. EXPERIMENTAL

2.2.1. Zeolites modification

A NH_4-Y zeolite with low sodium content (less than 0.15 wt.%) was obtained by threefold ion exchange of a commercial faujasite zeolite (CBV400, *Zeolyst*

International) at 85 °C for 1 h in suspensions of 15 wt.% aqueous solution of NH_4NO_3 (6.7 mL/g of zeolite). The resulting solid was filtered, washed with distilled water and dried at 105 °C for 14-16 h. HT500, HT600 and HT700 samples were then obtained by hydrothermal treatment of portions of the NH_4-Y zeolite under 100% steam flow for 5 h at 500, 600 or 700 °C, respectively. Typically, portions of 40 g of the NH_4-Y zeolite were placed in a 6 cm internal diameter quartz reactor and heated to the target temperature under dry air flow (100 sccm), followed by an isothermal step of 2 h. After that, water vapor was introduced (3 g water/min) and the air flow was stopped. The target temperature was kept for 5 h. Then, the zeolite was allowed to dry and cool to room temperature under dry air flow (100 sccm).

Acid leaching treatment was done by stirring the suspended HT zeolite in a 0.25 N HCl solution at 60 °C for 2 h, followed by filtration, washing, drying at 105 °C for 14-16 h and calcination at 550 °C for 4 h. The resulting samples are denoted by adding the suffix AL (acid leaching) to the corresponding HT zeolite.

2.2.2. Preparation of hydrocracking catalysts

Composite hydrocracking catalysts were prepared from the hydrothermally-treated and acid-leached zeolites. Each modified zeolite (40 wt.%) was kneaded with alumina binder (Catapal B, kindly supplied by *Sasol North America Inc.*) using a 1 wt.% HNO_3 solution as peptizing agent. The zeolite content was established aiming to obtain highly active catalysts. The resulting doughs were extruded into cylindrical shapes with a diameter of 1 mm. These catalyst bodies were dried, crushed and calcined at 550 °C for 6 h under static conditions. Subsequently, NiMoP-containing catalysts were prepared by sequential introduction via incipient wetness impregnation of P, Mo and Ni in the form of phosphoric acid (85 wt.%, Merck), ammonium heptamolybdate tetrahydrate (99 wt.%, Merck) and nickel nitrate hexahydrate (99 wt.%, Merck). Intermediate drying at 105 °C for 15 h and calcination under static air in an oven at 500 °C for 2 h were performed after each impregnation step. The intended (nominal) loadings were 1 wt.% of P, 15 wt.% of MoO_3 and 3 wt.% of NiO. The final hydrocracking catalysts based on the steam treated zeolites were denoted as NiMoP/(HT### + Alumina). The catalysts based on the acid leached zeolites were denoted as NiMoP/(HT###AL + Alumina). "###" denotes the treatment temperature applied during the hydrothermal treatment.

2.2.3. Characterization methods

2.2.3.1. Textural properties and morphology

Nitrogen adsorption measurements for all samples were carried out at 77 K on a Micromeritics ASAP 2020 instrument. The samples were outgassed at 400 °C for 8 h prior to the sorption measurements. The Brunauer-Emmett-Teller (BET) adsorption isotherm model was used to determine the total surface area. The mesopore volume and mesopore size distribution was calculated from the adsorption branch of the isotherm by the Barrett-Joyner-Halenda (BJH) method.

High resolution transmission electron microscopy (HRTEM) images of the zeolite particles were taken on a FEI Tecnai 20 microscope at an electron acceleration voltage of 200 kV. Prior to measurements, the zeolite samples were suspended in ethanol, sonicated for 1 min, and dispersed over a carbon coated holey Cu grid.

2.2.3.2. Bulk, surface and framework composition

The bulk chemical composition was determined by ICP-OES after proper digestion of the complete sample in a mixture of HF/HNO_3 acids.

The surface composition of the zeolites was measured by a Thermo Scientific K-Alpha X-ray Photoelectron Spectrometer (XPS) system. The conditions used for all of the survey scans were as follows: energy range 1350-0 eV, step size 1 eV. For the high-resolution spectra an energy range of 40 eV was used at a step size of 0.1 eV. All spectra were analyzed using the CasaXPS software. Peak shifts were normalized with the C 1s peak set to 284.5 eV. The surface Si/Al ratio was calculated by dividing the intensity (peak area) for Si and Al by the appropriate sensitivity factors (0.234 and 0.339 for Al and Si, respectively).

XRD patterns were recorded on a Bruker D4 Endeavor diffractometer using CuKα radiation in the range of $5° \leq 2\theta \leq 60°$ with a step size of 0.0028 2θ and a time per step of 1s. The unit cell size (UCS, a_0) of the zeolites was determined using a full pattern matching procedure with the TOPAS software. Profile fitting was performed using the TCHZ pseudo-Voigt function. Background was simulated with a Chebychev Polynomial of 5th order. The (111) reflection at around 6.34 2θ was excluded in the calculation of UCS values due to its high asymmetry.

2.2.3.3. Acid properties

FTIR spectroscopy of adsorbed pyridine was used to probe Brønsted and Lewis acidity. Spectra were recorded with a Bruker Vertex V70v instrument equipped with a home-made controlled-environment transmission cell and CaF_2 windows. Typically, a small amount of zeolite powder was pressed into a self-supporting wafer. The wafer was heated for 1 h under vacuum to 550 °C at a rate of 10 °C/min. After cooling to 150 °C, a reference spectrum was taken. The sample was then exposed to pyridine until it was saturated. Physisorbed pyridine was removed by evacuation for 1 h at 150 °C. The resulting FTIR spectrum was used to determine the total acidity. Then, the sample was evacuated at 300 °C and 500 °C for 1 h and spectra were recorded at 150 °C after each desorption step. These spectra were used to quantify the acid sites of medium and strong strength. The concentration of Brønsted (peak at 1550 cm^{-1}) and Lewis (peak at 1450 cm^{-1}) acid sites were determined using the following equation [25].

$$Concentration\,(mol/g\ of\ zeolite) = \left(\frac{peak\ area\ of\ acid\ site\ band \times wafer\ area}{wafer\ dried\ weight \times molar\ ext.coefic\ ient} \right)$$

Values for the molar extinction coefficients were 0.73 cm/mol and 1.11 cm/mol for Brønsted and Lewis acid sites, respectively [26].

2.2.3.4. Nuclear Magnetic Resonance

The ^{27}Al Magic Angle Spinning (MAS) Nuclear Magnetic Resonance (NMR) spectra of the zeolite samples were recorded on a Bruker DMX500 NMR spectrometer operating at a magnetic field of 11.7 T. For the ^{27}Al MAS NMR a standard Bruker MAS probe head was used with 2.5 mm rotors spinning at a rate of 20 kHz. In a typical experiment, about 10 mg of hydrated sample was packed in the zirconia rotor. The ^{27}Al chemical shift was referred to a saturated $Al(NO_3)_3$ solution.

The ^{29}Si MAS NMR spectra were recorded on a Bruker AVANCE III D400 spectrometer operating at a magnetic field of 9.4 T at a spinning rate of 14 kHz. Spectra were obtained using single pulse excitation ($\pi/2$ pulses). The ^{29}Si spectra were externally referenced to Q_8M_8 (cubic octameric silicate) at 0 ppm. ^{29}Si MAS NMR experiments offer definite benefits of observing spin 1/2 nuclei, for which line

broadening is effectively removed by sample rotation at the magic angle ($\theta = 54.74°$). Resonances corresponding to different framework silicon environments occur in characteristic chemical-shift ranges with increasing shifts of ca. 5 - 6 ppm. Individual signals are represented as $Q^4(nAl) = Si(nAl) = Si(0Si)_{4-n}(0Al)_n$, where Q^4 represents a Si atom connected to four T atoms by a bridging oxygen and nAl indicates the number of aluminum atoms in the second coordination shell. Peaks at chemical shifts around -107, -101, -95 and -89 ppm are assigned to $Q^4(0Al)$, $Q^4(lAl)$, $Q^4(2Al)$ and $Q^4(3Al)$, respectively. According to Lowenstein's rule aluminum tetrahedral does not link together in zeolites because of the repulsion of two adjacent negative charges. The quantitative line shape analysis of the ^{29}Si MAS NMR spectra was performed by using the Dmfit2011 software [27]. Every resolved component of the experimental NMR spectra was described by pure Gaussian lineshapes. The position (chemical shift) and the height of the corresponding lines were optimized by a least square fit. Besides the $Q^4(nSi)$ signals, an additional peak fixed at -110 ppm assigned to an extraframework amorphous silica phase (Si_{EF}) was added while fitting in order to reach a decomposition within the noise level. Due to its asymmetry, the $Q^4(0A1)$ framework site was fitted with a double line structure [28, 29]. The existence of two different $Q^4(0A1)$ atoms at distinct crystallographic positions has been reported before [30]. Species $Q^3 = Si(0Si)_2(0Al)_1(OH)_1$ and $Q^2 = Si(0Si)_2(OH)_2$ (typically at -92 ppm), and $Q^3 = Si(0Si)_3(OH)$ (typically at -101ppm) were not taken into account for the fit. The relative intensities of the components of every simulated spectrum ($I_{Si(nAl)}$) were obtained by integrating over the component line compared to the total integral over all component lines of the simulated spectrum. The framework Si/Al was calculated from ^{29}Si MAS NMR spectra using the relative intensities of Si(nAl) peaks according to the following equation [31].

$$Si/Al = \frac{\sum_{n=0}^{4} I_{Si(nAl)}}{\sum_{n=0}^{4} 0.25\, n \cdot I_{Si(nAl)}}$$

Further information about the fundaments of the zeolite characterization techniques used in this thesis can be found in [31-36].

2.2.3.5. Characterization of NiMoP-supported catalysts

UV–Vis Diffuse Reflectance Spectroscopy (DRS) and Laser Raman spectroscopy (LRS) measurements were performed to the composite NiMoP hydrocracking catalysts in their oxide state. UV–Vis DRS spectra were recorded on a Shimadzu UV-2401 PC spectrometer in diffuse-reflectance mode with a 60 mm integrating sphere in the 200–800 nm range. $BaSO_4$ was used as the reference material. The spectra were transformed using the Kubelka–Munk function. Laser Raman spectra were recorded with a Jobin–Yvon T64000 triple stage spectrograph with spectral resolution of 2 cm^{-1} operating in double subtractive mode. The laser line at 325 nm of a Kimmon He–Cd laser was used as exciting source. The power of the laser on the sample was 4 mW.

Surface analysis by XPS spectroscopy was applied to characterize the sulfidability of the hydrocracking catalysts. Sulfidation of the samples was done by heating typically 0.25 g of 50/80 mesh of the calcined NiMoP catalyst pellets in a stainless steel micro reactor in a mixed H_2S/H_2 flow (15 mol% H_2S) at a rate of 6 °C/min up to 400 °C; the final temperature was maintained for 2 h. The sample was then cooled to room temperature and the gas was switched to He. By closing valves before and after the reactor, the sample was transferred to a glove box under nitrogen atmosphere with controlled oxygen and water levels (both < 1 ppm) in order to avoid re-oxidation of the catalyst. The samples were crushed in a mortar and pressed onto a double-sided carbon tape attached to a sample holder. The sample holder was then transferred from the globe box to the introduction chamber of the XPS spectrometer under exclusion of air. XPS spectra were recorded on a KRATOS AXIS ULTRA instrument with an Al monochromator source (1486.6 eV) and a hemi-spherical analyzer operating at fixed pass energy of 40 eV and working under high vacuum ($<10^{-9}$ Pa). The Al 2p peak from the support at 74.5 eV was used as internal standard for binding energy calibration.

The Mo 3d, Ni 2p, S 2p, Al 2p, O 1s, and Si 2p spectra were analyzed using the software CasaXPS. A Shirley background subtraction was applied and a 30/70 Gaussian/Lorentzian ratio for peak decomposition was used. The Mo 3d spectra were decomposed into a main peak ($3d_{5/2}$) and the associated peak ($3d_{3/2}$). These two peaks are bound to each other by binding energy, width at half height and relative areas. For the kind of samples of the present study, molybdenum can exist as disulfide (MoS_2, Mo^{IV}), oxide (MoO_x, Mo^{VI}) and oxysulfide (MoO_xS_y, Mo^{V}) compounds. In the disulfide form, the doublet is located at 229.0 eV (Mo^{IV} $3d_{5/2}$) and 232.1 eV (Mo^{IV} $3d_{3/2}$). For the

Mo oxide phase, contributions are located at 232.2 eV (Mo^{VI} $3d_{5/2}$) and 235.3 eV (Mo^{VI} $3d_{3/2}$). For the oxysulfide phase the doublet appears at 230.2 eV (Mo^{V} $3d_{5/2}$) and 233.4 eV (Mo^{V} $3d_{3/2}$). The Mo region of the spectrum contains two additional bands located at 226.0 eV and 227.6 eV corresponding to S^{2-} in MoS_2 and S_2^{2-} in MoO_xS_y species, respectively. These sulfur species must be subtracted from the total spectrum of Mo 3d. The constrain values applied during the decomposition for the Mo 3d spectra were taken from the work of Gandubert et al [37]. Ni may exist on the surface of the sulfide catalysts as NiO_x, NiS_x (Ni_2S_3, Ni_9S_8, NiS) and NiMoS phase. The main binding energy position (Ni $2p_{3/2}$) for the oxide form appears at 856.0 eV, for the sulfide is at 856.0 eV and for the NiMoS phase the contribution is located at 854.0 eV. The constrain values for binding energy, area, width at half height and the number of satellite peaks used for the decomposition of the Ni $2p_{3/2}$ spectra were taken from reference [38]. The sulfidation degree is derived from the Mo 3d spectra; the amount of NiMoS phase from the Ni 2p spectra.

With the aim of providing a coherent understanding of the results described in this chapter, **Appendix A** further describes the characterization techniques that were used to assess the properties of the modified zeolite and the hydrocracking catalysts.

2.2.4. Activity evaluation of hydrocracking catalysts

Hydrocracking activity tests were performed with the NiMoP-based catalysts. The feedstock was a Rubiales pre-treated vacuum gas oil with the following properties: density = 0.91 g/cm^3, S content = 43 ppm, N content = 25 ppm, aniline point = 79.9 °C. The catalysts were placed in a ½ inch internal diameter stainless-steel tubular reactor arranged in downflow mode (*Parr Instruments*). In a typical run, 4.2 g of the catalysts was diluted with inert sand (40/60 weight ratio). The reaction bed volume was approximately 8 cm^3. Spherical glass beads were loaded on top and bottom of the catalyst bed to ensure good mixing and heat transfer.

The catalysts were sulfided *in situ* following a slow heating ramp (10 °C/h) to 345 °C with a diesel feed containing 4 wt.% of dimethyl disulfide and 0.5 wt.% of aniline. The sulfidation temperature was maintained for 12 h before the VGO admission. The hydrocracking reaction conditions were 345 °C, 1500 psig, H_2/feed volume ratio 1250 NL/L, and the weight hourly space velocity (WHSV) was 1 h^{-1}. Products were analyzed by gas chromatography coupled to simulated distillation (SimDis-GC) according to the

ASTM D7213 standard test method. Conversion and yields were calculated as in [39] with the following equations.

$$Conversion(\%) = \left(\frac{wt.\%\ fraction\ {}^{370+}_{feed} - wt.\%\ fraction\ {}^{370+}_{products}}{wt.\%\ fraction\ {}^{370+}_{feed}} \right) x100$$

$$Yield\ _{MD}(\%) = \left(\frac{wt.\%\ fraction\ {}^{180to370}_{products} - wt.\%\ fraction\ {}^{180to370}_{feed}}{wt.\%\ fraction\ {}^{370+}_{feed}} \right) x100$$

$$Yield\ _{naphtha}(\%) = \left(\frac{wt.\%\ fraction\ {}^{IBP\ to\ 180}_{products} - wt.\%\ fraction\ {}^{IBP\ to180}_{feed}}{wt.\%\ fraction\ {}^{370+}_{feed}} \right) x100$$

Conversion was referred to the 370 °C^{+} cut in the feed. Yield to middle distillates (MD) was referred to the fraction 180 - 370 °C in the product mixture (obtained from the SimDis-GC data). Yield to naphtha was referred to the fraction IBP - 180 °C (IPB, initial boiling point). Conversions values are reported from the average of several liquid product samples taken from 50 to 80 h on stream. The experimental error in conversion was determined to be below 2% by performing three different runs with a selected catalyst at the same conditions.

2.3. RESULTS AND DISCUSSION

2.3.1. XRD patterns

XRD patterns of the zeolites samples are presented in **Figure 2.1**. Both the number of peaks and peak positions agree well with the powder diffraction pattern of a typical Ultrastable Y zeolite (FAU framework type) reported by The International Zeolite Association (IZA) [40]. It can be noted that the treatments do not drastically affect the crystalline order of the USY zeolites. Additionally, diffuse scattering effects from X-ray amorphous non-framework species such as silica and silica-alumina, which are typically observed in the 2θ region between 20 and 30°, remain low for all the zeolite samples.

Figure 2.1. XRD patterns of the zeolite samples.

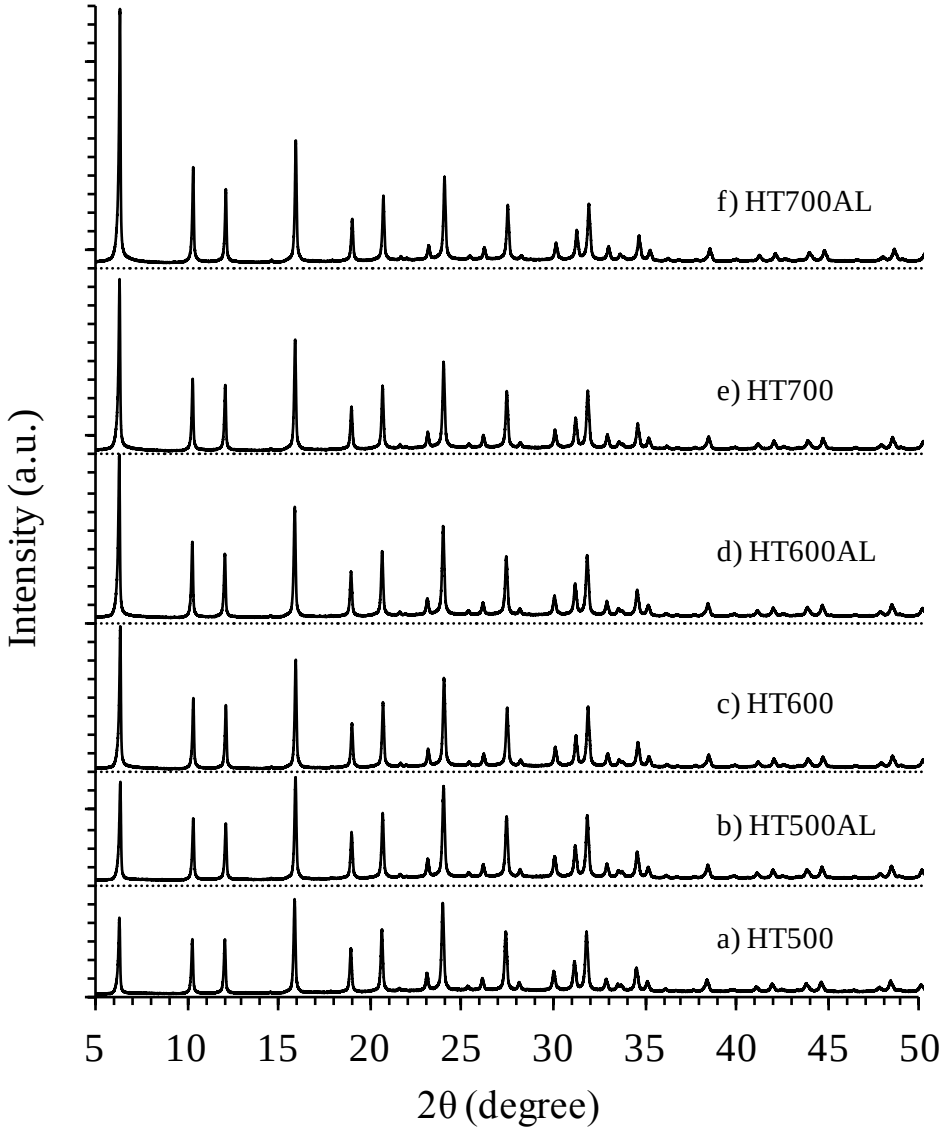

2.3.2. Textural characterization

Figure 2.2 presents the nitrogen adsorption and desorption isotherms of the modified USY zeolites. The samples show type IV isotherms with hysteresis loops indicative of materials possessing both micro and mesoporosity. The progressive change to upward curvature in the hysteresis loop for the steam-treated samples at increasing treatment temperature is indicative of development of cylindrical type of pores.

Figure 2.2. Nitrogen adsorption-desorption isotherms of the modified zeolites. a) HT500, b) HT500AL, c) HT600, d) HT600AL, e) HT700 and f) HT700AL zeolites. For better visualization, curves were vertically shifted according to the following values: a) no shift, b) 0.3 mmol/g, c) 3 mmol/g, d) 3.5 mmol/g, e) 7 mmol/g and f) 8.5 mmol/g.

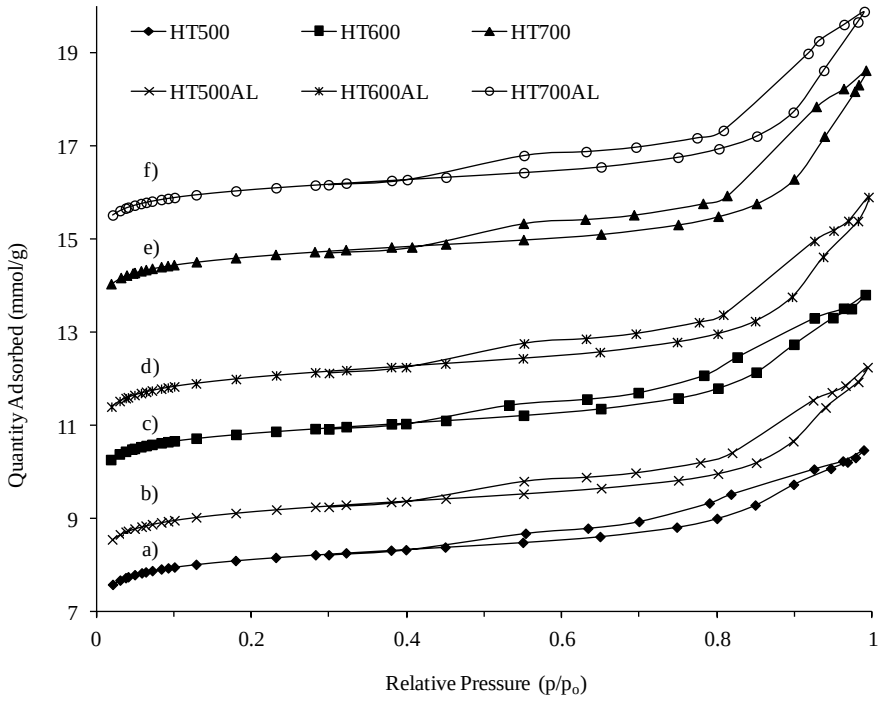

The pore size distributions (PSD) in the mesopore range are given in **Figure 2.3**. All materials have a relatively wide distribution of mesopore sizes with maxima at 160 Å for HT500 and HT600; upon acid treatment, the maxima shift to 220 Å, which should be the consequence of the removal of polymerized EFAl that obstruct the mesopore system. HT700 and HT700AL zeolites have similar mesopore size distributions.

The main textural properties of the modified zeolites are presented in **Table 2.1**. It is seen that the total surface area and micropore volume decrease with increasing temperature of the hydrothermal treatment step. At the same time, the mesopore and total pore volume increase slightly. These changes are due to the structural collapse of the zeolite [1]. During hydrothermal treatment, Al atoms are extracted from the framework. Framework dealumination involves the disassembly of the sodalite cages and also some supercages, resulting in formation of mesopores with sizes in the range of 5-50 nm [5].

Figure 2.3. Mesopore size distributions of the modified zeolites from the nitrogen adsorption isotherms (BJH method). a) HT500 and HT500AL zeolites, b) HT600 and HT600AL zeolites, c) HT700 and HT700AL zeolites.

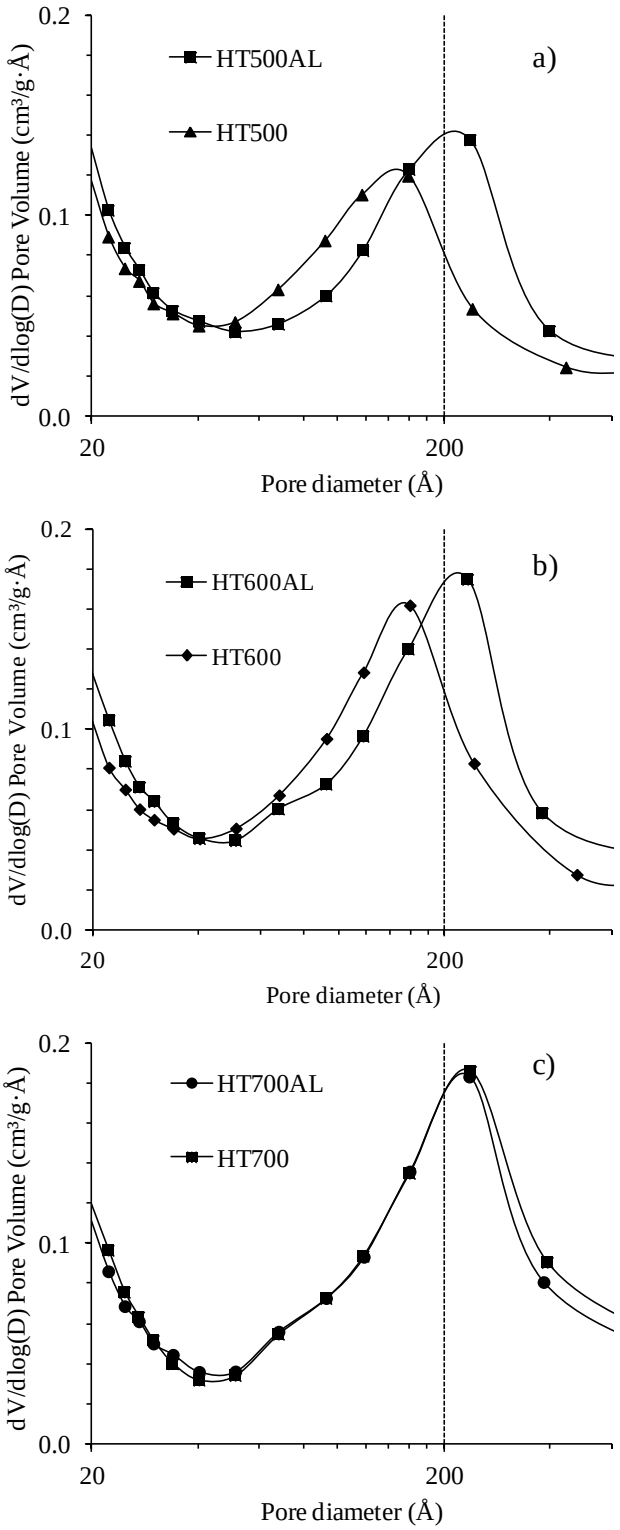

Table 2.1. Textural properties of the modified zeolites.

Property	HT500	HT600	HT700	HT500AL	HT600AL	HT700AL
S_{BET} (m^2/g)[a]	666	653	635	737	710	630
S_{micro} (m^2/g)[b]	599	575	551	650	620	549
V_{total} (cm^3/g)[c]	0.36	0.38	0.40	0.41	0.43	0.40
V_{micro} (cm^3/g)[d]	0.25	0.24	0.23	0.27	0.26	0.23
V_{meso} (cm^3/g)[e]	0.11	0.14	0.17	0.14	0.17	0.17

[a] BET surface area, [b] Microporous surface area, [c] Total pore volume, [d] Microporous pore volume (t-plot method), [e] Mesoporous pore volume.

After HCl leaching, the micro- and mesoporosity of the zeolites hydrothermally treated at 500 and 600 °C (samples HT500AL and HT600AL) improved. The increase in the mesopore volume is in line with findings reported in literature [41]. It has been ascribed to the removal of EFAl species formed during steaming that block the pore system [42]. Acid leaching in sample HT700 results in a different behavior with little change in the textural properties. This is presumably because the chosen leaching conditions were too mild to extract the kind of EFAl species present in the starting zeolite (HT700). Those are presumed to be of high polymeric nature.

2.3.3. Morphological characterization

The morphology of the zeolite particles and the mesopore network were examined by high resolution transmission electron microscopy (HRTEM). **Figure 2.4** presents representative HRTEM images of the HT600 and HT600AL zeolites. The images indicate that the morphology of the grains, as shown in **Figs. 2.4a** and **2.4b**, is similar in either the steam-treated or the acid-leached zeolite. Additionally, by comparison of several images before and after acid leaching, it is deduced that the acid treatment did not result in fragmentation of crystals; accordingly, considerable changes in the overall zeolite morphology due to the acid treatment are absent. **Figure 2.4b** also reveals the characteristics of the mesopore system in the acid-treated zeolite. Mesopores are distinguishable as lighter zones, typically concentrated in the interior of the grains, while the smooth dark zones relate to the unaffected microporous regions of the crystals. In this zeolite sample, some intra-crystalline voids coalesce to form channel-

like mesopores. In general, an inhomogeneous distribution of mesopores is observed among different zeolite grains and within individual grains. **Figure 2.4c** presents an image of a HT600 zeolite crystal at increased magnification. Some crater-like mesopores at the exterior surface of the zeolite particle are clearly noticeable. These mesopores have pore diameters close to the average value obtained from the nitrogen adsorption data (**Figure 2.3**). **Figure 2.4d** shows the formation of channels along crystals defects in the HT600AL zeolite, visibly connected to the outer surface of the crystals. The features observed by HRTEM are in general agreement with other studies of chemically-treated USY zeolites [5, 16].

Figure 2.4. HRTEM images of USY-HT600 and USY-HT600AL zeolites. a) HT600, b) HT600AL, c) HT600 and d) HT600AL.

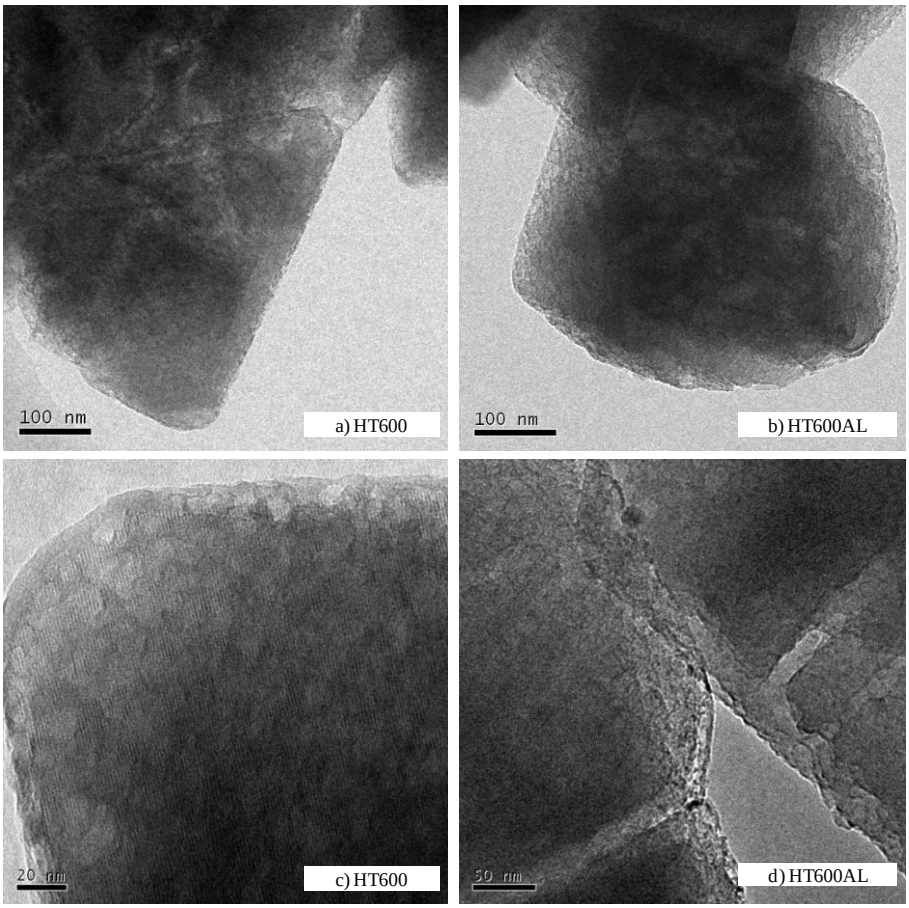

2.3.4. Nuclear Magnetic Resonance characterization

2.3.4.1 ^{29}Si MAS NMR characterization

The changes in the distribution of the different Si species during the hydrothermal treatment and acid leaching were followed by ^{29}Si MAS NMR. The experimentally obtained and deconvoluted ^{29}Si MAS NMR spectra of the samples are shown in **Figure 2.5**. In all the modified zeolites, silicon species with 0Al neighbors (Si(0Al)) dominate the spectra. This feature becomes more notorious in zeolites steam-treated at higher temperature. This directly indicates that aluminum is progressively removed from the framework during steaming with increasing treatment temperature. Additionally, acid leaching treatment slightly changes the Si species distribution in the zeolites.

Figure 2.5. ^{29}Si MAS NMR spectra of the hydrothermally and acid treated zeolites. a) HT500, b) HT500AL, c) HT600, d) HT600AL, e) HT700 and f) HT700AL. The different deconvoluted signals for the Si environments are shown in b) as dashed lines. See the experimental section 2.2.2.4 for further details about the fitting.

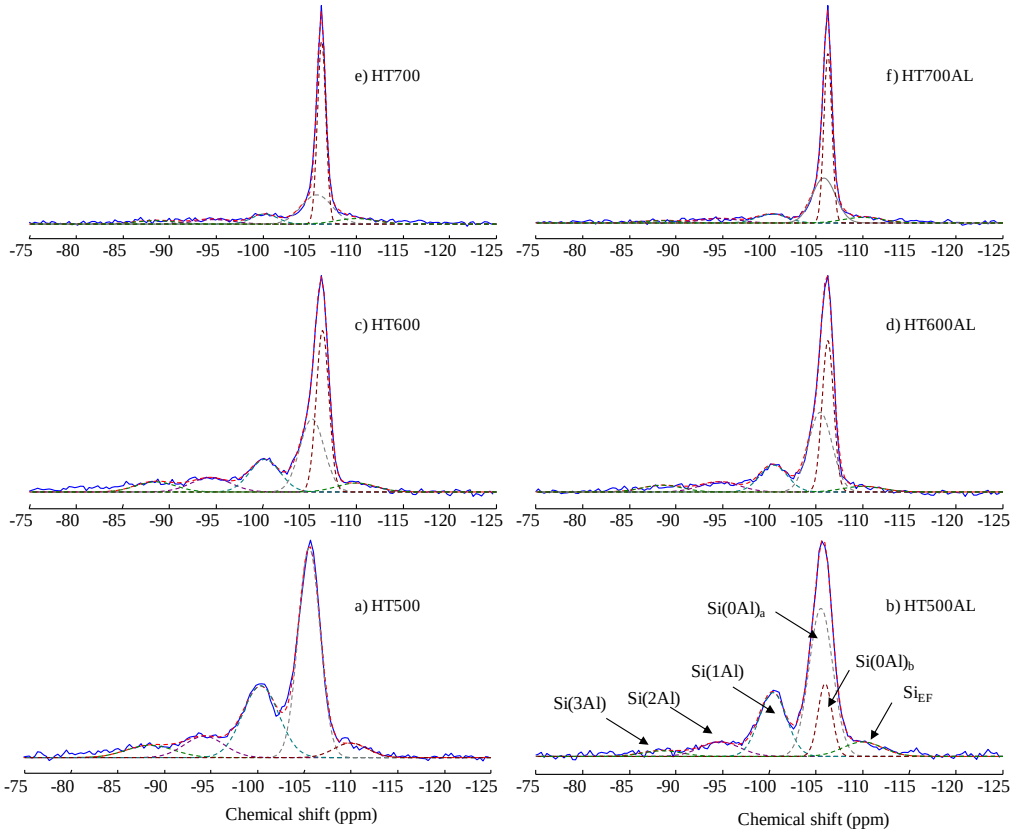

The relative intensities of the peaks associated to each Q^4(nAl) environment are presented in **Table 2.1**. The decrease of relative intensities of Si(3Al), Si(2Al) and Si(1Al) species, and the increase of that of Si(0Al) species, evidence the progressive dealumination with increasing treatment temperature. Additionally, acid leaching induces further dealumination.

Table 2.2. Relative intensities of deconvoluted signals from ^{29}Si MAS NMR spectra.

Signal		HT500	HT500AL	HT600	HT600AL	HT700	HT700AL
Si(3Al)	δ (ppm)	-88.5	-88.5	-88.5	-88.5	-88.5	-88.5
	$I_{Si(3Al)}$ (%)	6.5	3.0	6.8	5.4	4.5	3.2
Si(2Al)	δ (ppm)	-94.3	-94.7	-94.4	-94.7	-94.7	-94.7
	$I_{Si(2Al)}$ (%)	9.0	7.4	9.2	7.6	6.2	5.6
Si(1Al)	δ (ppm)	-100.3	-100.4	-100.2	-100.6	-100.2	-100.3
	$I_{Si(1Al)}$ (%)	28.6	23.0	16.1	16.8	7.6	8.6
$Si(0Al)_a$	δ (ppm)	-105.5	-105.5	-105.2	-105.5	-105.8	-105.8
	$I_{Si(0Al)}$ (%)	50.6	45.9	29.0	36.4	27.9	33.2
$Si(0Al)_b$	δ (ppm)		-106.0	-106.4	-106.3	-106.3	-106.3
	$I_{Si(0Al)}$ (%)		13.4	33.0	27.9	46.9	41.8
Si_{EF}	δ (ppm)	-110.0	-110.0	-110.0	-110.0	-110.0	-110.0
	$I_{Si(EF)}$ (%)	5.3	7.4	5.8	5.9	7.0	7.6

2.3.4.2 ^{27}Al MAS NMR characterization

The evolution of the coordination of the Al species in the samples due to hydrothermal and acid leaching treatments was followed by ^{27}Al NMR spectroscopy. Three main peaks are observed in the spectra for all of the zeolites shown in **Figure 2.6**, namely at 60, 30 and 0 ppm. The signals at 60 and 0 ppm are due to Al nuclei in tetrahedral and octahedral coordination environment, respectively [43-45]. The signal at 30 ppm is assigned to distorted tetrahedral or five-coordinated Al species (extraframework) [45-47]. Increasing the temperature of hydrothermal treatment from 500 to 600 °C increases the 30 ppm band. For the sample steam-treated at 700 °C the contributions of the three main bands becomes nearly equal, which points to the highest degree of dealumination and considerable heterogeneity in the Al coordination. Acid leaching causes the decrease of the band at 30 ppm and sharpening of the octahedral Al region in samples HT500AL and HT600AL. It points to removal of EFAl species. Nevertheless, a significant amount of EFAl species (penta- and hexa-coordinated Al) resisted acid leaching. According to literature, acid leaching removes preferentially amorphous

material and Al linked to the framework [47, 48]. The changes in the NMR spectra therefore indicate that a separate extraframework silica-alumina phase is removed by acid leaching. The EFAl contribution is highest in the HT700AL sample with respect to its parent zeolite HT700. This result indicates that the acid leaching in the HT700 sample was not as effective as for the milder steamed samples, presumably because of the higher degree of agglomeration of the EFAl phase.

Figure 2.6. ^{27}Al MAS NMR spectra of the hydrothermally and acid treated zeolites. a) HT500, b) HT500AL, c) HT600, d) HT600AL, e) HT700 and f) HT700AL.

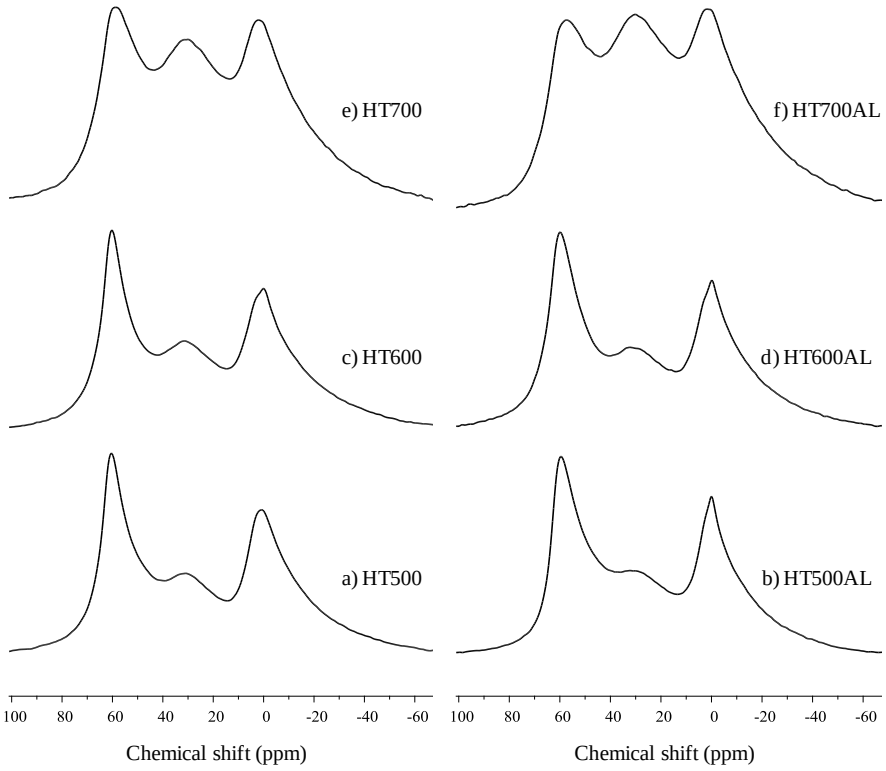

2.3.5. Compilation of the main physicochemical properties of the zeolites

The most important properties including the unit cell parameters, the bulk, framework and surface Si/Al ratios of the modified zeolites are presented in **Table 2.3**.

Hydrothermal treatment did not change the bulk Si/Al ratios of the samples. On the contrary, acid leaching increased the bulk Si/Al as a result of the removal of Al. The degree of Al removal is, however, relatively low for the acid leaching treatment employed here. It is largest for the acid leached sample that was steam-treated at 500

°C. It has been established that the temperature of steam dealumination influences the EFAl speciation [49]. At higher steaming temperature the amount of polymerized EFAl species increases. The difficulty in removing EFAl species can therefore be related to their higher degree of agglomeration [4].

Table 2.3. Structural properties of the modified zeolites.

Property	HT500	HT600	HT700	HT500AL	HT600AL	HT700AL
$(Si/Al)_{bulk}$	3.1	3.1	3.1	3.8	3.6	3.5
$(Si/Al)_{surface}$ [a]	1.8	1.5	1.2	3.0	2.6	2.0
$(Si/Al)_{framework}$ [b]	5.7	6.8	11.1	7.9	8.5	12.6
a_o (Å)[c]	24.389	24.359	24.334	24.396	24.346	24.300

[a] From XPS, [b] Framework Si/Al ratio from ^{29}Si MAS NMR, [c] Unit cell size from XRD.

The framework Si/Al ratios (as obtained from ^{29}Si MAS NMR with the data of **Table 2.2)** are also presented in **Table 2.3**. It can be observed that the framework Si/Al ratios gradually increase with the temperature of steaming. This is expected and points to progressive dealumination of the framework [50]. There is also a significant difference between the bulk and framework Si/Al values for the hydrothermally treated samples. The difference becomes larger with the steaming temperature. This shows that more severe steam treatment results in more EFAl species. Comparison of the framework Si/Al ratios and the unit cell sizes before and after acid leaching shows that this treatment caused further dealumination of the framework. Accordingly, it is concluded that acid leaching by HCl does not only remove EFAl species but also further dealuminates the framework. The results presented in **Table 2.3** agree with the structural characterization obtained by ^{29}Si and ^{27}Al MAS NMR with respect to the framework Al content and the degree of bulk dealumination following acid leaching treatment.

XPS analysis shows that surface Si/Al ratios are lower than the corresponding bulk values for the hydrothermally treated zeolites. It points to migration of EFAl species to the external surface of the zeolite crystals [51]. The migration of EFAl species is more substantial for the samples steamed at higher temperatures. For acid leached zeolites, the surface Si/Al increases, which implies the removal of Al from the external surface

region of the zeolite crystals. Al is assumed to be removed by dissolution of EFAl species and part of the remaining framework Al [43].

In brief, the results presented above show that an increasing amount of Al is removed from the framework with increasing hydrothermal treatment temperature. This treatment gradually lowers the micropore surface area by formation of mesopores. At the same time, the surface Si/Al decreases due to migration of Al to the surface region. Acid leaching extracts some of the EFAl species and, consequently, improves the accessibility of the micropores and mesopores. Acid leaching also leads to some further framework dealumination.

2.3.6. Acid properties characterization

2.3.6.1. FTIR spectroscopy of hydroxyl groups

The Brønsted acidity of zeolites is mainly related to bridging hydroxyl groups. Infrared spectra of the zeolite samples in the OH stretching region are presented in **Figure 2.7**. The spectra show at least five bands at around 3562, 3600, 3625, 3670 and 3739 cm^{-1}. However, according to the literature all of these bands are overlapped by other OH stretching vibrations [52]. The bands at 3562 and 3625 cm^{-1} correspond to bridged Si-(OH)-Al Brønsted acid sites located in the sodalite cages (low-frequency, LF) and in the supercages (high-frequency, HF), respectively [53]. The band at around 3600 cm^{-1} is attributed to a high-frequency OH group perturbed by the interaction with Lewis sites present in EFAl species generated during steam dealumination [54]. The band at 3670 cm^{-1} is assigned to hydroxyl groups of Al-OH species present in extraframework positions [55]. The asymmetric band with a maximum at 3739 cm^{-1} corresponds to the superposition of several types of silanol groups [31].

According to **Figure 2.7**, when the temperature of hydrothermal treatment increases from 500 to 600 °C (spectra a and c), the amount of HF and LF hydroxyl groups slightly diminished. However, steam treatment at 700 °C (spectrum e) led to a strong decrease of the intensities of the HF and LF OH bands. It shows considerable framework dealumination and depletion of the Brønsted acidity. At the same time, structural defects developed, as indicated by the sharpening of the signal at 3739 cm^{-1} assigned to terminal Si-OH groups. Acid leaching mainly increases the intensity of the band at 3600 cm^{-1} for the zeolite hydrothermally treated at 500 °C (spectra a and b). For the other two steam-treated zeolites, the effect of acid leaching is very small. The band at around 3600

cm^{-1} has been extensively discussed in literature, because it has been linked to the increased acidity usually observed in USY zeolites [10, 56].

Figure 2.7. FTIR spectra in the OH region for the zeolite samples. a) HT500, b) HT500AL, c) HT600, d) HT600AL, e) HT700, f) HT700AL. Positions for the main bands are indicated with dashed lines. Spectra were taken at 150 °C after evacuation in vacuum at 500 °C.

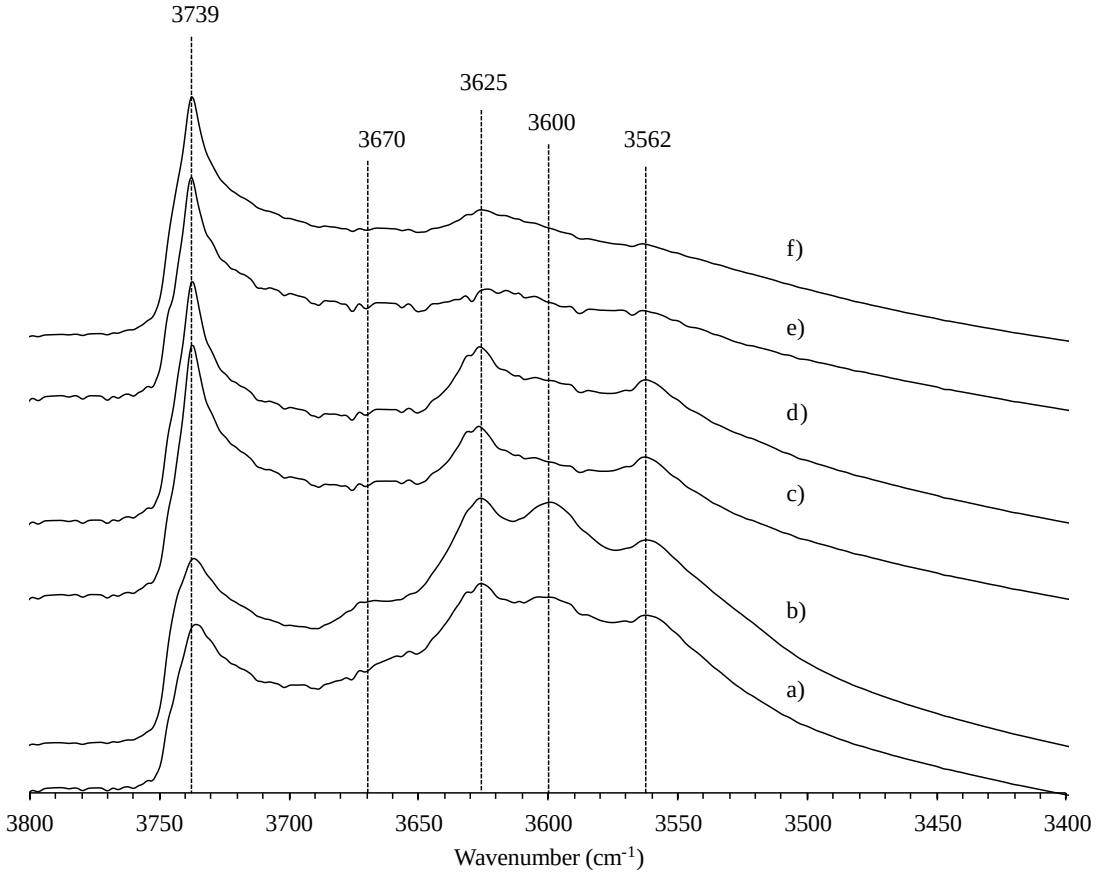

2.3.6.2. FTIR measurements of adsorbed pyridine

Further acidity characterization was done by FTIR spectroscopy of adsorbed pyridine. The spectra of the zeolite samples in the region of the bands associated to Brønsted and Lewis acid sites after adsorption and desorption of pyridine is included in **Appendix B1**. The quantitative data are reported in **Table 2.4**. It is seen that higher hydrothermal treatment temperature led to zeolites with lower Brønsted acid site content. This can be directly correlated to framework dealumination. At the same time, the fraction of strong Brønsted acid sites is also decreasing (B_{strong}/B_{total} ratios). Acid leaching increases the

total number of Brønsted acid sites, mainly by increasing the number of medium and strong acid sites for zeolites hydrothermally treated at 500 and 600 °C. The zeolite steam-treated at 700 °C and its acid-leached counterpart (HT700AL) behave differently. The increase in Brønsted acid site content after acid leaching can be explained by enhanced access of pyridine to the inner parts of the zeolite, because polymerized Al species obstructing the pore system have been partially removed. The increase in acid strength shown by the acid leached zeolites HT500AL and HT600AL is explained by the removal of some non-framework aluminum species acting as charge-balancing cations [42]. The pyridine IR results also show that the Lewis acid site content was slightly decreased by the acid leaching treatment in all cases. This can be directly related to the removal of EFAl species. Acid leaching of HT700 results in a zeolite with a higher Lewis to Brønsted acid site ratio (HT700AL) than the other samples.

Table 2.4. Acidity characterization by FTIR spectroscopy of adsorbed pyridine.

Zeolite	Brønsted acid sites (mmol/g)			Lewis acid sites (mmol/g)	B_{strong}/B_{total} [d]	L_{total}/B_{total} [e]
	Total[a]	Medium[b]	Strong[c]	Total[a]		
HT500	0.56	0.44	0.13	0.61	0.23	1.09
HT500AL	0.66	0.54	0.20	0.57	0.30	0.86
HT600	0.40	0.28	0.07	0.45	0.18	1.13
HT600AL	0.43	0.31	0.08	0.41	0.19	0.95
HT700	0.29	0.18	0.03	0.32	0.10	1.10
HT700AL	0.22	0.15	0.03	0.28	0.14	1.27

[a] Acid sites after desorption at 150 °C,

[b] Acid sites after desorption at 300 °C.

[c] Acid sites after desorption at 500 °C.

[d] Strong Brønsted acid sites over total Brønsted acid sites.

[e] Total Lewis acid sites over total Brønsted acid sites.

In summary, acidity characterization shows that increasing severity of the steam-calcination step lowers the amount of Brønsted acid sites. This is a consequence of framework dealumination. Acid leaching treatment significantly increases the number of medium and strong Brønsted acid sites, presumably as a result of the removal of

charge-balancing EFAl species. Removal of these and more agglomerated forms of EFAl leads to better accessibility of the acid sites.

2.3.7. Characterization of NiMoP supported catalysts

2.3.7.1. Textural properties and chemical composition

The main textural properties and the chemical composition of final NiMoP-suported hydrocracking catalysts in oxide state are presented in **Table 2.5.** The textural properties of the hydrocracking catalysts follow the trends seen for the parent zeolites (reported in **Table 2.1**). The metals and phosphorous loadings were lower than the intended values. However, similar Ni/Mo ratios were obtained for all the catalysts.

Table 2.5. Textural properties and chemical composition of NiMoP-suported hydrocracking catalysts in oxide state.

Sample	Textural properties		Chemical composition			
	S_{BET} (m^2/g)	V_{total} (cm^3/g)	NiO (wt.%)	MoO_3 (wt.%)	P_2O_5 (wt.%)	Ni/Mo
NiMoP/(HT500+Alumina)	303	0.30	2.6	13.0	2.0	0.39
NiMoP/(HT600+Alumina)	300	0.29	2.9	14.0	2.1	0.40
NiMoP/(HT700+Alumina)	295	0.28	2.8	14.1	2.2	0.40
NiMoP/(HT500AL+Alumina)	336	0.33	2.9	14.3	2.3	0.41
NiMoP/(HT600AL+Alumina)	325	0.32	3.0	13.7	2.4	0.43
NiMoP/(HT700AL+Alumina)	268	0.30	2.7	13.9	2.6	0.38

2.3.7.2. UV–Vis DRS

UV–Vis DRS measurements allow to obtain information regarding the Ni and Mo oxide species in the catalysts. **Figure 2.8** presents the UV-Vis DRS spectra of the supported NiMoP catalysts in calcined form (oxide). The UV-Vis DRS spectra are constituted by a single broad band with maximum at approximately 240 nm due to contributions of both isolated molybdate (tetrahedral Mo) and polymolybdate (octahedral Mo) species [57, 58]. In the 500–900 nm region contributions of tetrahedral Ni and octahedral Ni in NiO were also detected. Spectra for all the catalysts are very similar indicating that the different zeolite characteristics in the carrier do not impact the coordination symmetry of the supported Mo and Ni. All the catalysts have a similar proportion of different types of Mo species.

Figure 2.8. UV-Vis DRS spectra of the supported NiMoP catalysts in oxide form. a) NiMoP/(HT500 + Alumina), b) NiMoP/(HT500AL + Alumina), c) NiMoP/(HT600 + Alumina), d) NiMoP/(HT600AL + Alumina), e) NiMoP/(HT700 + Alumina), f) NiMoP/(HT700AL + Alumina).

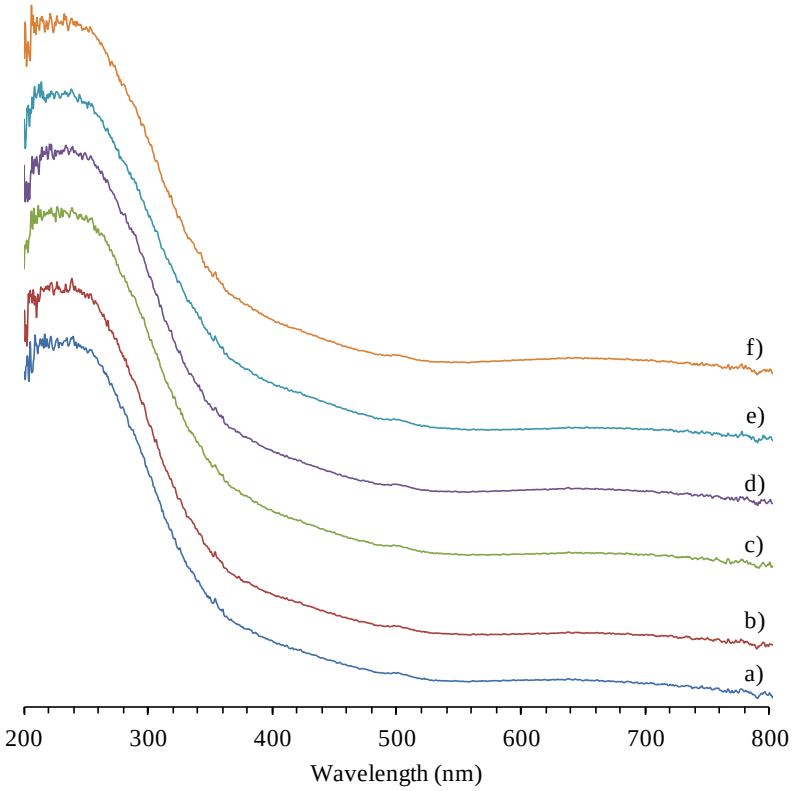

2.3.7.3. Laser Raman spectroscopy (LRS)

The Raman spectra of the NiMoP-supported hydrocracking catalysts in oxide state are presented in **Figure 2.9**. The dominant spectral features are very similar for all the samples indicating that the same types of metal oxides species are formed in the calcined catalysts. Spectra exhibit three Mo-characteristic frequency ranges of vibrational modes at three wavenumber ranges, namely, 200-250, 300-350, and 850-1000 cm^{-1} which are usually assigned respectively to Mo-O-Mo deformation, Mo=O bending vibrations, and symmetric and antisymmetric Mo=O terminal stretches [57, 59-61]. Particularly, the intense peak centered at 950 cm^{-1} is ascribed to the symmetric stretching of Mo=O bond in two-dimensional polymeric forms of octahedrally

coordinated Mo oxide species. Additionally, the bands around 550-600 cm^{-1} can be assigned to SiO vibrations. The band at 500 cm^{-1} is due to the zeolite framework symmetric bending vibration. Aside from the zeolite-related bands, the spectra compare well with previous LRS studies on NiMo/Alumina catalysts [61-63]. In short, the most important information derived from the LRS spectra of the present study is the absence of two sharp and intense peaks at 995 and 820 cm^{-1} characteristic of free MoO_3 aggregates [60] which is an indication that the preparation method yields in catalysts where Mo is well dispersed on the carrier materials. The presence of MoO_3 is undesirable because this oxide is reluctant to sulfidation into MoS_2 [38].

Figure 2.9. Raman spectra of the NiMoP supported catalysts (oxide state). a) NiMoP/(HT500 + Alumina), b) NiMoP/(HT500AL + Alumina), c) NiMoP/(HT600 + Alumina), d) NiMoP/(HT600AL + Alumina). Data not available for catalysts based on HT700 and HT700AL zeolites.

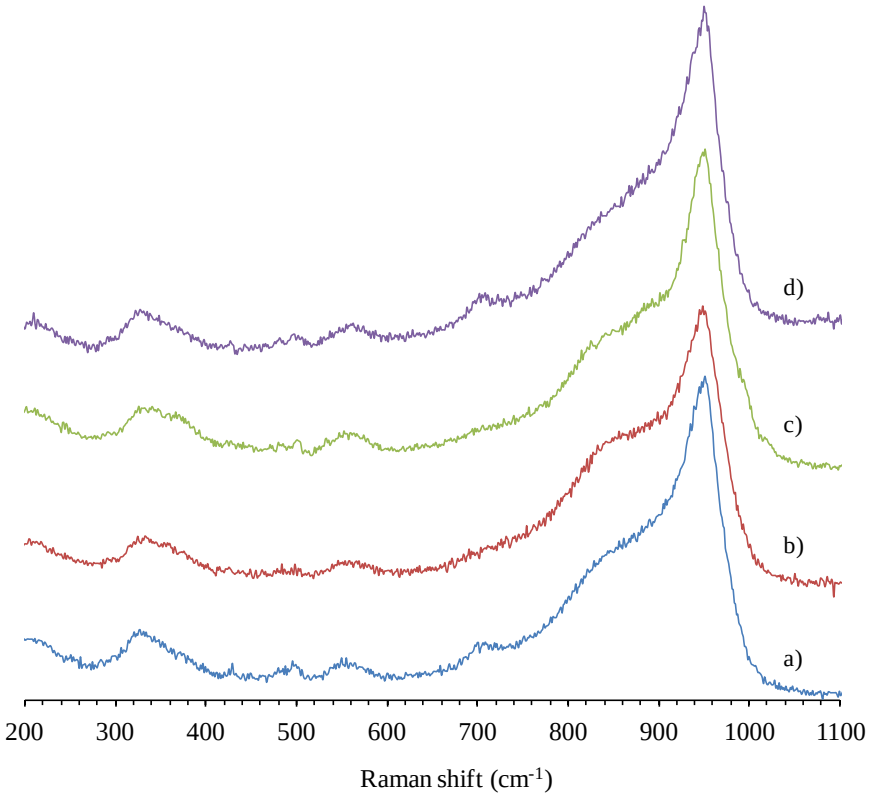

2.3.7.4. XPS spectroscopy of sulfided NiMoP catalysts

XPS surface analysis was performed to the NiMoP-suported hydrocracking catalysts after sulfidation in H_2S/H_2 flow. Mo 3d spectra of the sulfided NiMoP catalysts are presented in **Figure 2.10** with the corresponding deconvoluted peaks (details in experimental section). Evidently, Mo-sulfide species are predominant in all samples. Both the Mo $3d_{5/2}$ binding energy (228.9 eV) and the shape of each spectrum are characteristic of typical MoS_2 structures.

Figure 2.10. XPS Mo 3d spectra of the NiMoP catalysts after sulfidation in H_2S flow. a) NiMoP/(HT500 + Alumina), b) NiMoP/(HT500AL + Alumina), c) NiMoP/(HT600 + Alumina), d) NiMoP/(HT600AL + Alumina), e) NiMoP/(HT700 + Alumina), f) NiMoP/(HT700AL + Alumina). The spectra were decomposed into oxide, oxysulfide and sulfide components, as shown in a).

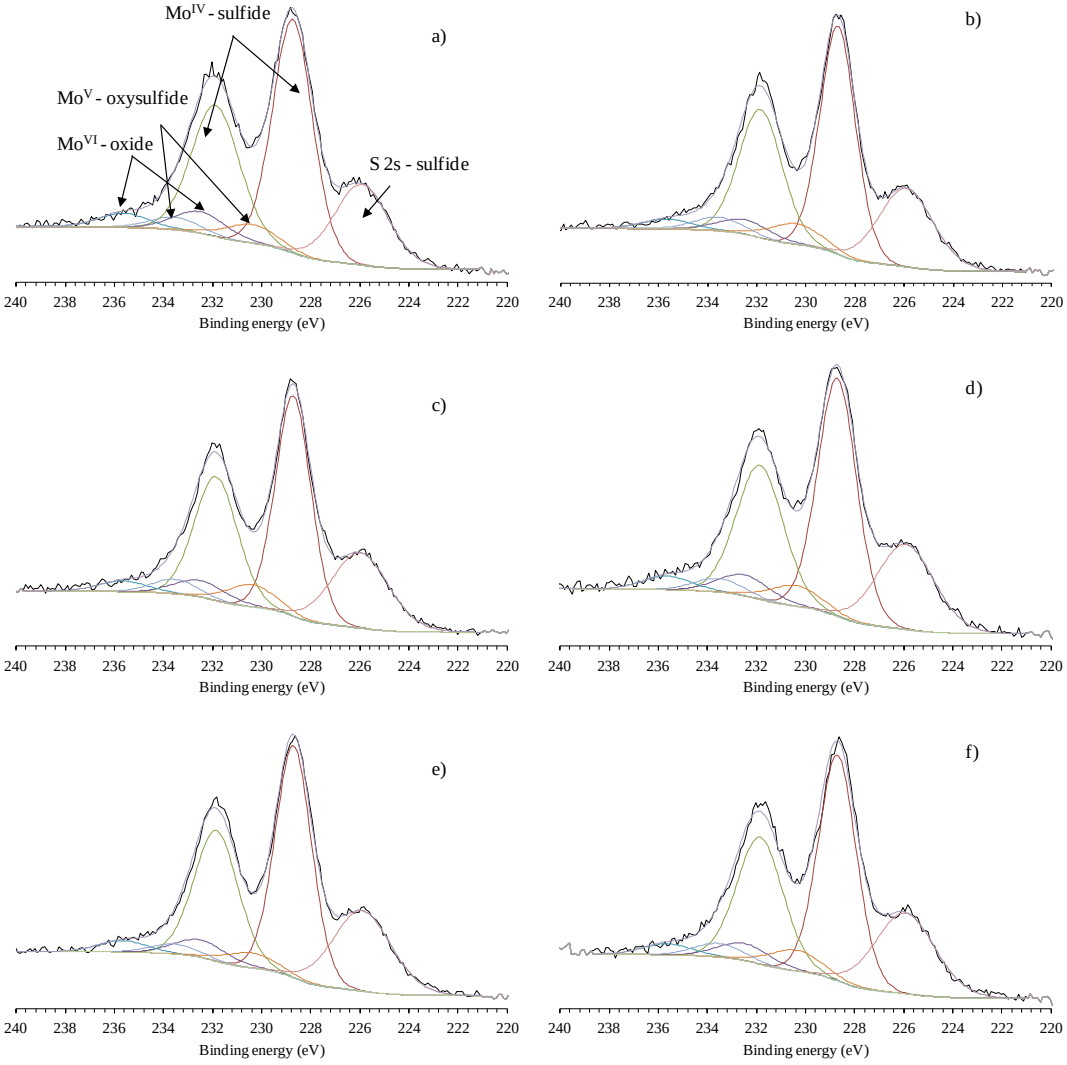

Figure 2.11 presents the Ni 2p spectra with the corresponding deconvoluted peaks for the $2p_{3/2}$ envelope. Again, no substantial differences are noted among the spectra of the catalysts.

Figure 2.11. XPS Ni 2p spectra of the NiMoP catalysts after sulfidation in H_2S flow. a) NiMoP/(HT500 + Alumina), b) NiMoP/(HT500AL + Alumina), c) NiMoP/(HT600 + Alumina), d) NiMoP/(HT600AL + Alumina), e) NiMoP/(HT700 + Alumina), f) NiMoP/(HT700AL + Alumina).

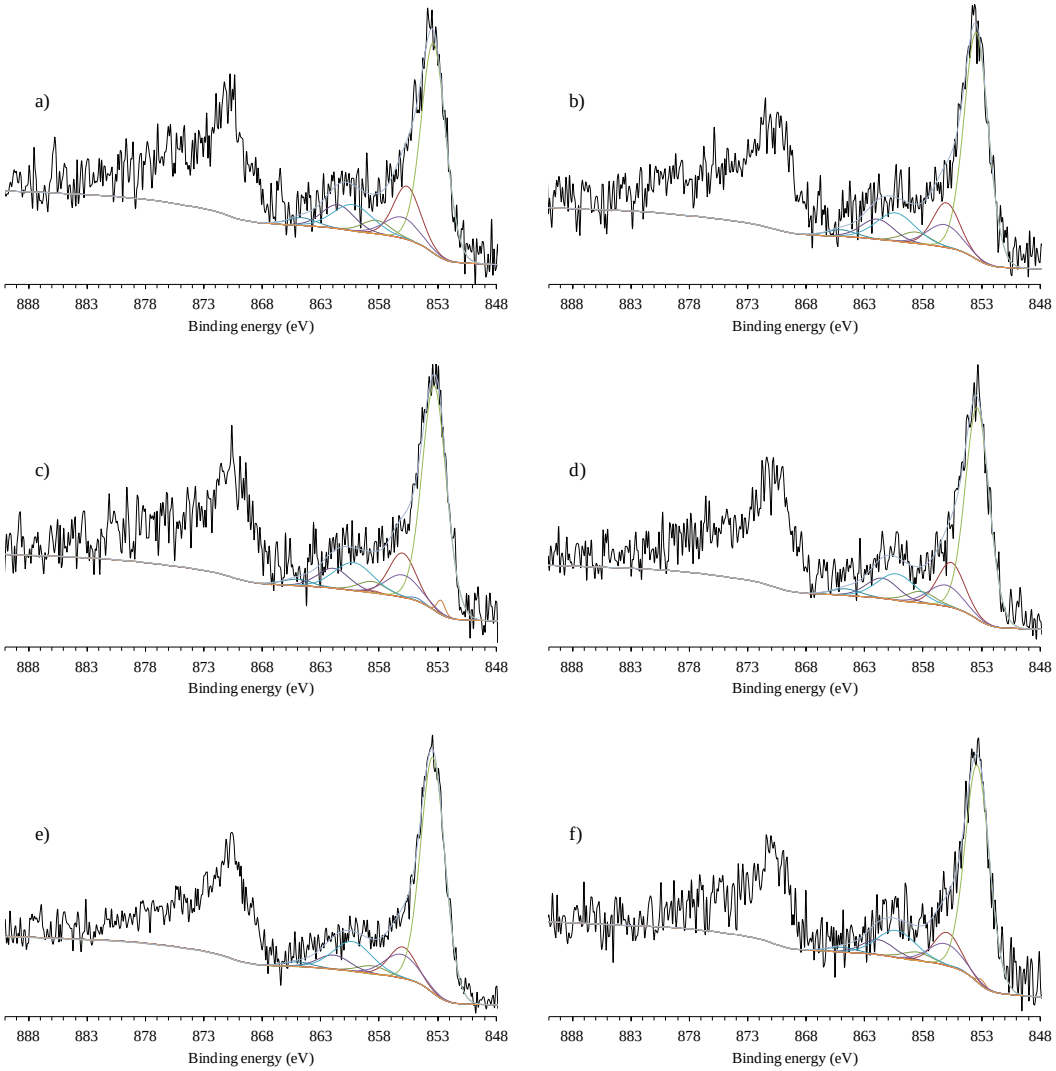

Table 2.6 shows the binding energies and atomic contents of the different Mo species for the catalysts in sulfided state. It can be seen that there is no significant differences in the binding energy (BE) of the Mo species among the sulfide catalysts, which suggests that there were no electronic effects coming from the supports [38]. Under the sulfidation conditions employed for the XPS tests, the atomic fractions of Mo species on the surface are similar in all the catalysts. Mo^{IV} species relative content (sulfidation degree) represents 81–84% of the total Mo on the samples under the sulfidation conditions used for this analysis. Species S_2^{2-} was not detected in significant relative amounts in any sample.

Table 2.6. XPS parameters of the different contributions of Mo 3d spectra obtained for the supported NiMoP catalysts in sulfided state.

Catalyst	Mo^{IV}		Mo^{V}		Mo^{VI}	
	BE (eV)	at%	BE (eV)	at%	BE (eV)	at%
NiMoP/(HT500 + Alumina)	228.7	82	230.4	8	232.5	10
NiMoP/(HT500AL + Alumina)	228.7	82	230.4	10	232.5	7
NiMoP/(HT600 + Alumina)	228.7	81	230.4	11	232.5	9
NiMoP/(HT600AL + Alumina)	228.7	82	230.4	9	232.5	9
NiMoP/(HT700 + Alumina)	228.7	84	230.4	7	232.5	9
NiMoP/(HT700AL + Alumina)	228.7	82	230.4	10	232.5	8

The relative quantities of Ni species (Ni^{II} oxide, NiS_x, and NiMoS) are presented in **Table 2.7**. The data indicate that a high proportion of nickel atoms are engaged forming NiMoS phase in all samples. In brief, XPS analyses do not reveal pronounced differences among samples in terms of sulfidability.

In summary, the characterization of the NiMoP-supported catalysts showed only minor differences in the dispersion of the NiMo-oxide components and in the metal-support interactions. UV-Vis DRS results indicate that the different characteristics of the modified zeolites in the supports do not influence the coordination of the supported Mo and Ni. According to LRS results, the lack of two sharp and intense peaks at 995 and 820 cm^{-1} characteristic of free MoO_3 aggregates point out that Mo is well dispersed on

the carrier materials. XPS analysis indicates that all the catalysts can reach similar sulfidation degrees and NiMoS phase contents independently of the features of the zeolite component in the supports. The above observed behaviors are to be expected because the (de)-hydrogenation components will be mainly deposited on the alumina part of the composite catalyst because the incorporation of Mo into the porous structure of the zeolite is usually restricted [64, 65].

Table 2.7. XPS parameters of the different contributions of Ni $2p_{3/2}$ spectra obtained for the supported NiMoP catalysts in sulfided state.

Catalyst	NiMoS phase		NiS_x		Ni^{II} - oxide	
	BE (eV)	at%	BE (eV)	at%	BE (eV)	at%
NiMoP/(HT500 + Alumina)	853.3	71	852.7	0	855.6	29
NiMoP/(HT500AL + Alumina)	853.4	76	853.0	0	856.0	24
NiMoP/(HT600 + Alumina)	853.3	74	852.7	2	856.0	24
NiMoP/(HT600AL + Alumina)	853.4	74	853.0	0	855.6	26
NiMoP/(HT700 + Alumina)	853.4	82	852.7	0	856.0	18
NiMoP/(HT700AL + Alumina)	853.3	79	853.0	1	855.9	20

2.3.8. Hydrocracking activity of NiMoP-supported catalysts

Hydrocracking catalysts were prepared by loading the NiMoP components on the supports based on the modified zeolites and alumina. The catalysts were sulfided and evaluated for their performance in the hydrocracking of a heavy VGO feedstock. As exemplified in literature [14, 16, 66-68], differences in catalytic activity in VGO hydrocracking can be related to the zeolite component as long as the other properties such as the hydrogenation function and catalyst loading are kept similar. The characterization results of the NiMoP-supported catalyst of the present work validate the above assumption since no significant differences among the catalysts in regard to the hydrogenation function were observed.

Hydrocracking activities and the yields to middle distillates and naphtha are presented in **Table 2.8**. For hydrocracking catalysts based on the non-acid-leached zeolites, the conversion of the 370 $°C^+$ VGO fraction decreased with increasing steaming temperature (increasing framework dealumination degree). The selectivity to middle

distillites, when calculated as the yield to middle distillate over yield to naphtha, follows expectedly the reverse trend, namely that it increases with decreasing conversion. The catalysts based on HT500AL and HT600AL display significantly higher VGO hydrocracking activities compared with catalysts based on the corresponding steam-treated zeolites. The catalyst based on the HT700AL zeolite shows different behavior in the sense that the activity decreased upon acid leaching. All of the above observations in the VGO hydrocracking performance can be directly related to changes in the textural and/or acid properties of the zeolite component of the hydrocracking catalysts (**Tables 2.1** and **2.4**).

Table 2.8. Hydrocracking activities of NiMoP-suported catalysts.

Catalyst	Conversion of 370 °C^{+} cut (%)[a]	Yields (wt.%)	
		Middle distillates[b]	Naphtha[c]
NiMoP/(HT500 + Alumina)	32.6	14.5	18.6
NiMoP/(HT600 + Alumina)	27.8	13.4	14.7
NiMoP/(HT700 + Alumina)	19.3	12.2	8.1
NiMoP/(HT500AL + Alumina)	38.5	15.8	22.1
NiMoP/(HT600AL + Alumina)	33.4	16.5	17.4
NiMoP/(HT700AL + Alumina)	12.4	8.1	4.1

[a] Average values after 80 h on stream. No deactivation was observed for the reaction times used to determine conversion.

[b] Yield to middle distillates (180 - 370 °C cut). Based on the liquid fraction of products.

[c] Yield to naphtha (IPB - 180 °C cut). Based on the liquid fraction of products. The gas product yields were less than 5% in all cases.

Overall, the steam treatment of the parent zeolite led to structural collapse of the zeolite due to the extraction of framework Al species. It resulted in a decrease of the total and micropore surface area, the unit cell size and, most importantly, the Brønsted acidity (**Tables 2.1, 2.3** and **2.4**). The degree of dealumination increased with increasing steam-treatment temperature. As a result of the lower acidity, the VGO hydrocracking conversion decreased for zeolites treated at more severe conditions. Upon acid leaching, catalysts made from HT500AL and HT600AL showed improved hydrocracking activity as compared to catalyst prepared from their steam-treated parents zeolites. It is the

consequence of increased accessibility due to partial EFAl removal. The improved conversion of the VGO feed is due to the increased mesopore surface area of the zeolites upon acid leaching. It may be safely assumed that hydrocracking of VGO over USY zeolites is a diffusion-controlled reaction, because the bulky compounds in the feed with up to 40 carbon atoms per molecule cannot enter the micropores. Only a small portion of acid sites can interact with these heavy oil molecules [69]. Therefore, the development of an additional mesopore system during steaming and improvement of its accessibility due to acid leaching by removal of polymerized EFAl species from the mesopores and the pore mouths facilitates the transport of heavy molecules from the bulk to the active sites [16]. The leaching of EFAl species was evident from the combination of chemical analysis, XRD, XPS, and ^{27}Al MAS NMR spectroscopy. The second effect of acid leaching is that the density of Brønsted acid sites increased. This is most likely due to the removal of EFAl species, opening up the pore structure as well as the removal of charge-balancing EFAl cations.

In the present study, it was also found that the relatively mild acid leaching treatment led to some further framework dealumination. This will decrease the Brønsted acid site content. However, its effect on performance is surpassed by the positive effect of the removal of EFAl species. It underlines that straightforward parameters such as the framework Si/Al obtained from NMR or the unit cell size obtained by XRD are not very useful to predict the real feed hydrocracking performance of USY-based hydrocracking catalysts [70]. Specific to the conversion of heavy feeds is that accessibility of the mesopores and availability of acid sites on the external surface of the zeolite crystals are key to good performance.

It was observed that the hydrocracking performance of the acid-leached HT700AL based catalyst was lower than that of the HT700 based one. This is consistent with the observation that acid leaching did not improve the accessibility and acidity of HT700. Moreover, it was seen that significant further framework dealumination occurred after acid leaching of HT700. This is also reflected in the highest Lewis-to-Brønsted acidity ratio of all acid-leached samples (**Table 2.4**). It is likely due to the more extensive agglomeration of the EFAl species upon steam treatment at 700 °C, making the acid leaching treatment ineffective. The decreased performance in VGO hydrocracking can therefore be attributed to the significant decrease in Brønsted acidity.

In accord with literature, it is observed that the middle distillates selectivity, when calculated as the yield to middle distillate over yield to naphtha, decreases with the conversion level [3, 24]. When the NiMoP/(HT600AL + Alumina) and NiMoP/(HT500 + Alumina) catalysts are compared, the former affords more middle distillates at similar conversion. This is probably a consequence of the combination of the lower strong acidity and enhanced mesoporosity induced by hydrothermal and acid treatment steps that prevents overcracking of the intermediate products [3, 14, 16]. This observation shows that, by a proper choice of the steam-calcination and acid-leaching treatment conditions, one can steer the product distribution during VGO hydrocracking using Y zeolites. Of particular importance, the present study shows how mild acid treatments yield to changes in key zeolite properties such as acidity and mesoporosity that are reflected markedly in the hydrocracking performance of a heavy VGO feedstock.

2.4. CONCLUSIONS

USY zeolites with different degree of framework dealumination were obtained by changing the temperature of hydrothermal treatment. Corresponding acid leached zeolites were also prepared. The characterization of the zeolites showed that hydrothermal treatment induces progressive framework dealumination, while acid leaching enhances both the textural and acid properties as a result of EFAl extraction. NiMoP-based hydrocracking catalysts were prepared using the modified zeolites and evaluated in the hydrocracking of a heavy VGO. Hydrocracking activity of the NiMoP supported catalysts correlates directly with the changes in surface area and acidity of the zeolites. Results indicate that a clear association exists between the degree of dealumination and hydrocracking activity for the catalysts based on steam treated zeolites. The lower the framework aluminum content, the lower the hydrocracking catalytic activity. A mild acid leaching treatment to the USY zeolite showed to be beneficial to improve the hydrocracking activity because of the enhanced access to acid sites after the removal of polymerized EFAl species. This study remarks the importance of adjusting the modification conditions to properly tailor the key properties of the USY zeolite such as acidity and surface area when used as the main acidic component of a hydrocracking catalyst.

REFERENCES

[1] J. Scherzer, Hydrocracking Science and Technology, Marcel Dekker, New York, 1995.

[2] A. Hoek, T. Huizinga, A. Esener, I. Maxwell, W. Stork, F. Van de Meerakker, O. Sy, Oil and Gas Journal;(United States) 89 (1991).

[3] P. Dik, O. Klimov, G. Koryakina, K. Leonova, V.Y. Pereyma, S. Budukva, E.Y. Gerasimov, A. Noskov, Catalysis Today 220 (2014) 124-132.

[4] C.S. Triantafillidis, A.G. Vlessidis, N.P. Evmiridis, Ind. Eng. Chem. Res. 39 (2000) 307-319.

[5] R. Beyerlein, C. Choi-Feng, J. Hall, B. Huggins, G. Ray, Topics in Catalysis 4 (1997) 27-42.

[6] S. Li, A. Zheng, Y. Su, H. Zhang, L. Chen, J. Yang, C. Ye, F. Deng, Journal of the American Chemical Society 129 (2007) 11161-11171.

[7] S.M. Almutairi, B. Mezari, G.A. Filonenko, P.C. Magusin, M.S. Rigutto, E.A. Pidko, E.J. Hensen, ChemCatChem 5 (2013) 452-466.

[8] H. Kung, B. Williams, S. Babitz, J. Miller, W. Haag, R. Snurr, Topics in Catalysis 10 (2000) 59-64.

[9] B. Williams, S. Babitz, J. Miller, R. Snurr, H. Kung, Applied Catalysis A: General 177 (1999) 161-175.

[10] N. Malicki, G. Mali, A.-A. Quoineaud, P. Bourges, L.J. Simon, F. Thibault-Starzyk, C. Fernandez, Microporous and Mesoporous Materials 129 (2010) 100-105.

[11] D. Verboekend, G. Vilé, J. Pérez-Ramírez, Advanced Functional Materials 22 (2012) 916-928.

[12] R. Chal, C. Gérardin, M. Bulut, S. van Donk, ChemCatChem 3 (2011) 67-81.

[13] H.K. Beyer, Molecular Sieves,Vol. 3, Springer-Verlag, Berlin, 2002.

[14] X.-w. Chang, L.-f. He, H.-n. Liang, X.-m. Liu, Z.-f. Yan, Catalysis Today 158 (2010) 198-204.

[15] M.-C. Silaghi, C. Chizallet, P. Raybaud, Microporous and Mesoporous Materials 191 (2014) 82-96.

[16] K.P. de Jong, J. Zečević, H. Friedrich, P.E. De Jongh, M. Bulut, S. Van Donk, R. Kenmogne, A. Finiels, V. Hulea, F. Fajula, Angewandte Chemie 122 (2010) 10272-10276.

[17] F.P. Gortsema, R.J. Pellet, A.R. Springer, J.A. Rabo, US 5047139 (1991).

[18] A.V. Abramova, E.V. Slivinskii, Y.Y. Goldfarb, A.A. Panin, E.A. Kulikova, G.A. Kliger, Kinetics and Catalysis 46 (2005) 758–769.

[19] H. Shimada, K. Sato, K. Honna, T. Enomoto, N. Ohshio, Catalysis Today 141 (2009) 43–51.

[20] A. Ishihara, T. Itoh, H. Nasu, T. Hashimoto, T. Doi, Fuel Processing Technology 116 (2013) 222-227.

[21] G. Burnens, C. Bouchy, E. Guillon, J.A. Martens, Journal of Catalysis 282 (2011) 145-154.

[22] R. Galiasso Tailleur, J.R. Nascar, Fuel Processing Technology 89 (2008) 808-818.

[23] E. Benazzi, L. Leite, N. Marchal-George, H. Toulhoat, P. Raybaud, Journal of Catalysis 217 (2003) 376–387.

[24] R. Henry, M. Tayakout-Fayolle, P. Afanasiev, C. Lorentz, G. Lapisardi, G. Pirngruber, Catalysis Today 220 (2014) 159-167.

[25] C. Emeis, Journal of Catalysis 141 (1993) 347-354.

[26] J. Datka, A. Turek, J. Jehng, I. Wachs, Journal of Catalysis 135 (1992) 186-199.

[27] D. Massiot, F. Fayon, M. Capron, I. King, S. Le Calvé, B. Alonso, J.O. Durand, B. Bujoli, Z. Gan, G. Hoatson, Magnetic Resonance in Chemistry 40 (2002) 70-76.

[28] C.A. Fyfe, J.L. Bretherton, L.Y. Lam, Journal of the American Chemical Society 123 (2001) 5285-5291.

[29] P. Grobet, H. Geerts, M. Tielen, J. Martens, P. Jacobs, Studies in Surface Science and Catalysis 46 (1989) 721-734.

[30] X. Zaiku, C. Qingling, Z. Chengfang, B. Jiaqing, C. Yuhua, The Journal of Physical Chemistry B 104 (2000) 2853-2859.

[31] A. Jentys, J. Lercher, Studies in Surface Science and Catalysis 137 (2001) 345-386.

[32] G. Leofanti, G. Tozzola, M. Padovan, G. Petrini, S. Bordiga, A. Zecchina, Catalysis today 34 (1997) 307-327.

[33] J. Weitkamp, M. Hunger, Acid and base catalysis on zeolites, Elsevier: Amsterdam, The Netherlands, 2007, pp. 787-835.

[34] J.W. Niemantsverdriet, Spectroscopy in catalysis, John Wiley & Sons, 2007.

[35] J.H.C. van Hooff, J.W. Roelofsen, in: E.M.F. H. van Bekkum, J.C. Jansen (Eds.), Studies in Surface Science and Catalysis, Elsevier, 1991, pp. 241-283.

[36] J. Ryczkowski, Catalysis Today 68 (2001) 263-381.

[37] A. Gandubert, C. Legens, D. Guillaume, S. Rebours, E. Payen, Oil & Gas Science and Technology-Revue de l'IFP 62 (2007) 79-89.

[38] T. Ninh, L. Massin, D. Laurenti, M. Vrinat, Applied Catalysis A: General 407 (2011) 29-39.

[39] J. Francis, E. Guillon, N. Bats, C. Pichon, A. Corma, L. Simon, Applied Catalysis A: General 409 (2011) 140-147.

[40] C.B.a.L.B. McCusker, Database of Zeolite Structures, The International Zeolite Asociation (IZA), http://www.iza-structure.org/databases/, 2015.

[41] S. Van Donk, A.H. Janssen, J.H. Bitter, K.P. de Jong, Catalysis Reviews 45 (2003) 297-319.

[42] N.P. Rhodes, R. Rudham, Journal of the Chemical Society, Faraday Transactions 89 (1993) 2551-2557.

[43] M.J. Remy, D. Stanica, G. Poncelet, E.J.P. Feijen, P.J. Grobet, J.A. Martens, a.P.A. Jacobs, J. Phys. Chem. 100 (1996) 12440-12447.

[44] Z. Yan, J.Z. Ding Maa, X. Liu, X. Liu, X. Hana, X. Baoa, F. Changb, L. Xub, Z. Liu, Journal of Molecular Catalysis A: Chemical 194 (2003) 153–167.

[45] A. Omegna, J.A. van Bokhoven, R. Prins, The Journal of Physical Chemistry B 107 (2003) 8854-8860.

[46] J. Van Bokhoven, A. Roest, D. Koningsberger, J. Miller, G. Nachtegaal, A. Kentgens, The Journal of Physical Chemistry B 104 (2000) 6743-6754.

[47] S.M.C. Menezes, V.L. Camorim, Y.L. Lam, R.A.S.S. Gil, A. Bailly, J.P. Amoureux, Applied Catalysis A: General 207 (2001) 367–377.

[48] A. Gola, B. Rebours, E. Milazzo, J. Lynch, E. Benazzi, S.L.L. Delevoye, C. Fernandez, Microporous and Mesoporous Materials 40 (2000) 73-83.

[49] A. Corma, V. Fornes, F. Rey, Applied catalysis 59 (1990) 267-274.

[50] N. Salman, C.H. Ruscher, J.-C. Buhl, W. Lutz, H. Toufar, M. Stocker, Microporous and Mesoporous Materials 90 (2006) 339–346.

[51] T. Fleisch, B. Meyers, G. Ray, J. Hall, C. Marshall, Journal of Catalysis 99 (1986) 117-125.

[52] I. Halasz, M. Agarwal, B. Marcus, W.E. Cormier, Microporous and mesoporous materials 84 (2005) 318-331.

[53] N. Malicki, P. Beccat, P. Bourges, C. Fernandez, A.-A. Quoineaud, L.J. Simon, F. Thibault-Starzyk, Studies in Surface Science and Catalysis 170 (2007) 762-770.

[54] S. Khabtou, T. Chevreau, J. Lavalley, Microporous materials 3 (1994) 133-148.

[55] P.O. Fritz, J.H. Lunsford, Journal of Catalysis 118 (1989) 85-98.

[56] O. Cairon, ChemPhysChem 14 (2013) 244-251.

[57] J. Vakros, A. Lycourghiotis, G.A. Voyiatzis, A. Siokou, C. Kordulis, Applied Catalysis B: Environmental 96 (2010) 496-507.

[58] T. Zepeda, B. Pawelec, J. Fierro, A. Olivas, S. Fuentes, T. Halachev, Microporous and Mesoporous Materials 111 (2008) 157-170.

[59] E. Payen, S. Kasztelan, J. Grimblot, J. Bonnelle, Journal of Raman spectroscopy 17 (1986) 233-241.

[60] D. Zingg, L.E. Makovsky, R. Tischer, F.R. Brown, D.M. Hercules, The Journal of Physical Chemistry 84 (1980) 2898-2906.

[61] G. MESTL, T. Srinivasan, Catalysis Reviews 40 (1998) 451-570.

[62] H. Jeziorowski, H. Knoezinger, Journal of Physical Chemistry 83 (1979) 1166-1173.

[63] P. Dufresne, E. Payen, J. Grimblot, J. Bonnelle, The Journal of Physical Chemistry 85 (1981) 2344-2351.

[64] E. Hensen, J. Van Veen, Catalysis today 86 (2003) 87-109.

[65] J. Fierro, J. Conesa, A. Lopez Agudo, Journal of Catalysis 108 (1987) 334-345.

[66] A. Corma, A. Martınez, V. Martınez-Soria, Journal of Catalysis 200 (2001) 259-269.

[67] Q. Cui, Y. Zhou, Q. Wei, X. Tao, G. Yu, Y. Wang, J. Yang, Energy & Fuels 26 (2012) 4664-4670.

[68] K. Sato, Y. Nishimura, K. Honna, N. Matsubayashi, H. Shimada, Journal of Catalysis 200 (2001) 288–297.

[69] J. Arribas, A. Corma, V. Fornes, F. Melo, Journal of Catalysis 108 (1987) 135-142.

[70] R. Bezman, Catalysis Today 13 (1992) 143-156.

3. EFFECT OF EDTA TREATMENT ON THE ACIDIC PROPERTIES OF USY ZEOLITE AND ITS PERFORMANCE IN VACUUM GAS OIL HYDROCRACKING*

SUMMARY

USY zeolite catalysts were chemically modified by treatment with aqueous solutions of sodium ethylenediaminetetraacetic acid (EDTA) to study the effect of removal of extraframework aluminum species (EFAl) on hydrocracking performance. Hydrocracking catalysts were prepared from the modified USY zeolites and alumina loaded with a P-promoted NiMo-sulfide phase. The most active hydrocracking catalyst was obtained by mild EDTA treatment. Under moderate conditions EDTA selectively extracts amorphous EFAl species from the mesopore system, resulting in better access to acid sites and an increase of the concentration of strong Brønsted acid sites. Severe EDTA treatment resulted in lower hydrocracking activity which was ascribed to progressive leaching of EFAl involved in the cracking catalysis. The present study therefore point out the importance of the presence of some EFAl species for the hydrocracking of real feedstocks. This work also shows that even with supports with increased mesoporosity and stronger acid character, higher hydrocracking activity of a real feedstock is not guaranteed.

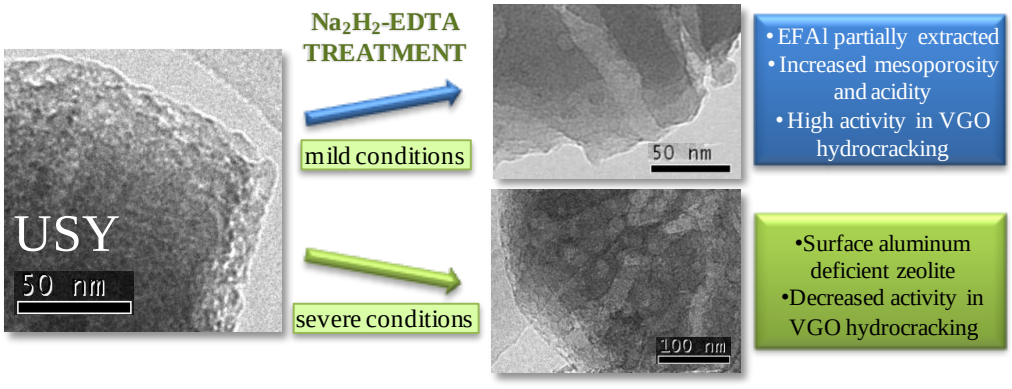

* The content of this chapter was published as*: On the effect of EDTA treatment on the acidic properties of USY zeolite and its performance in vacuum gas oil hydrocracking.* J.L. Agudelo, B. Mezari, E.J.M. Hensen, S.A. Giraldo, L.J. Hoyos. *Applied Catalysis A:* 488 (2014) 219-230.

3.1. INTRODUCTION

Hydrocracking catalysts use USY zeolites that are usually prepared by combination of hydrothermal treatment and chemical modification methods [1, 2]. Hydrothermal treatment results in the formation of extraframework aluminum species (EFAl). These species are usually concentrated near the external surface of the crystals [3]. EFAl is a generic name that involves various Al species, whose proportion and nature depends on the treatment conditions used for dealumination. EFAl species may occur as cationic (Al^{3+}, $Al(OH)_2^{+}$, $Al(OH)^{2+}$) or polymerized forms (AlO(OH), $Al(OH)_3$, Al_2O_3) [4]. It is believed that the cracking activity of USY zeolites is determined by synergistic interactions of framework and cationic extraframework aluminum species [4-6]. The change in the distribution of framework and extraframework Al atoms affects the acid strength of the acid sites of the zeolite. Consequently, differences in the EFAl content can explain the catalytic behavior of hydrocracking catalysts.

The preceding chapter showed that a mild acid leaching treatment to the USY zeolite is favorable to improve the hydrocracking activity because of the partial removal of EFAl species. However, acid leaching also caused framework dealumination and significant changes in the acid and textural properties. This fact leaves open questions in regard of, for example, the role of the quantity extraframework Al species in USY zeolites. The focus of the present chapter is therefore on the role of the EFAl species in the zeolite. USY zeolites with progressive removal of extraframework aluminum species (EFAl) were prepared by treatment of a hydrothermally-treated zeolite with the sodium salt of the ethylenediaminetetraacetic acid (Na_2H_2-EDTA). This compound has shown to be a selective leaching agent for EFAl without removing Al from zeolite framework [7-10]. Hydrocracking catalysts were prepared from the modified USY zeolites and evaluated in the hydrocracking of a VGO feed.

3.2. EXPERIMENTAL

3.2.1. Preparation of zeolites and hydrocracking catalysts

Starting from a NH_4-Y zeolite, a sample named HT600 was obtained by hydrothermal treatment under 100% steam flow for 5 h at 600 °C, following the same procedure described in chapter 2 (section 2.2.1.).

Further chemical treatments with Na_2H_2-EDTA·$2H_2O$ salt aqueous solutions (for simplicity hereinafter referred as EDTA) were performed to the steam-treated zeolite.

Typically, a portion of HT600 was suspended in an EDTA salt solution at a ratio of 20 mL/g of zeolite, at 85 °C for 2 h under stirring followed by filtration and washing with distilled water. Two subsequent ion exchanges were performed in ammonium nitrate solutions at 85 °C for 1 h, followed by filtration, washing, drying at 105 °C for 14-16 h and calcination at 550 °C for 4 h. Three EDTA-modified samples were prepared with gradual increment in strength of treatment by varying the molar concentration of EDTA salt in the solution. EDTA1, EDTA2 and EDTA3 correspond to samples obtained using solutions of 0.09, 0.11 and 0.18 mol/L of EDTA respectively. So, the severity of treatment increases from ETDA1 to EDTA3.

Hydrocracking catalysts were prepared with the hydrothermal treated zeolite and the three EDTA-modified USY zeolites. In first instance, mixed supports were prepared by kneading the modified zeolite (40 wt.%) and alumina binder (Catapal B, kindly supplied by *Sasol North America Inc.*) using a 1 wt.% HNO_3 solution as peptizing agent. The doughs were then extruded in cylindrical shapes. The resulting bodies were dried at 105 °C during 14-16 h, and then crushed and calcined at 550 °C for 6 h under static conditions. Subsequently, phosphorous, molybdenum and nickel were loaded by sequential wet impregnation with intermediate calcinations as described in chapter 2 (section **2.2.1).** The same Ni, Mo and P loadings were intended. The final hydrocracking catalysts were denoted as NiMoP/("modified zeolite" + Alumina).

3.2.2. Characterization methods

3.2.2.1. Textural properties and crystal morphology

Nitrogen adsorption measurements were performed as described in chapter 2.

High Resolution Transmission electron microscopy (HRTEM) pictures of the zeolite particles were taken as detailed in chapter 2.

3.2.2.2. Bulk, surface and framework composition

The bulk chemical composition was measured by ICP-OES in a Spectro Ciros CCD ICP optical emission spectrometer after a digestion stage of each element in a mixture of HF/HNO_3 acids.

The surface composition of the zeolites was determined by XPS using the same experimental conditions described in chapter 2 (section 2.2.3.2.).

XRD patterns of the zeolites were acquired as described in chapter 2. The correlation to estimate the framework Si/Al from the unit cell size (a_0) proposed by Kubelková et al. [10] was used.

$$\alpha = \frac{Al_{framework}}{(Si_{framework} + Al_{framework})} = 0.591\, a_0 - 14.305$$

There are several similar correlations available in the literature [11], however, the above seems to be the most suitable one for the kind of zeolites of the present study (EDTA-treated zeolites). The unit cell composition for FAU structure requires that number of Si and Al atoms must be equal to 192 ($Si_{framework}$+$Al_{framework}$ = *192*). Additionally, all Al atoms must be present in either framework or extraframework phases, therefore, Al_{total} = $Al_{framework}$ + $Al_{extraframework}$. The number of extraframework Al per unit cell was calculated as detailed in reference [12] using the framework Si/Al taken from the ^{29}Si MAS NMR data.

Crystallinity degree was estimated following the TOPAS 4.2 tutorial. In first instance, the calculation implies modeling the amorphous phase bump by inserting a split pseudo-Voigh (SPV) peak at the peak maximum. In the next step, the peaks coming from the crystalline phase are modeled and refined. In that way, the software is able to calculate the composition of both phases and to quantify the crystallinity degree.

3.2.2.3. Acid properties

Acidity distribution of the modified-USY zeolites was monitored by temperature programmed desorption (TPD) of ammonia in a Micromeritics TPD/TPR 2900 instrument with a thermal conductivity detector (TCD). Typically, 0.3 g of zeolite sample was placed in a quartz reactor and was heated up to 550 °C with a temperature ramp of 10 °C/min under He flow (50 mL/min); at this temperature the samples was further heated for 1 h. Adsorption of ammonia took place after cooling to 150 °C by pulses until full saturation was verified. Physically adsorbed ammonia was removed by flushing the sample with He flow for 1 h. Desorption of ammonia was performed at a rate of 10 °C/min from 150 °C to 550 °C under He flow (50 mL/min), followed by an isothermal step of 1 h.

The Brønsted and Lewis acidity of the modified zeolites was analyzed by adsorption/desorption of pyridine monitored by FTIR spectroscopy. The experimental method was the same as detailed in chapter 2.

3.2.2.4. Nuclear Magnetic Resonance

The ^{27}Al Magic Angle Spinning (MAS) Nuclear Magnetic Resonance (NMR) spectra of the zeolite samples were recorded at a magnetic field of 11.7 T as reported in chapter 2.

^{27}Al MQ MAS NMR spectra were recorded by use of a pulse sequence p1-t1-p2-τ -p3-t2 for triple quantum generation and zero-quantum filtering (strong pulses p1 = 3.4 μs and p2 = 1.4 μs at ν1 = 100 kHz; soft pulse p3 = 11 μs at ν1 = 8 kHz; filter time τ =20 μs; interscan delay 0.2 s).

The isotropic chemical shift of ^{27}Al atoms in solids depends on their coordination number (three-, four-, five- or six-fold coordinated to oxygen atoms). Also the species of atoms in the next coordination sphere and the bonding angle via oxygen atoms between linked tetrahedra influence the chemical shift. Therefore the ^{27}Al MAS NMR spectrum provides information about the coordination of the aluminum species. However, the spectra resolution is reduced by the second-order quadrupolar interaction of the central transition, which shifts the position of the central transition resonance away from its isotropic (actual) chemical shift and gives broad powder patterns. Operating under MAS condition reduces, but does not completely average the second-order quadrupolar interactions. With the ^{27}Al MQ MAS NMR experiment, a correlation between the multiple and single quantum transitions is made, which leads to well-resolved spectra that have an isotropic dimension, free of any anisotropic quadrupolar broadening. This permits an unambiguous determination of the aluminum coordinations in the sample. The values of the isotropic chemical shifts and quadrupolar parameters determined from the analysis of the MQ MAS NMR spectra can be used to simulate the ^{27}Al MAS NMR spectra, leading to quantitative information on the aluminum species. In the present study, the fitting of the experimentally obtained ^{27}Al MAS NMR spectra was performed with the Dmfit2011 program employing Czjzek lineshape peaks. The Czjzek lineshapes assume a Gaussian distribution of chemical shifts and quadrupolar coupling constants [13].

The ^{29}Si MAS spectra were recorded at 9.4 T as detailed in chapter 2. The quantitative analysis was also performed in the same way as for zeolites of chapter 2.

With the aim of providing a coherent understanding of the results described in this chapter, **Appendix A** further describes the characterization techniques that were used to assess the properties of the modified zeolite and the hydrocracking catalysts.

3.2.3. Activity evaluation

3.2.3.1. Zeolite acid activity tests

The acid activity of the modified zeolites was determined by measuring the rate of monomolecular conversion of propane [14]. Briefly, a tubular flow reactor was loaded with 0.1 g of 60/80 mesh zeolite pellets, which were mixed with 0.9 g of SiC. Catalytic activity measurements were performed at 590 °C with a feed mixture of 10 vol% C_3H_8 in He that was delivered by mass flow controllers at a total flow rate of 100 mL/min. The product composition was analyzed by an online three-column gas chromatograph. The conversion was kept below 2% to ensure differential conditions. The reaction rate (r) was calculated according to $r = X \cdot F / m_{cat}$, in which X is the conversion of propane, F is the flow rate in mol/s and m_{cat} is the mass of the catalyst in g. The rate of cracking (methane and ethylene as the main products) and dehydrogenation (propylene and hydrogen as the main products) were computed according to the products distribution.

3.2.3.2. Cracking activity of the extruded supports

The activity of the extruded supports (modified zeolite and alumina, previous to the incorporation of metals), were tested in the cracking of 1,3,5-tri-isopropylbenzene (1,3,5-TIPB) at 350 °C at atmospheric pressure in a fixed-bed micro-activity test (MAT) unit. Typically, the reactor was loaded with 1 g of the catalyst particles (30/50 mesh size) mixed with 2 g of inert sand (60/70 mesh size). The samples were heated to 350 °C under a 30 mL/min flow of dry nitrogen for 1 h. Then 1 mL of 1,3,5-TIPB (96 wt.%, Merck) was injected by a syringe pump during 38 s. Liquid products were condensed and analyzed by gas chromatography. The 1,3,5-TIPB molecule has a kinetic diameter of ~ 0.94 nm that is significantly larger than the Y-zeolite openings of ca. 0.74 nm. Therefore the conversion of this molecule corresponds to the relative amount of strong acid sites on the mesopores and the external surface of the zeolites particles [15]. The conversion of 1,3,5-TIPB has been used as a test reaction either to depict the behavior of heavy hydrocarbons feedstock or to inspect the diffusion properties of the Y zeolite in FCC catalysts [16-20].

3.2.3.3. Activity evaluation of hydrocracking catalysts

Hydrocracking activity tests were performed with the NiMoP-supported catalysts using the same feedstock and sulfidation procedure described in chapter 2. Experimental conditions used for the reaction tests of the present chapter were 350 °C, 1500 psig, and 1250 NL/L of H_2/feed volume ratio. The weight hourly space velocity during the first 18 h on stream was 2 h^{-1}, and for the rest of the run it was 1 h^{-1}. The duration of every run was at least 100 h. Conversion and yields were calculated as in chapter 2. Products were analyzed as detailed in chapter 2.

3.3. RESULTS AND DISCUSSION

3.3.1. XRD patterns

Figure 3.1 presents the X-ray diffraction patterns of the modified zeolites. Both the number of peaks and peak positions agree well with the powder diffraction pattern of a typical Ultrastable Y zeolite (FAU framework type) reported by The International Zeolite Association (IZA) [21]. EDTA treatments preserve the structural character of the zeolite since the whole patterns are identical. Higher peak intensities for EDTA-treated samples are observed suggesting higher crystallinity degree.

Figure 3.1. XRD patterns of the modified zeolite samples.

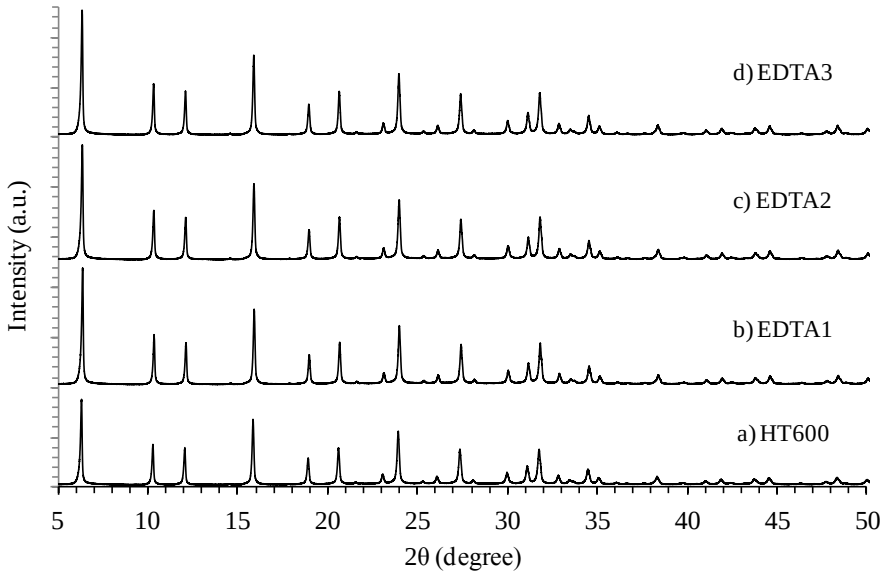

3.3.2. Textural characterization of the modified zeolites

In **Figure 3.2** the nitrogen adsorption and desorption isotherms are given for the different USY zeolites. The samples present type IV isotherms with hysteresis loops indicative of materials possessing both micro and mesoporosity. For HT600 the hysteresis loop is slightly flat, indicating inkbottle type pores, whereas the progressive change to upward curvature in the hysteresis loop of the EDTA-treated samples is indicative of development of cylindrical type of pores [22].

Figure 3.2. Nitrogen adsorption and desorption isotherms for the zeolites. For clarity the isotherms have been shifted upward. For better visualization, curves were vertically shifted according to the following values: a) no shift, b) no shift, c) 2 mmol/g, d) 3 mmol/g.

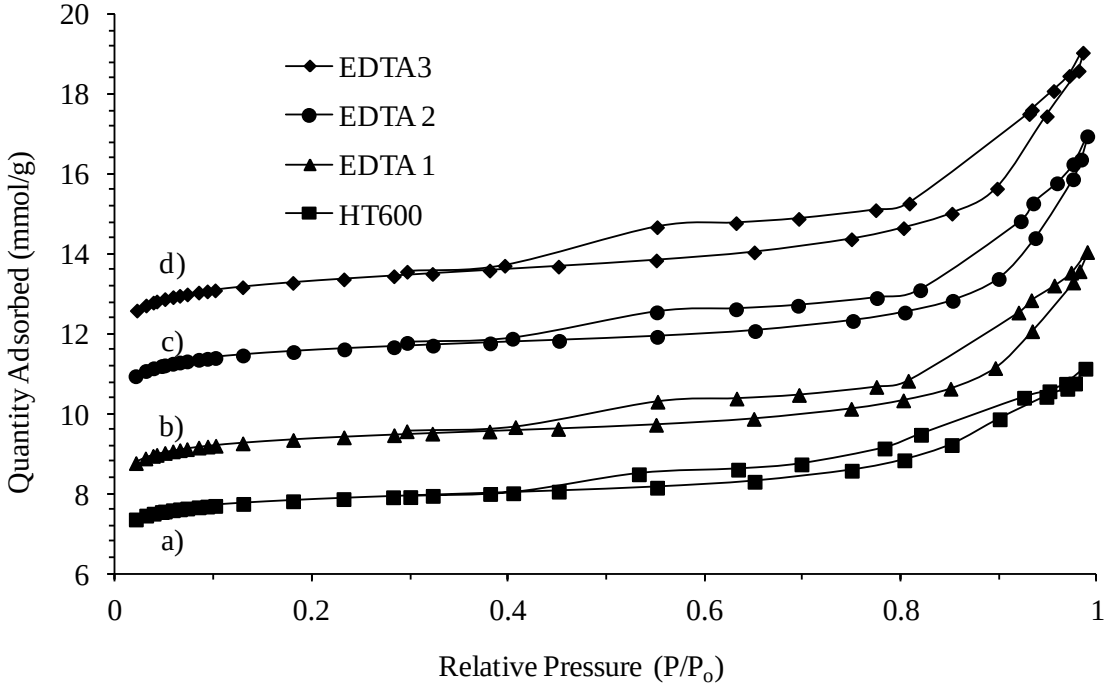

The pore size distributions of the zeolite samples are presented in **Figure 3.3**. The materials of the present study have a relatively wide mesopore size distribution with a maximum around 16 nm in the case of HT600, which is shifted to around 24 nm for the EDTA-treated samples. It is known that during steaming Al ions are extracted from the framework leaving lattice vacancies [3, 23]. Some of the vacancies are healed by mobile silicon species, resulting in the formation of a secondary pore system [1]. It has been

postulated that the collapse of the zeolite framework occurs by disassembly of the sodalite cages (β-cages) that destroys some supercages and the associated 12-membered rings, leading to the formation of mesoporosity in the range of 5-50 nm [3].

Figure 3.3. Pore size distributions of the modified zeolites calculated from the nitrogen adsorption isotherms (BJH method).

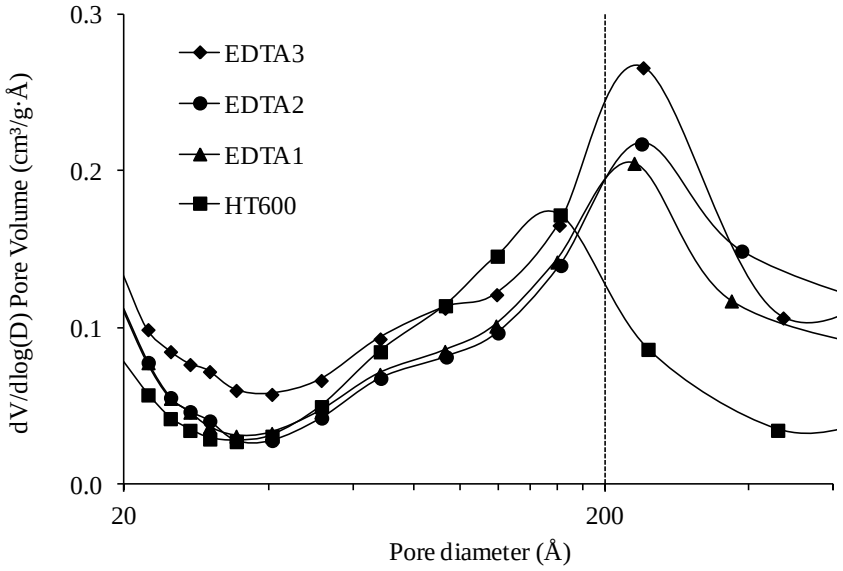

Table 3.1 presents the main textural characteristics of the zeolites used in this study. In first instance, comparing the HT600 sample with the starting H(Na)-Y zeolite (CBV400), it is observed that the hydrothermal treatment causes a decrease in total and microporous surface area and in the microporous volume. At the same time, there is a small increase in the total and mesoporous volume. These changes in textural properties after steam treatment have been attributed to the partial collapse of the zeolite structure [3]. Now, comparing the EDTA-modified zeolites with the hydrothermally treated zeolite (HT600), it is clear that all the textural properties significantly improve after EDTA treatment. The changes in the properties are more substantial when the severity of treatment is increased, that is going from sample EDTA1 to EDTA3. These results are line with those reported by Rhodes et al. [9], where the increase in micro- and mesoporosity due to EDTA treatment was ascribed to the removal of EFAl species formed during the hydrothermal treatment that block the pore system. Similar changes

in the textural properties of Y zeolites after chemical modification with methods such as acid and alkaline treatment have been also observed [24].

Table 3.1. Textural properties of the modified zeolites.

Zeolite	S_{BET} (m^2/g)[a]	S_{micro} (m^2/g)[b]	S_{meso} (m^2/g)[c]	V_{total} (cm^3/g)[d]	V_{micro} (cm^3/g)[e]	V_{meso} (cm^3/g)[f]
CBV400	739	679	60	0.35	0.28	0.07
HT600	686	624	62	0.39	0.26	0.13
EDTA1	781	701	80	0.49	0.29	0.20
EDTA2	798	717	82	0.52	0.30	0.22
EDTA3	858	753	105	0.56	0.31	0.25

[a] BET specific surface area. [b] t-plot micropore area. [c] t-plot external surface area.

[d] Total pore volume. [e] t-plot micropore volume. [f] Mesopore volume = $V_{total} - V_{micro}$.

3.3.3. Morphological characterization

Figure 3.4 shows representative transmission electron micrographs of all the zeolites. The images clearly show the features of the mesopore system. The smooth dark zones relate to the unaffected microporous regions of the crystals, whereas the light gray areas represent the mesopores. Globally, the distribution of mesopores is not homogeneous among different zeolite grains and within individual grains. Some small cavities with diameters of less than 10 nm are apparent in all samples. Predominantly for EDTA-treated zeolites, cavity-like mesopores appear to combine to form channels in some regions. For EDTA3, those channels-like mesopores are apparently connected to the external surface having diameters of 20-25 nm. Similar observations in regard to the characteristics of mesopores in USY zeolites have been reported for chemically treated USY zeolites [3, 25].

In summary, EDTA treatment leads to materials with enhanced textural properties. Micro- and mesoporosity were significantly increased by this treatment. HRTEM images support the statement that mesoporosity is enhanced.

Figure 3.4. High resolution TEM images of the modified zeolites. Arrows point to channels-like mesopores clearly visible for EDTA-treated samples.

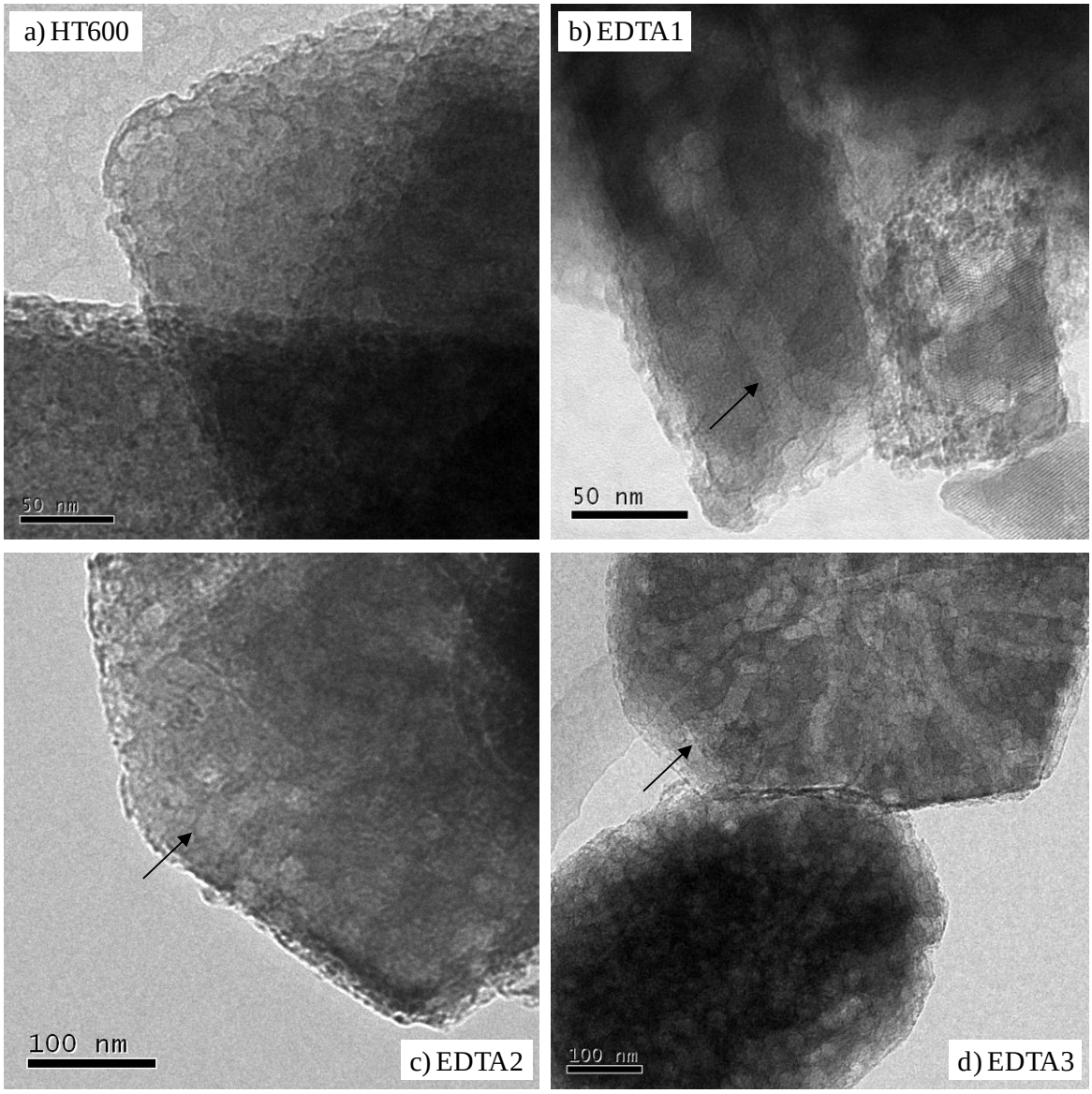

3.3.4. ^{29}Si MAS NMR characterization

The experimentally obtained and deconvoluted ^{29}Si MAS NMR spectra of the samples are shown in **Figure 3.5**. In all of the modified-zeolites, silicon species with 0Al neighbors dominate the spectra. At a first glance, EDTA treatment does not induce severe changes in the silicon species distribution.

The relative intensities of the peaks associated to each Q^4(nAl) environment are presented in **Table 3.2**. The increase of relative intensities of Si(2Al) and Si(1Al) species, and the decrease of Si_{EF} species after performing the EDTA treatment to the

HT600 zeolite at low concentration (sample EDTA1), suggest that this agent is able to reinsert to the framework some extraframework species. No significant changes in the Si species distribution are observed after performing the treatment at higher EDTA concentration. Furthermore, EDTA does not induce further framework dealumination.

Figure 3.5. ^{29}Si MAS NMR spectra of the steamed and chemically modified Y zeolites. In each spectrum the solid line (up) represents the experimental curve and the dashed line corresponds to the computed model. Solid lines (down) correspond to the Gaussian peaks representing each Q^4(nAl) species.

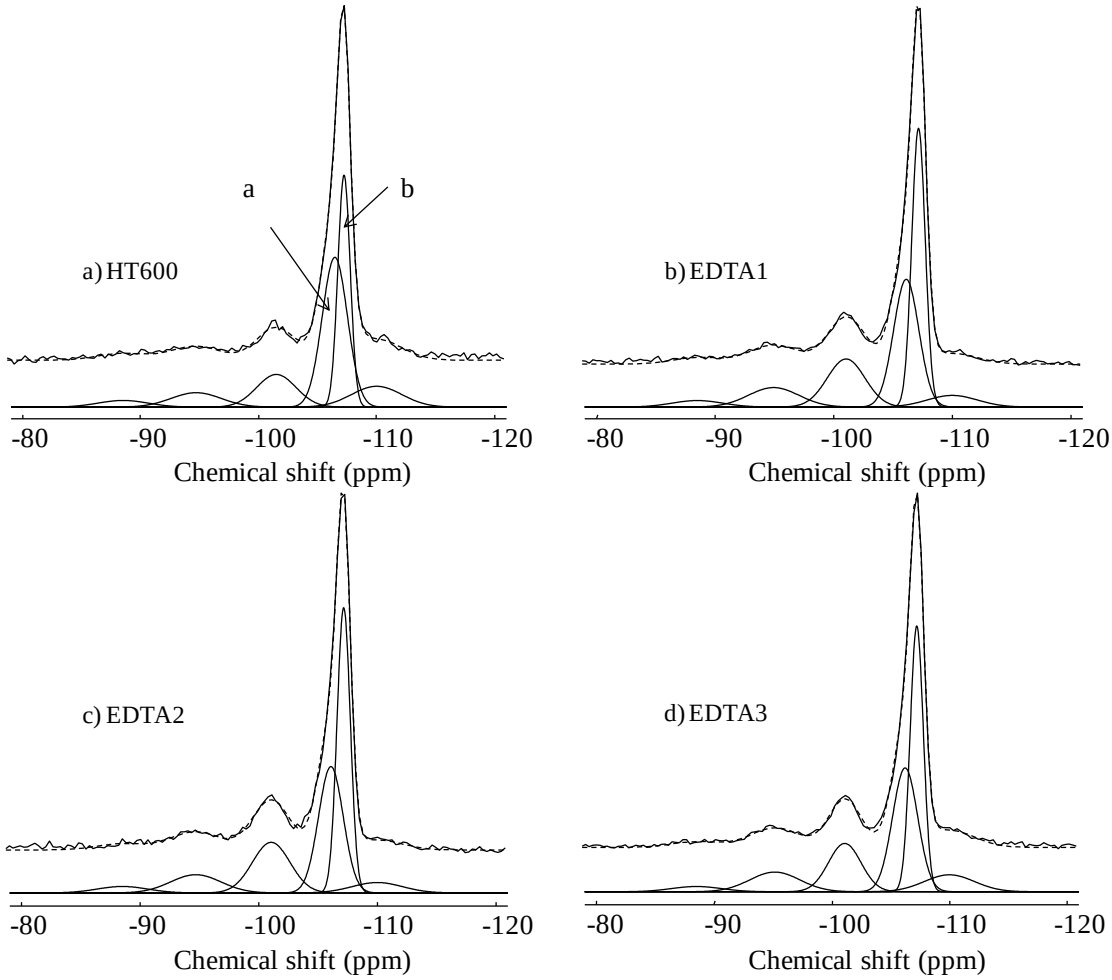

Table 3.2. Relative intensities of the deconvoluted signals from the ^{29}Si MAS NMR spectra.

Signal		HT600	EDTA1	EDTA2	EDTA3
Si(3Al)	δ (ppm)	-88.5	-88.5	-88.5	-88.5
	$I_{Si(3Al)}$ (%)	3.4	3.1	2.9	2.7
Si(2Al)	δ (ppm)	-94.7	-94.9	-94.7	-95.2
	$I_{Si(2Al)}$ (%)	7.0	9.1	8.7	9.5
Si(1Al)	δ (ppm)	-101.5	-101.04	-101.05	-101.1
	$I_{Si(1Al)}$ (%)	12.9	16.8	17.9	15.2
$Si(0Al)_a$	δ (ppm)	-106.5	-106.1	-106.1	-106.2
	$I_{Si(0Al)}$ (%)	37.8	30.4	29.6	30.3
$Si(0Al)_b$	δ (ppm)	-107.2	-107.2	-107.2	-107.2
	$I_{Si(0Al)}$ (%)	28.5	35.5	36.1	34.0
Si_{EF}	δ (ppm)	-110.0	-110.0	-110.0	-110.0
	$I_{Si(EF)}$ (%)	10.5	5.1	4.7	8.3

3.3.5. Compilation of the main physicochemical properties of the modified zeolites

Table 3.3 summarizes the Si/Al ratios of the parent and modified zeolites calculated from ICP-OES, XPS, XRD and ^{29}Si MAS NMR. XRD data indicated similar values of unit cell size for all the zeolites. This indicates that EDTA treatment had little effect on the framework Si/Al ratio. XRD patterns of the treated zeolites (not shown) also show that the EDTA treatment did not affect the crystal structure of the zeolite. However, EDTA significantly increases the crystallinity, which is a consequence of the extraction of amorphous materials formed during the hydrothermal treatment [24].

The lattice Si/Al ratios determined from ^{29}Si MAS NMR are similar to the ones obtained by XRD for the EDTA-treated samples. There is only a difference in the values for the hydrothermally treated zeolite (HT600). The decrease in framework Si/Al ratio in EDTA-treated zeolites with respect to the hydrothermally treated zeolite indicated by ^{29}Si MAS NMR suggest that EDTA treatment results in the reinsertion of some extraframework Al atoms into the lattice or in the extraction of some framework silicon atoms. Both behaviors have been described for alkaline-treated Y zeolites [26, 27]. As ^{29}Si MAS NMR shows that the framework Si/Al ratio hardly changed, reinsertion of EFAl species or extraction of Si species by EDTA treatment seems unlikely.

Table 3.3. Structural properties of the modified zeolites.

Zeolite	ICP-OES	XPS	XRD				^{29}Si MAS NMR			
	Si/Al	Si/Al	$a_{o,}$ (Å)	$(Si/Al)_F$[a]	NAl_F[b]	Cryst.[c], (%)	$(Si/Al)_F$[d]	NAl_F[b]	Si_{EF}[e], (%)	NAl_{EF}[f]
HT600	3.1	1.3	24.384	8.4	20.3	73	9.7	18.0	10.5	38
EDTA1	5.6	5.8	24.384	8.4	20.3	90	8.6	20.1	5.1	11
EDTA2	6.3	7.2	24.377	8.8	19.5	93	8.7	19.9	4.7	7
EDTA3	7.0	7.8	24.385	8.4	20.5	87	8.7	19.9	8.3	5

[a] From Kubelková et al. equation (see experimental section).

[b] Number of aluminum atoms in the framework per unit cell. Assuming perfect cell, so $NAl_F + NSi = 192$.

[c] Calculated according to TOPAS software tutorial.

[d] Calculated from ^{29}Si MAS NMR data.

[e] Relative amount of extraframework silica, from peak at -110 ppm in ^{29}Si MAS NMR spectra.

[f] Number of extraframework aluminum per unit cell.

Elemental analysis by ICP-OES indicated that the bulk Si/Al ratios increase after increasing severity of the treatment with EDTA. This is an indication of progressive dealumination of the zeolites. The considerable difference between the bulk and framework Si/Al ratios (from XRD and ^{29}Si MAS NMR) evidences the presence of a significant amount of EFAl species in HT600 zeolite. This difference decreases after EDTA treatment. As the framework Si/Al ratios were hardly affected by EDTA treatment, these data confirm that EDTA preferentially extracts extraframework aluminum. This is consistent with previous works from literature [8-10].

According to XPS, in sample HT600 the Si/Al ratio at the external surface of the crystals is significantly lower than the one of the bulk. This means that external surface of the zeolite crystals of this sample is enriched in Al. This has been explained by the migration of part of the Al atoms expelled during the steaming procedure toward the external surface of the crystals [3, 23, 28]. On the other hand, for the EDTA-treated samples the surface Si/Al ratio becomes higher than that of the bulk. This indicates that these samples are depleted in surface Al. This decrease in the surface Al content of steamed zeolites after chemical treatments such acid leaching has been reported and is generally explained by the dissolution of extraframework Al [28]. Therefore, since the framework is not dealuminated with our EDTA treatment, it can be deduced that the external surface of the zeolite crystals is depleted in extraframework Al. Additionaly, it

can be reasonably inferred that also the treatment depletes the EFAl content at the walls of the mesopores. This can be done taking into account the presence of wide mesopores apparently connected to the external surface evidenced for the EDTA-treated zeolites that would facilitate the access to EDTA. In particular, according to Dwyer et al. [29] dealumination with EDTA proceeds from the outside of the crystal surface, probably due to diffusional limitations. Therefore, an aluminum composition gradient along the zeolite crystals is expected after treatment with EDTA [29, 30].

Summing up, the results presented above indicate that the framework is not significantly affected by EDTA treatment. The main effect of EDTA treatment is the progressive decrease of the content of EFAl species.

3.3.6. Al speciation by ^{27}Al MQ MAS NMR

Figure 3.6 shows the ^{27}Al MQ MAS NMR spectra of zeolites measured at a field of 11.7 T. The F2 projection of the 2D MQ MAS spectra is the anisotropic (MAS) dimension. The F1 projection is the isotropic multiple-quantum dimension free of any anisotropic quadrupolar broadening. The upper lines in each spectrum are the corresponding 1D ^{27}Al MAS NMR spectra. The MAS spectra (F2 projections) are distorted compared to those obtained from the single-pulse MAS experiments (1D) because of the non-uniform excitation conditions.

For HT600 sample (**Figure 3.6a**), at least two different contributions are distinguished in the MQMAS spectra in the tetrahedral region (from 65 to 35 ppm) denoted $Al(IV)_a$ and $Al(IV)_b$. In the octahedral region (from 20 to -20 ppm) three overlapping resonances can be distinguished, namely $Al(VI)_a$, $Al(VI)_b$, and $Al(VI)_c$. A signal of low intensity slightly deviated from the diagonal at 35 to 40 ppm attributed to five-coordinated Al and called Al(V), is also detected. In the ^{27}Al MQ MAS NMR spectrum of EDTA-treated samples (Figure 8 b, c and d) the intensity of the species Al(V), $Al(VI)_a$, $Al(VI)_b$ and $Al(VI)_c$ gradually decrease with the severity of treatment. Al(V) almost completely disappeared from the 2D spectrum in sample EDTA3. Compared with previous reports, the present ^{27}Al MQ MAS results on the steam-treated zeolite (HT600) are in general agreement with the findings of Omegna et al. [31].

Figure 3.6. ^{27}Al MQ MAS NMR 2D contour plots of the steam and EDTA-treated zeolites measured at 11.7 T. F2 and F1 projections of the 2D MQMAS spectra are the anisotropic (MAS) and the isotropic multiple-quantum dimensions, respectively. The upper lines in each spectrum are the corresponding 1D ^{27}Al MAS NMR spectra. The different aluminum species detected in the samples are indicated in a).

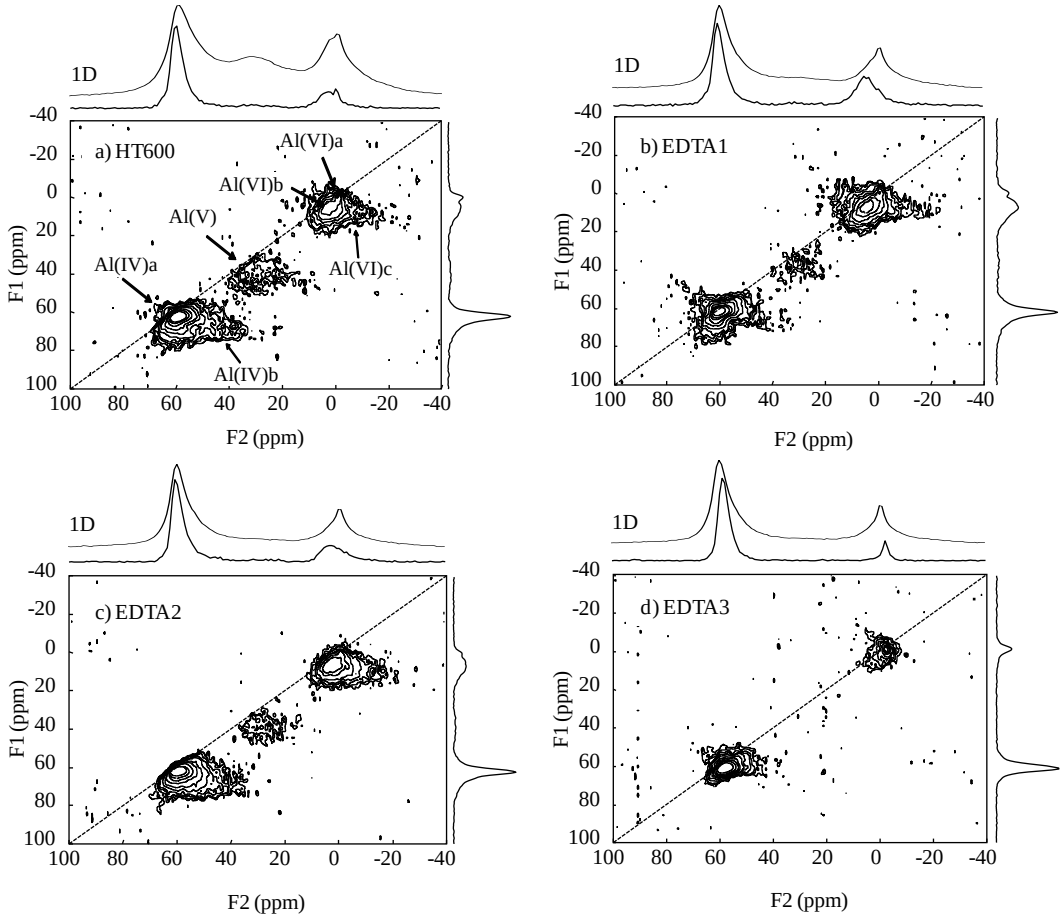

The peak Al(IV)$_a$ resonates close to the diagonal, indicating that the corresponding Al species experience a small quadrupolar interaction. Al(IV)$_a$ resonance is assigned to tetra-coordinated framework Al atoms charge-balanced by protons and with weak electric field gradients (EFGs) at the nucleus. Peak Al(IV)$_b$, which appears as a tail to signal Al(IV)$_a$, deviates from the diagonal, indicating a large anisotropic quadrupolar-induced shift or in other words, much stronger EFG at the nucleus and thus a less symmetrical electronic surrounding. The species Al(IV)$_b$ has been object of intense debate in literature. This broad component has been assigned to non-framework tetrahedral Al from amorphous silica-alumina, to penta-coordinated Al species, and to

strongly distorted tetrahedral framework aluminum [32, 33]. Ray et al. [34] stated that after the initial stages of dealumination the aluminum extracted from the framework remains tetrahedral instead of forming octahedral species. This non-framework four coordinated Al species probably resides trapped in the centre of the basic sodalite units resistant to any further migration. Most recently, Malicki et al. [6] have shown results that support the attribution of $Al(IV)_b$ as a framework tetra-coordinated Al interacting with cationic EFAl species.

The $Al(VI)_a$ species resonates close to the diagonal and corresponds to a narrow peak. It has been previously suggested that the highly symmetric environment around the nuclei indicates that the $Al(VI)_a$ resonance corresponds to cationic extra-framework aluminum species in close vicinity to the framework [6]. The Al species attributed to $Al(VI)_b$ experience a relatively small quadrupolar interaction but higher chemical heterogeneity than species $Al(VI)_a$ since their resonance lineshapes are more elongated in the 2D spectrum diagonal. $Al(VI)_c$ shows strong quadrupolar broadening.

The Al(V) signal is traditionally attributed to penta-coordinated Al. Conversely, Menezes et al. [35] have assigned the peak at around 32 ppm to amorphous silica-alumina species with tetrahedral coordination formed during steam dealumination. According to Gola et al. [7] the Al(V) signal detected by NMR in a steamed sample and removed by EDTA leaching is associated with amorphous alumina, which may also contain Al(IV) and Al(VI). In the present study, this kind of polymerized EFAl is extracted progressively with increasing concentration of EDTA. Such attribution of the Al(V) signal to amorphous alumina would support the observations in respect to the changes in textural properties after EDTA treatment due to the extraction of EFAl species.

3.3.7. Quantification of Al species with ^{27}Al MAS NMR

The information obtained from the MQ MAS experiments is then used to simulate the 1D ^{27}Al MAS spectra. **Figure 3.7** shows the ^{27}Al MAS NMR spectra of the samples and their decomposition in six signals. The fitting model accurately simulates the experimental MAS spectra and is consistent with most of the findings obtained from the MQ MAS experiment. The main observations derived from visual inspection of **Figure**

3.7 are the progressive sharpening of the signal $Al(IV)_a$ and the depletion of signals Al(V) and $Al(VI)_b$ with increasing severity of EDTA treatment.

Figure 3.7. ^{27}Al MAS NMR spectra of the samples and their decomposition into Czjzek lineshapes peaks measured at 11.7 T. The fitted curves are presented as solid lines below the experimental spectra (upper lines).

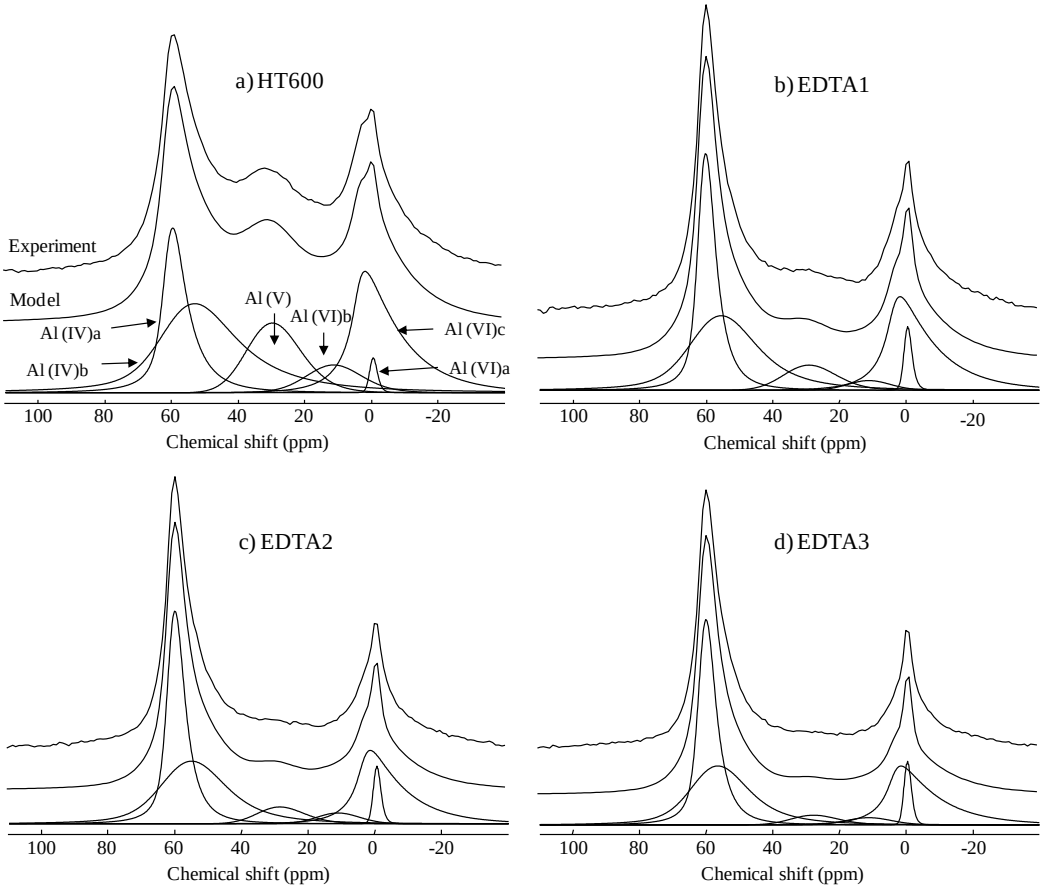

Table 3.4 presents the set of NMR parameters obtained from the fit of all ^{27}Al MAS NMR spectra and the relative contribution of the different Al species in the samples. Quadrupolar Coupling Constant (CQ) and isotropic chemical shift (δ_{iso}) values for the different species compare well with those previously reported in literature [31]. The values of the relative contribution of the different Al species clearly confirm that EDTA treatment progressively increases the population of the tetra-coordinated framework aluminum species $Al(IV)_a$, and depletes the amount of penta-coordinated Al, Al(V). Changes in Al coordination have been reported for USY zeolites after different post-

synthesis treatments [32]. In particular, it has been claimed that EDTA treatment in USY converts Al(V) and Al(VI) species into $Al(IV)_b$ species [33].

Table 3.4. NMR parameters obtained from the fit of the ^{27}Al MAS NMR spectra and the relative contribution of the different Al species in the samples.

Species	Parameter	HT600	EDTA1	EDTA2	EDTA3
	δ_{iso} (ppm)	61	61	61	61
$Al(IV)_a$	CQ (MHz)	3.0	2.4	2.4	2.4
	%	20	29	32	35
	δ_{iso} (ppm)	59	60	59	60
$Al(IV)_b$	CQ (MHz)	5.1	4.1	3.9	3.7
	%	32	31	32	31
	δ_{iso} (ppm)	35	34	33	32
Al (V)	CQ (MHz)	3.9	3.6	3.6	3.5
	%	15	8	6	4
	δ_{iso} (ppm)	13	13	13	13
$Al(VI)_b$	CQ (MHz)	2.2	2.2	2.2	2.2
	%	6	2	3	2
	δ_{iso} (ppm)	4	4	4	4
$Al(VI)_c$	CQ (MHz)	4.5	4.4	4.3	4.5
	%	25	26	25	24
	δ_{iso} (ppm)	0	0	0	0
$Al(VI)_a$	CQ (MHz)	1.3	1.3	1.3	1.2
	%	1	3	3	4

Contrasting to data in **Table 3.3**, ^{27}Al MAS NMR results indicate only partial removal of hexa-coordinated aluminum after EDTA treatment. Due to either their nature or their location inside the small cages which make them inaccessible to the reactant molecule because of diffusion limitations, some EFAl species are more difficult to remove from the zeolites [9]. Nevertheless, some other studies have shown complete disappearance of the NMR signal corresponding to the penta- and hexa-coordinated aluminum after EDTA treatment [7, 33], suggesting in that way that most of the EFAl were extracted. The discrepancy between the results of the present study and those from the literature in regard to the extent of EFAl extraction is most probably related to differences in the severity of treatment conditions. For instance, Katada et al. [33] used higher temperature and longer contact time compared to the present study. Interestingly,

Rhodes et al. [9] observed that, after EDTA extraction for samples with virtually no peaks arising from non-framework Al, the octahedral peaks become visible upon the addition of acetyl-acetone. This complexing agent facilitated the resolution of the highly asymmetric (invisible) non-framework aluminum. Apparently, the majority of the non-framework aluminum in steamed samples is present as highly asymmetric species such as $Al(OH)_2^+$, $Al(OH)^{2+}$ and polymeric oxides [9]. The invisibility of some EFAl species would partially explain the observed discrepancy in the extent of removal of extra-framework Al derived from the difference between the global and the framework Si/Al ratios.

3.3.8. Acidic properties of the modified zeolites

3.3.8.1. Hydroxyl group speciation

The acidic properties of zeolites are mainly connected to the structural hydroxyl groups. Infrared spectra in the region of the OH vibrations for the zeolite samples are shown in **Figure 3.8**. The spectra show at least seven distinguishable bands at 3566, 3600, 3631, 3670, 3700, 3739 and 3745 cm^{-1}. The most notorious change observed after EDTA treatment is the depletion of the intensity of the band at 3566 cm^{-1} with respect to the band at 3631 cm^{-1}. In addition, the intensity of the bands at 3739 and 3745 cm^{-1} progressively increase with respect to the other bands of the spectra.

The bands at around 3631 cm^{-1} (high-frequency band, HF) and at around 3566 cm^{-1} (low frequency band, LF) correspond to Brønsted acid groups having a siliceous environment (Si-OH-Al) located in the supercages and in the hexagonal prism and/or sodalite cages, respectively [36, 37].

The assignment of the band at around 3600 cm^{-1} is controversial. It has been attributed to species such as non-acidic lattice hydroxyls, inaccessible OH groups, non-framework Al(OH) species and strongly acidic amorphous silica–alumina [35, 38-40]. Also Niwa et al. [41] identified a hydroxyl group absorbing at 3595 cm^{-1} after performing treatment with Na_2H_2-EDTA to a USY zeolite. Although the position of the band is slightly different, the OH group they detected seems to be the same as the one observed in the present study. In recent literature this band is referred as “perturbed” or “polarized” HF band and ascribed to framework hydroxyl groups of enhanced acidity due to close proximity of non-framework cationic Al species [42, 43]. Cationic EFAl such as

$Al(OH)^{2+}$, or $Al(OH)_3$ clusters, were suggested to withdraw electron density of the framework close to the Brønsted acid site, enhancing its acid strength [41]. It has been argued that the interaction of EFAl species with the HF OH groups results in superacidity and enhanced catalytic activity [44]. However, also zeolites that do not demonstrate high catalytic activity (after sodium exchange, for example) still show quite an intense band around 3600 cm^{-1}. Consequently, some non-acidic species may also contribute to this mode [42, 45]. According to Malicki et al. [39] the region between 3650 and 3575 cm^{-1} contains five peaks ascribed to OH groups in the supercage, the exact position depending on the nature and location of the EFAl phase. The possible presence of these superimposed vibrations makes difficult the interpretation of the changes in this region of the FTIR spectra.

Figure 3.8. FTIR spectra in the OH region for the zeolite samples. Positions for the main bands are indicated. Spectra were taken at 30 °C after following the same sample preparation and pretreatment procedure used for the pyridine measurements.

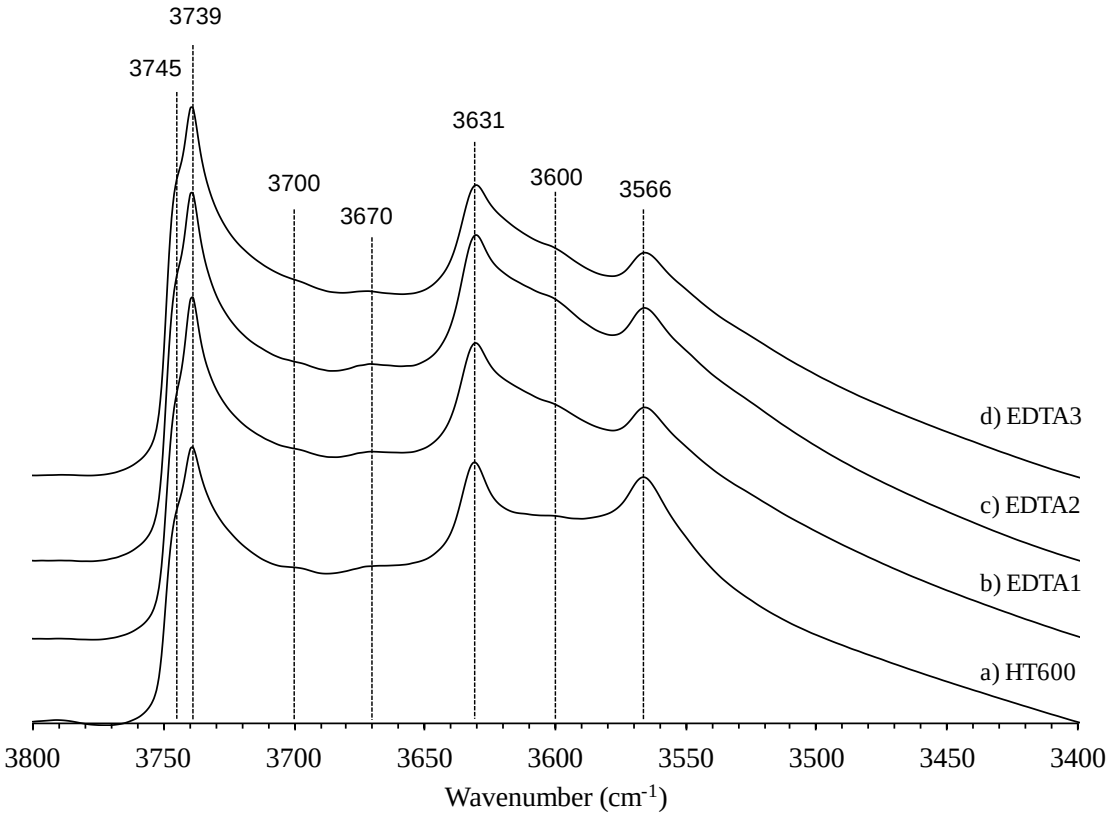

The weak bands at 3670 and 3700 cm^{-1} are assigned to hydroxyl groups of Al-OH species present in extraframework material [46, 47]. The asymmetric band between 3700 and 3760 cm^{-1} corresponds to the superposition of different kinds of silanol groups [37, 48]. The sharp band situated at around 3739 cm^{-1} is due to terminal silanol consisting of an OH group bonded to an external Si atom [37]. The intensity of this band slightly increases with the progress of EDTA treatment suggesting the formation of external structural defects [49]. This band is considered to be non-acidic or weakly acidic [8]. The band around 3745 cm^{-1} is generally assigned to isolated external Si-OH attached to silica-alumina or silica fragments [37].

In summary, the characterization by FTIR evidenced changes in the amount of OH groups in the small cavities after modification with EDTA (band at 3566 cm^{-1}). Although it is difficult to assert the exact cause of this decrease, it is reasonable to state that it has to do with the redistribution of EFAl species that have relocated in the sodalite cages during EDTA treatment. This perturbs the Brønsted acid groups. For the case of EFAl species of cationic nature, one would expect a more intense band at 3525 cm^{-1} due to perturbed bridging hydroxyl groups in the sodalite cages. This was not seen. An alternative explanation is that entire sodalite units collapse after EDTA treatment, thus depleting the amount of LF sites. This would partially explain the creation of defects indicated by the change of the amount of terminal silanol groups.

3.3.8.2. Ammonia TPD

The analysis of the NH_3-TPD curves for the solids of the present work (**Figure 3.9**) reveals changes in acid sites distribution caused by EDTA treatments. In EDTA-treated samples, the high temperature component of the NH_3-TPD profiles becomes more abundant while the feature at low temperature remains fairly unaffected. A similar observation has been reported by Katada et al. [50], and was explained by the increase in the concentration of certain strong Brønsted acid sites caused by the treatment with EDTA. Indeed, some non-framework Al species have the ability to act as charge-balancing cations. Therefore, their extraction with EDTA would yield to an increase in the concentration of strong Brønsted acid sites [9].

Figure 3.9. NH_3-TPD profiles for the zeolites. The band at high temperature corresponds to ammonia desorbed from strong acid sites.

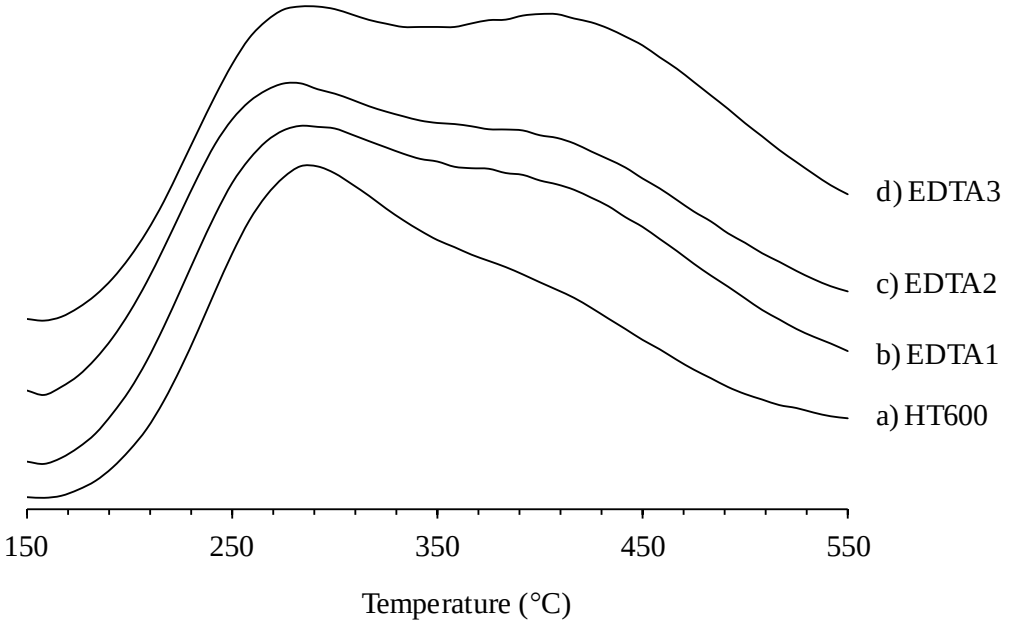

3.3.8.3. Pyridine FTIR

The spectra of the zeolite samples in the region of the bands associated to Brønsted and Lewis acid sites after adsorption and desorption of pyridine is included in **Appendix B2**. Acidity results obtained by adsorption-desorption of pyridine using FTIR spectroscopy are reported in **Table 3.5**. Clearly, EDTA treatments led to solids with progressively higher Brønsted acid sites content. Acid strength is also higher in EDTA-treated samples, as expressed by higher B_{strong}/B_{total} ratios. The increment in total content of Brønsted acid sites after EDTA treatment is consistent with the observed increase in micro- and mesoporous area (**Table 3.1**), and therefore is explained by the enhanced access to pyridine to the inner sites after extraction of polymerized EFAl species obstructing the pore system [51]. The changes in acid strength distribution shown by pyridine-IR are in accord with the observations derived from NH_3-TPD profiles. This is explained taking into account that some EFAl species acting as compensating cations can be extracted with EDTA leading to the release of some strong Brønsted acid sites [9].

Table 3.5. Acidity measured by adsorption-desorption of pyridine monitored by FTIR.

Zeolite		Total[a] (mmol/g)	Strong[b] (mmol/g)
HT600	Brønsted (B)	0.41	0.06
	Lewis (L)	0.39	0.18
	B/L	1.0	
	B_{strong}/B_{total}	0.15	
EDTA1	Brønsted (B)	0.44	0.12
	Lewis (L)	0.33	0.19
	B/L	1.3	
	B_{strong}/B_{total}	0.28	
EDTA2	Brønsted (B)	0.48	0.13
	Lewis (L)	0.29	0.20
	B/L	1.6	
	B_{strong}/B_{total}	0.27	
EDTA3	Brønsted (B)	0.58	0.15
	Lewis (L)	0.30	0.20
	B/L	1.9	
	B_{strong}/B_{total}	0.26	

[a] Total acid sites from pyridine-FTIR (after desorption at 150 °C).

[b] Strong acid sites from pyridine-FTIR (after desorption at 500 °C).

Table 3.5 also shows that Lewis acid sites are slightly depleted, entailing to higher Brønsted to Lewis acid sites ratios. The higher Lewis acidity of HT600 is likely due to its larger amount of extraframework Al. The observed trend in Lewis acidity is in line with ^{27}Al MAS NMR that showed only moderate changes in the relative amount of octahedral Al species after EDTA treatment.

In brief, acidity characterization by NH_3-TPD and pyridine-FTIR reveals that EDTA treatment results in solids with gradually higher acid strength and total density.

3.3.9. Propane conversion and cracking of 1,3,5-tri-isopropylbenzene

Table 3.6 presents the total propane conversion rates, the turnover frequencies (TOF) per total Brønsted acid site (as measured by pyridine-FTIR, **Table 3.5**) for the zeolites and the conversion of 1,3,5-TIPB for the extruded supports. It can be noted that the total conversion rate of propane gradually increases with the severity of EDTA treatments. This is in turn reflected in increasing TOF values. **Table 3.6** also shows that the ratio of

rate of propane cracking over rate of dehydrogenation increases with the severity of the EDTA treatment. Propane is a small molecule that can diffuse and react in all pores of the zeolite [14]. According to Xu et al. [14] propane conversion reaction over USY zeolites likely probes only the strongest active Brønsted acid sites. In the present work it was observed that the amount of strong Brønsted acid sites was increased after EDTA treatment. Therefore, our activity trend for propane conversion can be correlated to the higher density of strong Brønsted acid sites that become available to react with propane.

Table 3.6. Acid catalytic activity of the zeolites and extruded supports.

Zeolite	Propane cracking reaction			1,3,5 TIPB conversion, (%)[d]
	r_{total} x10^{-6} (mol/g·s)[a]	r_{crack}/r_{des} [b]	TOF (total)[c] (mol/g·s) x 10^{-3}	
HT600	0.8	0.8	1.9	34.0
EDTA1	1.1	1.3	2.6	41.0
EDTA2	1.3	1.6	2.8	40.3
EDTA3	1.7	1.9	3.0	37.8

[a] Total reaction rate for propane conversion.

[b] Cracking reaction rate over dehydrogenation reaction rate.

[c] Turnover frequency for overall propane conversion (per total Brønsted acid sites from pyridine-FTIR).

[d] Referred to the activity of the extruded supports (modified zeolite + alumina).

From the 1,3,5-TIPB cracking tests results, it can be noted that all EDTA-treated zeolites give higher 1,3,5-TIPB conversion than the hydrothermally treated Y zeolite. Now, comparing the results for the set of EDTA-treated samples, it can be observed that the EDTA1 sample exhibits higher 1,3,5-TIPB conversion than EDTA2 and EDTA3. In comparison to propane cracking tests, activity data for 1,3,5-TIPB does not show a direct relationship with the increments in textural properties or acidity. The conversion of 1,3,5-TIPB has been commonly used as a test reaction to depict the behavior of heavy hydrocarbons feedstock. The 1,3,5-TIPB reactant has a kinetic diameter of ~ 0.94 nm, which makes it too bulky to enter the micropore system of faujasite zeolite (openings of 0.74 nm). Accordingly, it is expected that 1,3,5-TIPB preferentially interacts with all the acid sites located at the external surface of the zeolite particles and the accessible mesopores [15, 20, 52]. This compound has been converted over diverse

acidic catalysts such as Y zeolite [15, 17, 18, 20], composites of Y-zeolite-amorphous silica-alumina [16, 53], ZSM-5, MOR and Beta zeolite [19, 52]. According to literature studies, the increase in external and mesoporous surface area of zeolites after chemical treatments increases the opportunity for the 1,3,5-TIPB molecules to be cracked [19, 20]. Therefore, the higher 1,3,5-TIPB conversion shown by the EDTA-treated samples of the present study in comparison to the HT600 zeolite is explained by the enhanced accessibility to acid sites since the treatment significantly increases the mesoporous surface area. Enhancement in cracking activity of 1,3,5-TIPB of USY zeolite after treatment with EDTA has also been related to the increase of strong Brønsted acid sites [50].

Nevertheless, the above mentioned factors related to better accessibility and acidity fail to explain the declining 1,3,5-TIPB conversion trend shown by the three EDTA-treated samples since the mesoporosity and acid sites continuously increase with the severity of treatment. Therefore, the results for the EDTA-treated zeolites need alternative explanations. This will be addressed in more detail in the discussion of the VGO hydrocracking activity.

3.3.10. Properties of NiMoP supported catalysts

Table 3.7 presents the textural properties and the chemical composition of the final composite hydrocracking catalysts containing alumina and NiMoP. The textural properties of the catalysts vary in line with the observed trend for the modified zeolites (**Table 3.1**). The metals and phosphorous loadings were lower than the intended values. However, similar Ni/Mo ratios were obtained for all the catalysts.

As in the study of chapter 2, further characterizations with UV-Vis DRS, Laser Raman Spectroscopy and XPS were performed to zeolite-alumina composite supported NiMoP catalysts. The results are presented in Appendix C. The data asserted only minor differences in the dispersion of Ni and Mo oxide species on the supports, the Mo-support interaction and the sulfided state of the catalyst after activation in H_2S/H_2 flow.

Table 3.7. Textural properties and chemical compositions of NiMoP-supported catalysts.

Catalyst	Textural properties		Chemical composition			
	S_{BET} (m^2/g)[a]	V_{Total} (cm^3/g)[c]	NiO (wt.%)	MoO_3 (wt.%)	P_2O_5 (wt.%)	Ni/Mo
NiMoP/(HT600+Alumina)	288	0.30	2.3	14.1	1.9	0.33
NiMoP/(EDTA1+Alumina)	343	0.33	2.2	12.8	1.8	0.34
NiMoP/(EDTA2+Alumina)	369	0.34	2.1	12.9	1.7	0.33
NiMoP/(EDTA3+Alumina)	396	0.57	2.0	12.5	1.9	0.31

[a] BET specific surface area, [b] t-plot micropore area; [c] Total pore volume.

3.3.11. Hydrocracking performance of NiMoP-supported catalysts

The NiMoP-supported catalysts based on the modified zeolites were evaluated in the hydrocracking of a heavy VGO feedstock. In view that the same method was used for incorporating the metals and that the catalysts contain the same amount of zeolite, the catalytic performances in the hydrocracking tests can be reasonably attributed to the catalyst acid function, and specifically, to the effects of the treatment method on the states of aluminum in the modified USY zeolites.

Under the experimental conditions used for the hydrocracking tests, a progressive deactivation trend was observed for all catalysts. Typically hydroprocessing catalysts show fast deactivation during the first few days on stream, after which a long period of almost stable activity is attained [54, 55]. That steady state activity stage was not achieved during the catalytic runs of 110 h on stream. The cumulative poisoning of the acid sites by ammonia coming from the decomposition of nitrogen compounds present in the feed and the progressive formation of carbonaceous deposits (coke) are probably the main factors responsible for the activity decline [55, 56]. It was not the aim of this study to develop a new formulation of a hydrocracking catalyst based on the EDTA-treated zeolites. Therefore, obtaining detailed insights about the deactivation mechanism was not addressed. Certainly, adjusting the catalysts properties, e.g. the (de)-hydrogenation over acidity ratio, or the operating conditions may enhance their long-term performance [57].

Hydrocracking activities and yields to naphtha and middle distillates after 80 h on stream are presented in **Table 3.8**. The activity trend for the catalysts is NiMoP/(EDTA1+Alumina) > NiMoP/(EDTA2+Alumina) > NiMoP/(EDTA3+Alumina) > NiMoP/(HT600+Alumina). Activities in VGO hydrocracking are in line with the ones shown by the 1,3,5-TIPB cracking tests (activity of EDTA1 > EDTA2 > EDTA3 > HY600). In both tests all the catalysts based on EDTA-treated zeolites show higher activity than the one based on the reference hydrothermally treated zeolite (HT600). Additionally, the catalyst based on the EDTA1 zeolite, which was obtained under the least severe treatment conditions, was more active than the other two EDTA-treated samples. The comparison at the same reaction temperature also indicates that in all cases naphtha yields are higher than middle distillates yields.

Table 3.8. Comparison of VGO hydrocracking activities after 80 h on stream.

Catalyst	Conversion of 370 °C^{+} cut (%)[a]	Yields (wt.%)	
		Middle distillates[b]	Naphtha[c]
NiMoP/(HT600+Alumina)	45	17	28
NiMoP/(EDTA1+Alumina)	56	20	36
NiMoP/(EDTA2+Alumina)	53	21	32
NiMoP/(EDTA3+Alumina)	49	18	31

[a] Values reported after 80 h on stream.

[b] Based on the 180-370 °C cut wt.% in the liquid fraction of products.

[c] Based on the IBP-180 °C cut wt.% in the liquid fraction of products.

The higher VGO hydrocracking activity showed by the catalysts based on EDTA-treated zeolites with respect to the one based on the parent steam-treated zeolite is coherent with the enhancements in textural and acid properties shown by these solids. EDTA treatment results in solids with increased mesoporous area, which supposes better access for feedstock molecules to the cracking sites. Additionally, the acid sites strength and density increase after EDTA treatment as indicated by pyridine-FTIR and NH_3-TPD curves. Consequently, the combination of these factors explains the enhanced

hydrocracking activity displayed by the catalysts based on EDTA-treated zeolites in relation to the one based on the hydrothermally treated zeolite.

Rationalizing the declining in VGO hydrocracking activity trend shown by the three catalysts based on EDTA-treated zeolites requires a deeper inspection of changes in the zeolite properties induced by the treatment. In first instance, the parallel behavior between VGO and 1,3,5-TIPB activity suggests in principle that increasing the severity of treatment entails to decreasing accessibility to acid sites. However, the textural characterization of the zeolites showed that EDTA treatment progressively increases the mesoporous surface area and pore volume. Therefore, the most severe treated sample (EDTA3) should have better accessibility than EDTA2 and EDTA1. Recent literature reports have shown that accessibility in chemically-treated zeolites increases when mesoporous surface area is developed [19, 20]. The decreasing activity cannot be explained either by depletion of the global acidity since pyridine-FTIR measurements confirm that the total amount and the strength of the acid sites gradually increase with the severity of treatment. Additionally, the three EDTA-treated zeolites contain similar number of framework Al since they have comparable values of unit cell sizes and Si/Al ratio obtained by ^{29}Si MAS NMR. This feature makes particular the set of samples of the present study. Therefore, the activity trend cannot be attributed to depletion of framework acid sites. Consequently, the explanation of the declining activity trend for the set of catalysts based on EDTA-treated zeolites is linked to the content of EFAl species. Textural characterization, elemental analysis, XPS spectroscopy, and ^{27}Al MAS NMR experiments evidenced the gradual depletion of the content of EFAl. It has been established that some EFAl species present in USY zeolites may play a good catalytic role [3, 6, 58]. Some cationic EFAl species can synergistically interact with the Brønsted acid sites and thereby increase their acid activity [4]. Shertukde et al. [59] found that maxima in cracking activity is a function of both lattice and extralattice aluminum content. Addison et al. [24] observed that the conversion of the heavy fraction of the gas oil feed decreases as EFAl is removed. Some EFAl species such as silica-alumina can show cracking activity by themselves. Therefore their extraction may yield to a decline in the global catalytic performance. Moreover, zeolites with very low EFAl species content, for example those prepared by isomorphous substitution with $(NH_4)_2SiF_6$, exhibit lower cracking activity compared to the conventional steam treated zeolites having comparable levels of framework Al [60]. Therefore, to explain the

dropping activity trend for the three catalysts based on EDTA-treated zeolites it is deduced that severe EDTA treatment diminishes the content of key EFAl species interacting with the acid sites accessible to VGO compounds. Consequently, the present study underlines the importance of the presence of some EFAl species for the hydrocracking of real feedstocks. The loss of synergistic interaction between Brønsted acid sites and EFAl species has been alleged before to rationalize the activity depletion in a model reaction after EDTA treatment [9].

The catalyst based on the EDTA2 zeolite shows higher middle distillate yield than the one based on EDTA1. This behavior suggests that with certain EDTA treatment conditions it is possible to alter the product distribution profiles of the hydrocracking catalyst. Nevertheless, in general terms, the treatment conditions used to modify the zeolites in the present study result in solids with moderate middle distillate selectivity in hydrocracking of the selected feedstock. This selectivity behavior can be explained by the stronger intrinsic acid nature of the EDTA-treated zeolites, which may induce overcracking of the intermediate products. This is in accord with some similar works from literature employing USY zeolite-based hydrocracking catalysts where strong Brønsted acid sites provided high cracking activity but low middle distillates selectivity [61, 62]. From the results of the present study, it can be inferred that a suitable balance between weak and strong acid sites at the mesopore and external surface of the zeolite crystals seems necessary to obtain zeolites with high yield to middle distillates in VGO hydrocracking.

3.4. CONCLUSIONS

In this chapter, modified USY zeolites with different EFAl species content were obtained by treatment with Na_2H_2-EDTA. The results showed that EDTA is a selective agent for the extraction of EFAl species from USY preserving the framework Al content. However, concomitant with EFAl removal, EDTA induces significant changes in bulk and surface properties, in particular to the Al state in the USY zeolites. The prepared NiMoP supported catalysts based on the modified zeolites were tested in hydrocracking of a heavy VGO. Zeolites treated under mild treatment condition were more active in hydrocracking of VGO than the parent hydrothermally treated USY zeolite. This was attributed to the enhancement in accessibility to acid sites after the

extraction of highly condensed EFAl species. Severe treatment conditions with EDTA resulted in decreasing hydrocracking activity ascribed to progressive removal of EFAl species involved in the cracking catalysis. The present study therefore point out the importance of the presence of some EFAl species for the hydrocracking of real feedstocks. The positive/negative effect observed in VGO hydrocracking for the catalysts based on the modified zeolites depends on the conditions used during the EDTA treatment. This work also shows that even with supports with increased mesoporosity and stronger acid character, higher hydrocracking activity of a real feedstock is not guaranteed.

REFERENCES

[1] J. Scherzer, Hydrocracking Science and Technology, Marcel Dekker, New York, 1995.

[2] S. Van Donk, A.H. Janssen, J.H. Bitter, K.P. de Jong, Catalysis Reviews 45 (2003) 297-319.

[3] R.A. Beyerlein, G.B. McVicker, Studies in Surface Science and Catalysis 134 (2001) 3-40.

[4] S.M. Almutairi, B. Mezari, G.A. Filonenko, P.C. Magusin, M.S. Rigutto, E.A. Pidko, E.J. Hensen, ChemCatChem 5 (2013) 452-466.

[5] S. Li, A. Zheng, Y. Su, H. Zhang, L. Chen, J. Yang, C. Ye, F. Deng, Journal of the American Chemical Society 129 (2007) 11161-11171.

[6] N. Malicki, G. Mali, A.-A. Quoineaud, P. Bourges, L.J. Simon, F. Thibault-Starzyk, C. Fernandez, Microporous and Mesoporous Materials 129 (2010) 100-105.

[7] A. Gola, B. Rebours, E. Milazzo, J. Lynch, E. Benazzi, S.L.L. Delevoye, C. Fernandez, Microporous and Mesoporous Materials 40 (2000) 73-83.

[8] S.L. Bao, P. Wu, Q.H. Xu, Chinese Journal of Chemistry 11 (1993) 105-112.

[9] N.P. Rhodes, R. Rudham, Journal of the Chemical Society, Faraday Transactions 89 (1993) 2551-2557.

[10] L. Kubelková, V. Seidl, G. Borbély, H.K. Beyer, Journal of the Chemical Society, Faraday Transactions 1: Physical Chemistry in Condensed Phases 84 (1988) 1447-1454.

[11] R. Dimitrijevic, W. Lutz, A. Ritzmann, Journal of Physics and Chemistry of Solids 67 (2006) 1741-1748.

[12] R. Gounder, A.J. Jones, R.T. Carr, E. Iglesia, Journal of Catalysis 286 (2012) 214-223.

[13] D. Massiot, F. Fayon, M. Capron, I. King, S. Le Calvé, B. Alonso, J.O. Durand, B. Bujoli, Z. Gan, G. Hoatson, Magnetic Resonance in Chemistry 40 (2002) 70-76.

[14] B. Xu, S. Bordiga, R. Prins, J.A. van Bokhoven, Applied Catalysis A: General 333 (2007) 245-253.

[15] A. Bazyari, A. Khodadadi, N. Hosseinpour, Y. Mortazavi, Fuel Processing Technology 90 (2009) 1226-1233.

[16] N. Hosseinpour, Y. Mortazavi, A. Bazyari, A. Khodadadi, Fuel Processing Technology 90 (2009) 171-179.

[17] E.F.S. Aguiar, M.P. Silva, D.F. Silva, Zeolites 15 (1995) 620-623.

[18] Z. Qin, B. Shen, Z. Yu, F. Deng, L. Zhao, S. Zhou, D. Yuan, X. Gao, B. Wang, H. Zhao, Journal of Catalysis 298 (2013) 102-111.

[19] K. Tarach, K. Góra-Marek, J. Tekla, K. Brylewska, J. Datka, K. Mlekodaj, W. Makowski, M. Igualada López, J. Martínez Triguero, F. Rey, Journal of Catalysis 312 (2014) 46-57.

[20] Z. Qin, B. Shen, X. Gao, F. Lin, B. Wang, C. Xu, Journal of Catalysis 278 (2011) 266-275.

[21] C.B.a.L.B. McCusker, Database of Zeolite Structures, The International Zeolite Asociation (IZA), http://www.iza-structure.org/databases/, 2015.

[22] A. Janssen, A. Koster, K. De Jong, The Journal of Physical Chemistry B 106 (2002) 11905-11909.

[23] T. Fleisch, B. Meyers, G. Ray, J. Hall, C. Marshall, Journal of Catalysis 99 (1986) 117-125.

[24] S. Addison, S. Cartlidge, D. Harding, G. McElhiney, Applied catalysis 45 (1988) 307-323.

[25] R. Chal, C. Gérardin, M. Bulut, S. van Donk, ChemCatChem 3 (2011) 67-81.

[26] L. Aouali, J. Teanjean, A. Dereigne, P. Tougne, D. Delafosse, Zeolites 8 (1988) 517-522.

[27] D.-S. Liu, S.-L. Bao, Q.-H. Xu, Zeolites 18 (1997) 162-170.

[28] M.J. Remy, D. Stanica, G. Poncelet, E.J.P. Feijen, P.J. Grobet, J.A. Martens, a.P.A. Jacobs, J. Phys. Chem. 100 (1996) 12440-12447.

[29] J. Dwyer, F.R. Fitch, F. Machado, G. Qin, S.M. Smyth, J.C. Vickerman, Journal of the Chemical Society, Chemical Communications (1981) 422-424.

[30] T. Gross, U. Lohse, G. Engelhardt, K.-H. Richter, V. Patzelova, Zeolites 4 (1984) 25-29.

[31] A. Omegna, J.A. van Bokhoven, R. Prins, The Journal of Physical Chemistry B 107 (2003) 8854-8860.

[32] J. Van Bokhoven, A. Roest, D. Koningsberger, J. Miller, G. Nachtegaal, A. Kentgens, The Journal of Physical Chemistry B 104 (2000) 6743-6754.

[33] N. Katada, S. Nakata, S. Kato, K. Kanehashi, K. Saito, M. Niwa, Journal of Molecular Catalysis A: Chemical 236 (2005) 239-245.

[34] G. Ray, B. Meyers, C. Marshall, Zeolites 7 (1987) 307-310.

[35] S.M.C. Menezes, V.L. Camorim, Y.L. Lam, R.A.S.S. Gil, A. Bailly, J.P. Amoureux, Applied Catalysis A: General 207 (2001) 367–377.

[36] J. Dwyer, Studies in Surface Science and Catalysis 37 (1988) 333-354.

[37] I. Halasz, M. Agarwal, B. Marcus, W.E. Cormier, Microporous and mesoporous materials 84 (2005) 318-331.

[38] S. Khabtou, T. Chevreau, J. Lavalley, Microporous materials 3 (1994) 133-148.

[39] N. Malicki, P. Beccat, P. Bourges, C. Fernandez, A.-A. Quoineaud, L.J. Simon, F. Thibault-Starzyk, Studies in Surface Science and Catalysis 170 (2007) 762-770.

[40] G. Garralon, A. Corma, V. Formes, Zeolites 9 (1989) 84-86.

[41] M. Niwa, K. Suzuki, K. Isamoto, N. Katada, The Journal of Physical Chemistry B 110 (2006) 264-269.

[42] E.J.M. Hensen, D.G. Poduval, D.A.J.M. Ligthart, J.A.R. van Veen, M.S. Rigutto, The Journal of Physical Chemistry C 114 (2010) 8363-8374.

[43] O. Cairon, ChemPhysChem 14 (2013) 244-251.

[44] P.O. Fritz, J.H. Lunsford, Journal of Catalysis 118 (1989) 85-98.

[45] M.A. Makarova, J. Dwyer, The Journal of Physical Chemistry 97 (1993) 6337-6338.

[46] P. Hoffmann, J.A. Lobo, Microporous and Mesoporous Materials 106 (2007) 122-128.

[47] O. Cairon, K. Thomas, T. Chevreau, Microporous and Mesoporous Materials 46 (2001) 327-340.

[48] A. Corma, V. Fornes, A. Martinez, F. Melo, O. Pallota, Studies in Surface Science and Catalysis 37 (1988) 495-503.

[49] J. Datka, W. Kolidziejski, J. Klinowski, B. Sulikowski, Catalysis letters 19 (1993) 159-165.

[50] N. Katada, Y. Kageyama, K. Takahara, T. Kanai, H.A.B. , M. Niwa, Journal of Molecular Catalysis A: Chemical 211 (2004) 119–130.

[51] C.S. Triantafillidis, A.G. Vlessidis, N.P. Evmiridis, Ind. Eng. Chem. Res. 39 (2000) 307-319.

[52] A. Corma, V. Fornés, L. Forni, F. Marquez, J. Martınez-Triguero, D. Moscotti, Journal of Catalysis 179 (1998) 451-458.

[53] M. Aghakhani, A. Khodadadi, S. Najafi, Y. Mortazavi, Journal of Industrial and Engineering Chemistry (2013).

[54] J. Gosselink, W. Stork, Industrial & engineering chemistry research 36 (1997) 3354-3359.

[55] E. Furimsky, F.E. Massoth, Catalysis Today 52 (1999) 381-495.

[56] M. Guisnet, P. Magnoux, D. Martin, Studies in surface science and catalysis 111 (1997) 1-19.

[57] R. Henry, M. Tayakout-Fayolle, P. Afanasiev, C. Lorentz, G. Lapisardi, G. Pirngruber, Catalysis Today 220 (2014) 159-167.

[58] S. Li, A. Zheng, Y. Su, H. Zhang, L. Chen, J. Yang, F.D. Chaohui Ye, J. AM. CHEM. SOC. 129 (2007) 11161-11171.

[59] P. Shertukde, W. Hall, J. Dereppe, G. Marcelin, Journal of catalysis 139 (1993) 468-481.

[60] R. Beyerlein, G. McVicker, L. Yacullo, J. Ziemiak, The Journal of Physical Chemistry 92 (1988) 1967-1970.

[61] M. Ali, T. Tatsumi, T. Masuda, Applied Catalysis A: General 233 (2002) 77-90.

[62] P. Dik, O. Klimov, G. Koryakina, K. Leonova, V.Y. Pereyma, S. Budukva, E.Y. Gerasimov, A. Noskov, Catalysis Today 220 (2014) 124-132.

4. EFFECT OF USY ZEOLITE CHEMICAL TREATMENT WITH AMMONIUM NITRATE ON ITS VGO HYDROCRACKING PERFORMANCE

SUMMARY

Chemically modified USY zeolites were obtained by ammonium nitrate (AN) treatment under hydrothermal conditions. Further treatment with Na_2H_2-EDTA to a selected AN-treated zeolite was also performed. AN treatment considerably enhanced the mesopore volume of the parent steam-treated zeolite. This treatment also caused the creation of extraframework species of weak acid nature. NiMoP-based hydrocracking catalysts were prepared using the modified zeolites and evaluated in the hydrocracking of a heavy VGO. Hydrocracking activity results indicate that although AN treatment significantly develops mesoporosity in the parent steam treated USY zeolite, this single treatment was not efficient to enhance the accessibility of VGO compounds to the acid sites. However, the catalysts based on AN-treated zeolites showed significantly higher middle distillates yields than the one based on the steam-treated zeolite. The creation of an amorphous phase at the mesopore walls and the external surface of the zeolite crystals was argued to support this observation. Mild EDTA treatment to an AN-treated zeolite showed to be beneficial to improve the hydrocracking activity. This was attributed to the enhanced access to acid sites after the removal of polymerized EFAl species. Consequently, a modification strategy of USY zeolites that combines AN and EDTA treatments is proposed to develop catalysts with enhanced activity and middle distillates selectivity in the hydrocracking of real feedstocks.

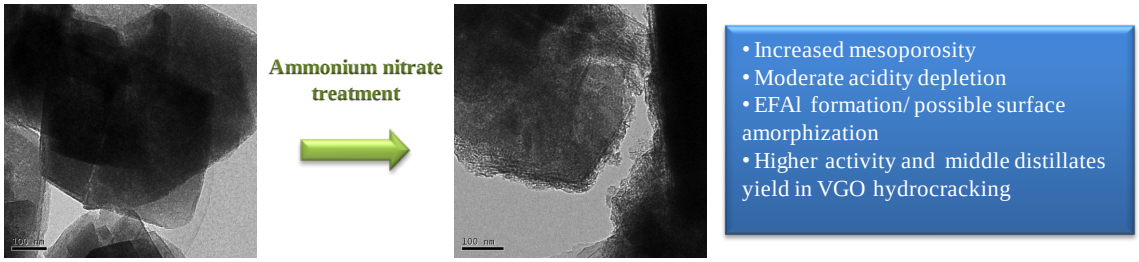

4.1. INTRODUCTION

Conventional USY Zeolite-based hydrocracking catalysts are more active than amorphous silica alumina (ASA)-based catalysts, although the former yield less middle distillates, in part due to the presence of stronger acid sites and smaller pores. The USY zeolite has most of its active sites inside the micropores that are often smaller than the molecules that are being converted in real applications; thus, molecular access to the interior active catalytic sites is limited by diffusion. Additionally, when the primary cracked products are delayed in leaving the zeolite crystal, they have a higher probability of overcracking to lighter products [1]. For hydrocracking, this behavior reduces the middle distillates yield and increases the coke forming tendency. With the goal of maximizing middle distillates, it is desirable to design hydrocracking catalysts that combine the good activity of the USY-zeolite based catalysts with the middle distillates selectivity of the ASA-based ones. One strategy to achieve this goal is therefore to improve the intra-particle diffusion transport properties of the zeolites.

The approaches to obtain zeolites with alleviated diffusion limitations can be classified in three main groups: (i) synthesis of zeolites with larger micropores or direct creation of mesopores, (ii) synthesis of zeolites of small crystals size, and (iii) post-synthesis methods designed to introduce additional mesoporosity [2-5]. Although notorious improvements have been achieved with the different approaches, some important economical and technical restrictions such as the use of expensive reactants, the formation of environmental pollutants, and the difficulty in controlling the zeolite structural degradation have limited their implementation in commercial applications [6, 7]. Recent research efforts have focused on the development of zeolites that have both the advantages of an organized mesoporous structure and those of a microcrystalline network [8]. This kind of materials has been termed hierarchical or mesoestructured zeolites [3]. In regard to hydrocracking, post-synthesis methods are mostly used to obtain USY zeolites to be used as the cracking function component. However, relatively few examples of USY-zeolite based hydrocracking catalysts with improved molecular traffic within the zeolite have been reported in open literature [7, 9-13].

In the previous chapter, the combination of hydrothermal treatment and Na_2H_2-EDTA treatment on USY zeolite improved the VGO hydrocracking performance [14]. Those results led to better explore the role of the zeolite acid sites accessibility in hydrocracking. Among different chemical modification methods, the treatment of USY

zeolites with aqueous solutions of NH_4NO_3 has been shown to be effective in enhancing the zeolite mesoporosity [15]. To the author's knowledge, no hydrocracking catalytic studies have been undertaken with solids obtained by this post-treatment method. In the present chapter it was studied the effect of the enhancement in the mesoporosity of a steam-treated USY zeolite by ammonium nitrate (AN) treatment on the hydrocracking performance of a real feedstock. The effect of further treatment with Na_2H_2-EDTA to a selected AN-treated zeolite was also studied.

4.2. EXPERIMENTAL

4.2.1. Preparation of the modified zeolites and hydrocracking catalysts

Chemical hydrothermal treatments with NH_4NO_3 solutions (hereinafter "AN") were performed to the same steam-treated zeolite used in the study of the chapter 3 (HT600). The procedure was adapted from Cooper et al. [15]. Typically, a portion of the sample HT600 was suspended in a 6N NH_4NO_3 aqueous solution at a ratio of 4.4 mL/g of zeolite in a Teflon-lined autoclave and treated at 120 or 180 °C for 6 h followed by filtration, washing, drying at 105 °C for 14-16 h and calcination at 550 °C for 4 h. This procedure yielded to samples ANT120 and ANT180, respectively, where "ANT" indicates ammonium nitrate treatment and the number indicate the temperature of treatment. Additionally, a portion of the ANT180 sample was treated in a 0.09 mol/L aqueous solutions of ethylenediamine-tetraacetic acid disodium salt (Na_2H_2-EDTA·$2H_2O$, hereinafter referred as EDTA) at a ratio of 20 mL/g of zeolite, at 85 °C for 2 h under stirring followed by filtration and washing with distilled water, two ion exchanges at 85 °C for 1 h with ammonium nitrate solutions to remove the added Na cations, filtration, washing, drying at 105 °C for 14-16 h and calcination at 550 °C for 4 h. This procedure yielded to sample ANT180-EDTA.

NiMoP-supported hydrocracking catalysts were prepared with the hydrothermally and AN-treated zeolites following the same procedure described in chapter 3.

4.2.2. Characterization methods

4.2.2.1. Textural properties and morphology

Nitrogen adsorption measurements were performed as described in chapter 2.

High Resolution Transmission electron microscopy (HRTEM) pictures of the zeolite particles were taken as detailed in chapter 2.

4.2.2.2. Bulk, surface and framework composition

The bulk, surface and framework composition were measured as reported in chapter 2.

4.2.2.3. Acid properties

Acidity distribution by TPD of ammonia and the Brønsted/Lewis acidity by FTIR spectroscopy of adsorbed pyridine were measured following the same procedure described in chapter 3.

4.2.2.4. Nuclear Magnetic Resonance

The ^{27}Al Magic Angle Spinning (MAS) Nuclear Magnetic Resonance (NMR) spectra of the zeolite samples were recorded at a magnetic field of 11.7 T as reported in chapter 2. The ^{29}Si MAS spectra were recorded at 9.4 T as detailed in chapter 2.

With the aim of providing a coherent understanding of the results described in this chapter, Appendix A further describes the characterization techniques that were used to assess the properties of the modified zeolite and the hydrocracking catalysts.

4.2.3. Activity evaluation of hydrocracking catalysts

Hydrocracking activity tests were performed under the same experimental conditions used for the study of chapter 3.

4.3. RESULTS AND DISCUSSION

4.3.1 XRD patterns

XRD patterns of the zeolites samples are presented in **Figure 4.1**. Both the number of peaks and peak positions agree well with the powder diffraction pattern of a typical Ultrastable Y zeolite (FAU framework type) reported by The International Zeolite Association (IZA) [16]. It can be noted that the treatments do not drastically affect the crystalline order of the USY zeolites.

Figure 4.1. XRD patterns of the zeolite samples.

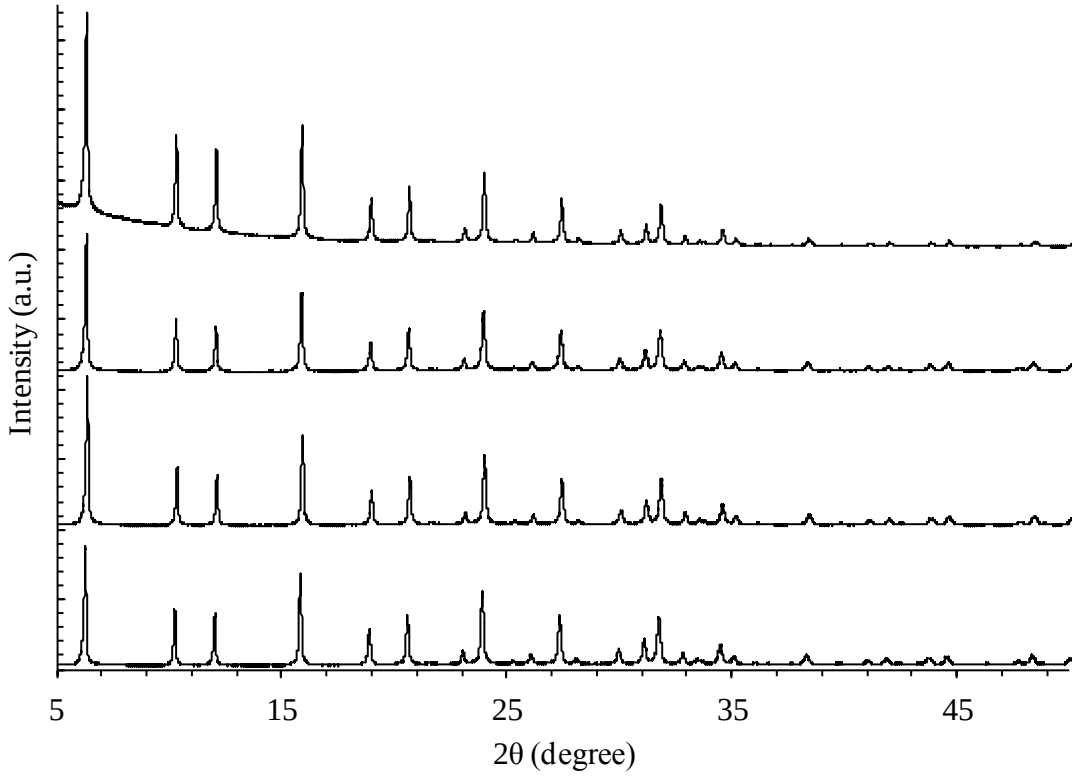

4.3.2. Textural properties of the modified zeolites

Figure 4.2 presents the nitrogen adsorption and desorption isotherms of the modified USY zeolites. The samples show type IV isotherms with hysteresis loops indicative of materials possessing both micro and mesoporosity. For HT600 the hysteresis loop is slightly flat, indicating inkbottle type pores, whereas the progressive change to upward curvature in the hysteresis loop of the AN-treated samples is indicative of progressive development of cylindrical type of pores [17].

The pore size distributions of the AN-treated zeolites are presented in **Figure 4.3**. The materials of the present study have relatively wide mesopore size distributions with a maximum around 160 Å in the case of HT600 (**Figure 4.3a**). The AN-treated samples have predominantly dual pore systems, one centered at around 60–80 Å likely associated to small intra-crystalline mesopores, and other centered at around 250 Å. The bigger mesopores are believed to be created during the initial hydrothermal treatment [18]. AN treatment at 180 °C seems to favor the development of the small mesopores. The further treatment with EDTA broadens the pore size distribution of the mesopores

contained in the sample ANT180. This change is most likely due to the removal of amorphous species from the mesopore system [19]. The mechanism to describe the creation of mesoporosity by AN treatment has not been studied before. Similar results in terms of the size distribution of the created mesopores have been observed by Aels et al. [20] with treatment using NH_4OH in a USY zeolite, and by Tarach et al. [21] with NaOH/TBAOH treatment in a Beta zeolite. Also de Jong et al. [13] have reported the creation of small cavity-like mesopores of 3 nm in average after desilication with NaOH of a USY zeolite.

Figure 4.2. Nitrogen physisorption isotherms of AN-treated zeolites. a) HT600, b) ANT120, c) ANT180, and d) ANT180-EDTA. Curves were vertically shifted according to the following values: a) no shift, b) 1 mmol/g, c) 2 mmol/g, d) 3 mmol/g.

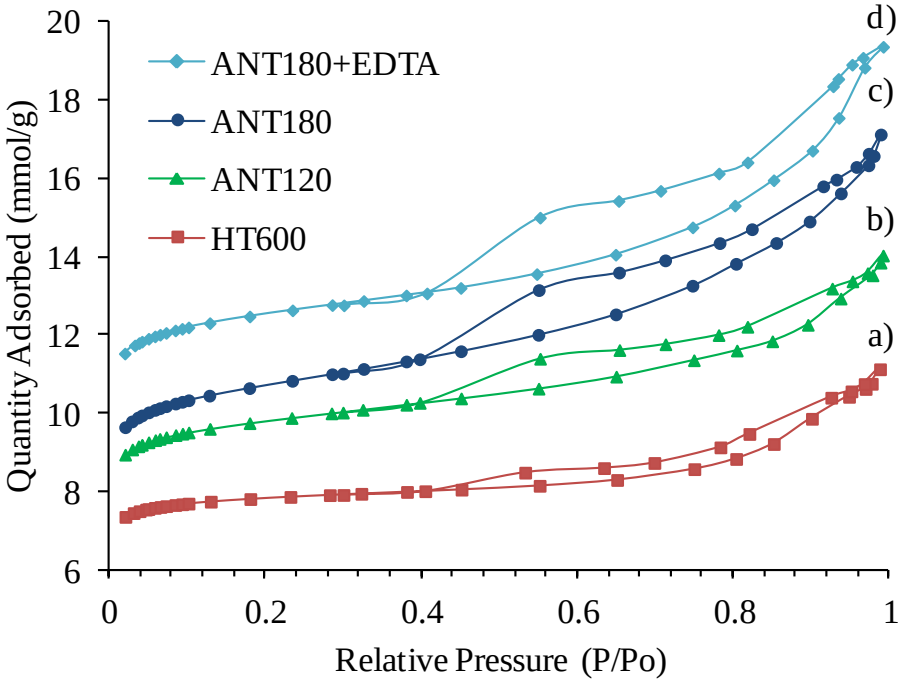

Figure 4.3. Pore size distributions of the AN-treated zeolites. a) HT600, b) ANT120, c) ANT180, and d) ANT180-EDTA. Curves were vertically offset according to the following values: a) no shift, b) 0.125 $cm^3/g \cdot Å$, c) 0.15 $cm^3/g \cdot Å$, d) 0.3 $cm^3/g \cdot Å$.

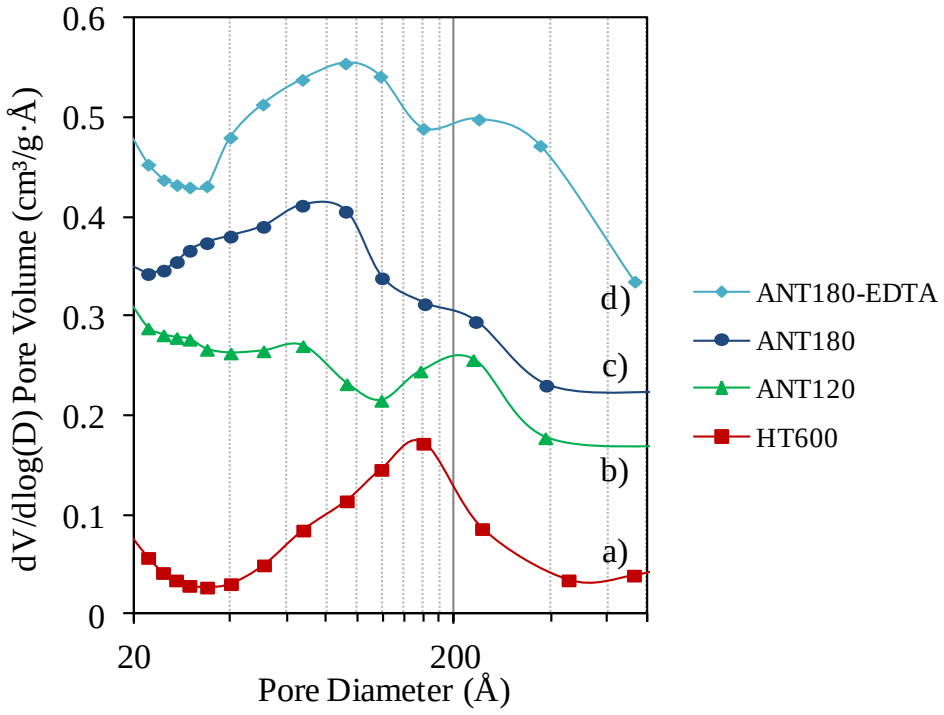

The main textural properties of the modified zeolites are presented in **Table 4.1**. Clearly, the mesoporosity is significantly increased in AN-treated zeolites with respect to the parent HT600 sample, as indicated by the higher mesopore volume and surface area values. Moreover, the higher the temperature of AN treatment, the higher the mesoporosity is developed. At the same time, the micropore volume and area gradually decrease with the AN treatment. The external surface area increased to more than double and triple for samples ANT120 and ANT180, respectively. This progressive increase in mesoporosity seems to occur at the expense of the partial deterioration of the microporous area. However, partial blocking of the micropores by extraframework material produced during the treatment is also possible. Now, when the ANT180 sample in subjected to further EDTA treatment (sample ANT180-EDTA), microporosity is recovered, showing the same values of microporous area and micropore volume of the reference hydrothermally treated zeolite HT600. The solid ANT180-EDTA contains, therefore, increased micro- and mesoporosity. As in chapter 3, this result is most probably due to the removal of some extraframework aluminum species formed during

hydrothermal treatment that block the micropore system. In the previous chapter this leaching agent showed to be selective for EFAl removal without affecting the zeolite framework. Similar observations have also been reported before [22].

Table 4.1. Textural properties of the modified zeolites.

Zeolite	S_{BET} (m^2/g)[a]	S_{micro} (m^2/g)[b]	S_{meso} (m^2/g)[c]	V_{total} (cm^3/g)[d]	V_{micro} (cm^3/g)[e]	V_{meso} (cm^3/g)[f]
HT600	686	624	62	0.39	0.26	0.13
ANT120	729	587	142	0.45	0.24	0.21
ANT180	720	529	190	0.52	0.22	0.31
ANT180-EDTA	790	625	165	0.57	0.26	0.31

[a] BET specific surface area, [b] t-plot micropore area, [c] t-plot external surface area, [d] Total pore volume, [e] t-plot micropore volume, [f] Mesopore volume.

4.3.3. Morphological characterization

Figure 4.4 presents representative HRTEM images of the HT600 and ANT180 zeolites. Apparently, the ANT180 zeolite grains have an external surface more irregular than the one of the zeolite HT600 (comparison of **Figure 4.4a**, **Figure 4.4c**, **Figure 4.4d** and **Figure 4.4e**). Some small defects (external protuberances) are clearly visible in ANT180 zeolite (**Figure 4.4c** and **Fig 4.4d**). In **Figure 4.4e** some crystal cracks are clearly visible. These images suggest that the morphology of the zeolite crystals is significantly affected by the AN treatment. **Figure 4.4f** presents an image of an ANT180 zeolite crystal at increased magnification. An amorphous layer at the exterior surface of the zeolite particle is noticeable.

4.3.4. ^{29}Si MAS NMR characterization

The experimentally obtained and deconvoluted ^{29}Si MAS NMR spectra of the samples are shown in **Figure 4.5**. In all of the modified-zeolites, silicon species with 0Al neighbors dominate the spectra. The visual inspection of the spectra does not reveal severe changes in the silicon species distribution.

Table 4.2 compiles the relative intensities of the peaks associated to each Q^4(nAl) environment for the modified zeolites. The increase of relative intensities of Si(3Al), Si(2Al) and Si(1Al) species, and the decrease of Si_{EF} species after performing the AN

treatment to the HT600 zeolite, suggest that this agent is able to reinsert to the framework some extraframework species.

Figure 4.4. HRTEM images of the HT600 and ANT180 zeolites.

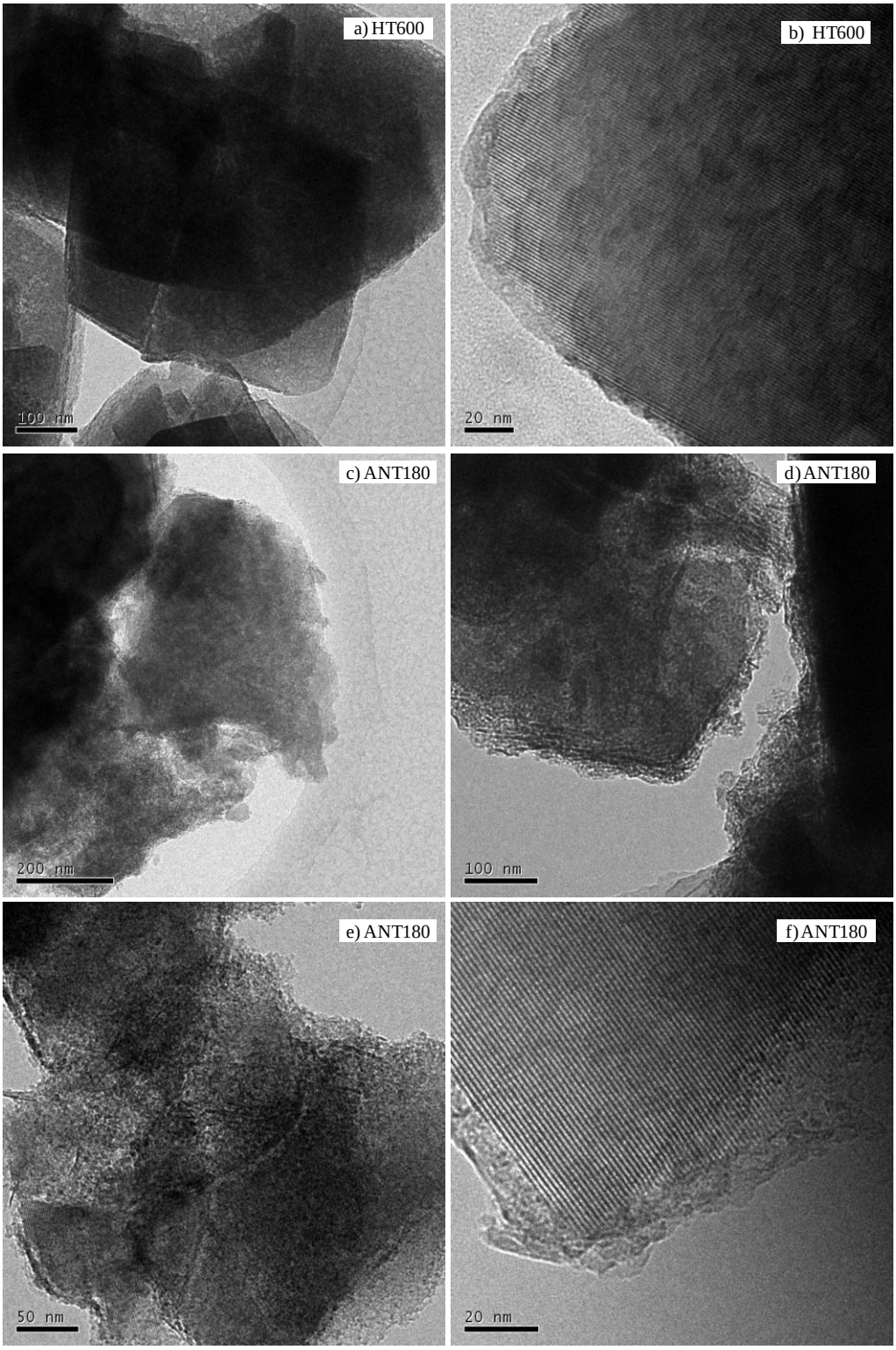

Figure 4.5. ^{29}Si MAS NMR spectra of the modified Y zeolites. In each spectrum the solid line represents the experimental curve and the dashed lines corresponds to the Gaussian peaks representing each Q^4(nAl) species.

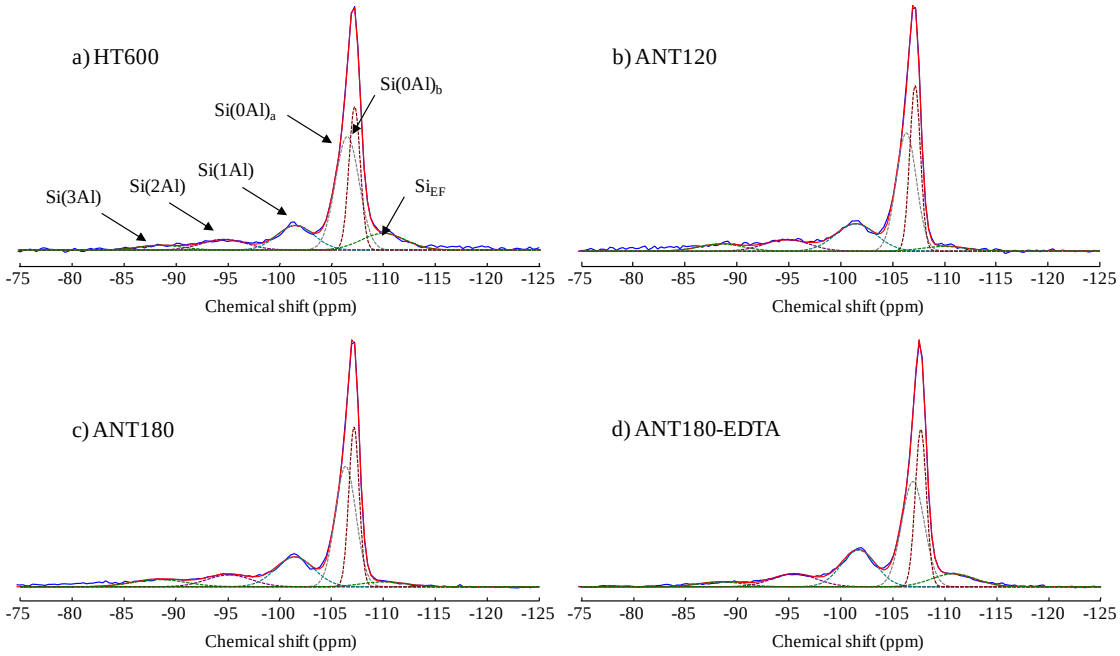

Table 4.2. Relative intensities of the deconvoluted signals from the ^{29}Si MAS NMR spectra.

Signal		HT600	ANT120	ANT180	ANT180-EDTA
Si(3Al)	δ (ppm)	-88.5	-88.5	-88.5	-88.5
	$I_{Si(3Al)}$ (%)	3.4	5.4	5.8	3.2
Si(2Al)	δ (ppm)	-94.7	-95.1	-95.2	-95.5
	$I_{Si(2Al)}$ (%)	7.0	8.3	9.2	8.5
Si(1Al)	δ (ppm)	-101.5	-101.43	-101.44	-101.69
	$I_{Si(1Al)}$ (%)	12.9	15.9	16.6	18.9
$Si(0Al)_a$	δ (ppm)	-106.5	-106.3	-106.4	-106.9
	$I_{Si(0Al)}$ (%)	37.8	37.4	38.4	35.3
$Si(0Al)_b$	δ (ppm)	-107.2	-107.2	-107.2	-107.7
	$I_{Si(0Al)}$ (%)	28.5	29.4	26.4	25.8
Si_{EF}	δ (ppm)	-110.0	-110.0	-110.0	-110.0
	$I_{Si(EF)}$ (%)	10.5	3.7	3.7	8.3

4.3.5. Bulk, framework and surface composition the modified zeolites

Table 4.3 presents the bulk, framework and surface Si/Al ratios of the parent and modified zeolites as calculated from ICP-OES, ^{29}Si MAS NMR (from data in **Table 4.2**) and XPS, respectively. The unit cell size for all the zeolites is also indicated. With respect to HT600 zeolite, the bulk Si/Al ratio slightly increases with AN treatment at 120 °C and remains constant when the treatment is done at 180 °C. The further treatment with EDTA to the HT600-ANT180 sample increases the bulk Si/Al ratio, which validates the assumed dealumination ability of this agent.

There is a considerable difference between the bulk and framework Si/Al ratios for the HT600 and AN treated zeolites. This is an evidence of the existence a significant amount of EFAl species in these samples. However, the framework Si/Al decreases after increasing the severity of AN treatment. Several proposals have been reported to explain similar behaviors during chemical treatments. The decrease in the lattice Si/Al may be caused by desilication of the framework. However, at low Si/Al ratios the extraction of framework silicon is inhibited due to the protective role of aluminum [23]. Therefore, this phenomenon is expected to proceed to a limited extent for the samples of the present study. An alternative explanation is that AN treatment results in the reinsertion of some extraframework Al atoms into the lattice. Such phenomenon has been discussed before for alkaline treated Y zeolites [24]. However, AN treatment had little effect on the unit cell size which can be related to framework Si/Al ratio. Consequently, no conclusive interpretations in favor of any proposal can be drawn with the information presented until here.

Table 4.3. Bulk, framework and surface Si/Al ratio of the modified zeolites.

Zeolite	$(Si/Al)_{bulk}$ [a]	$(Si/Al)_F$ [b]	$a_{o,}$ (Å)	$(Si/Al)_{surface}$ [c]
HT600	3.1	9.7	24.384	1.3
ANT120	3.5	7.9	24.379	1.4
ANT180	3.1	7.4	24.379	1.1
ANT180-EDTA	4.0	8.0	24.362	3.3

[a] From chemical analysis, [b] From ^{29}Si MAS NMR data, [c] From XPS.

The surface Si/Al ratio is significantly lower than that of the bulk in HT600, ANT120 and ANT180 sample. This observation means that external surface of the zeolite crystals is enriched in Al. In steam-treated zeolites, this has been explained by the migration of part of the Al atoms expelled during the treatment toward the external surface [25]. AN treatment does not significantly alter the surface Si/Al ratio, which indicates that neither further migration nor EFAl removal take place. Conversely, when the ANT180 sample is subjected to further treatment with EDTA, the surface Si/Al increases. This is explained by the dissolution of extraframework Al [14]. Surface Al content declining in zeolites after chemical treatments has been reported before [26].

In brief, the results presented above indicate that AN treatment is efficient to develop mesoporosity in the starting USY zeolite without affecting significantly the bulk and surface Si/Al ratio. ^{29}Si MAS NMR spectroscopy indicated that the treatment increases the amount of Al atoms at framework positions. Further EDTA treatment decreases the content of EFAl species and enhances the micro and mesoporosity.

4.3.6. ^{27}Al MAS NMR characterization

The ^{27}Al MAS NMR spectra of the treated zeolites are displayed in **Figure 4.6**. The spectra reveal the evolution of the Al species coordination in the samples due to AN treatment. Three main peaks are observed in the spectra for all of the zeolites centered around 60, 30 and 0 ppm. In first instance, for the starting zeolite HT600 (spectrum a) the signal corresponding to tetrahedral Al species is the most intense of the spectrum. For the AN-treated samples at 120 and 180 °C (spectra b and c), it is observed that the region associated to octahedral Al species becomes more intense with respect to the peak ascribed to Al in tetrahedral coordination. Moreover, the higher the temperature of AN treatment, the larger the proportion of Al species in octahedral coordination. Now, when the sample ANT180 is subjected to further chemical treatment with EDTA (spectra d), a notorious depletion of Al species in penta- and octahedral environment is observed.

The increase in the signal ascribed to octahedral Al species implies that this treatment yields to the formation of some EFAl species. In particular, the sharp band at 0 ppm has been attributed to isolated octahedrally coordinated Al such as $Al(H_2O)_6^{3+}$ [27] that is formed as a result of the partial hydrolysis of the framework Al-O bonds [28]. The large

depletion of Al species in penta- and octahedral environment observed for samples ANT180-EDTA confirms the elemental analysis and XPS results (**Table 4.3**), supporting the occurrence of partial removal of some EFAl species.

Figure 4.6. ^{27}Al MAS NMR Spectra of the treated zeolites. a) HT600, b) ANT120, c) ANT180, and d) ANT180-EDTA.

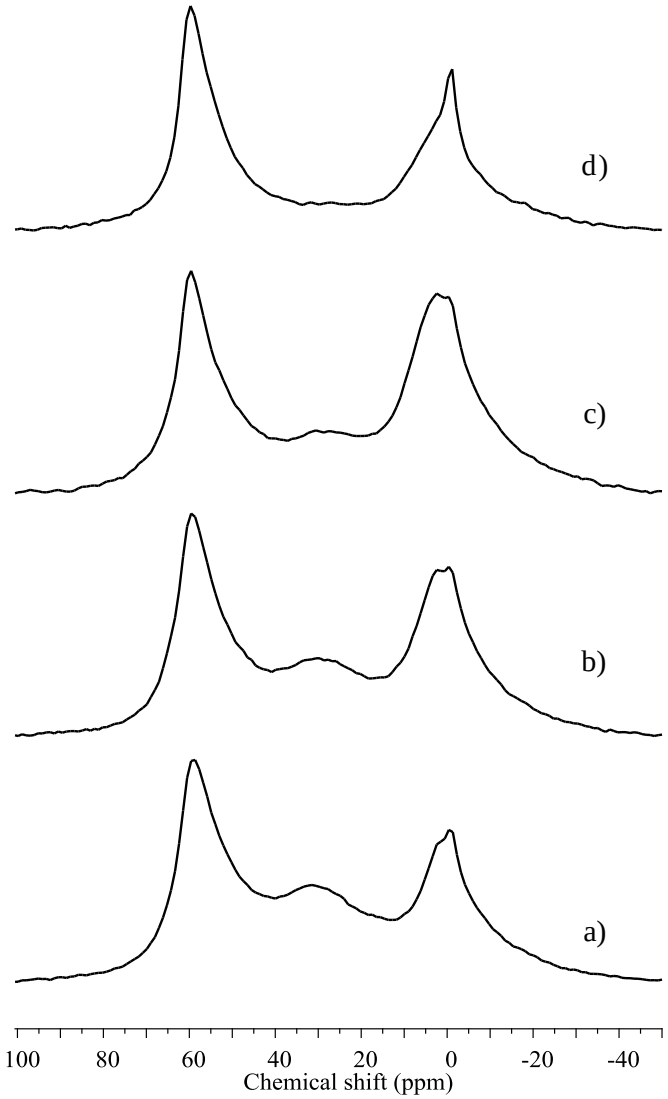

In summary, ^{27}Al MAS NMR experiments indicate that AN treatment increases the proportion of EFAl species in the zeolites. EDTA treatment was able to remove some extraframework Al species contained in the AN-treated sample.

4.3.7. Acid properties

4.3.7.1. Acidity strength distribution from ammonia TPD

The NH_3-TPD curves of the treated zeolites are presented in **Figure 4.7**. Curves show two distinguishable desorption peaks. The low-temperature desorption peak is traditionally ascribed to weakly acidic Brønsted sites, Lewis sites, terminal silanol groups, and acidic sites in extraframework material. The high-temperature desorption peak is associated to strong Brønsted acid sites and some Lewis sites. With respect to the steam-treated zeolite, in AN-treated samples the low temperature peak becomes broader and its peak maxima slightly shift to a lower temperature (curves b and c). This observation suggests that AN treatment induces the formation of weakly acidic species. Further treatment with EDTA to the sample ANT180 causes the depletion of some weak acid sites (curve d). The ANT180-EDTA sample also contains a higher proportion of strong acid sites with respect to the ANT180 and HT600 samples. This is explained by the removal of EFAl acting as charge-balancing species [22]. The increase of certain strong Brønsted acid sites, as a consequence of EDTA treatment, has also been argued [29].

Figure 4.7. NH_3-TPD profiles of the treated zeolites. a) HT600, b) ANT120, c) ANT180, d) ANT180-EDTA.

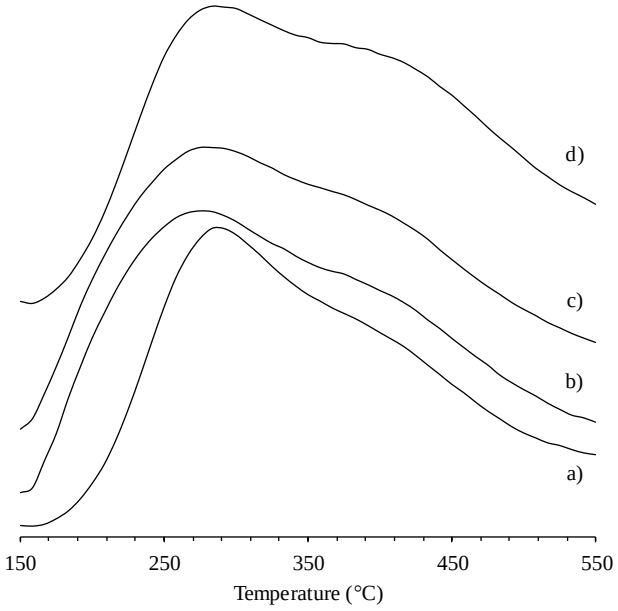

4.3.7.2. Changes in the hydroxyl groups

Infrared spectra in the hydroxyl groups region for the zeolite samples are presented in **Figure 4.8**. The spectra show distinguishable bands with maxima at around 3566, 3600, 3631, 3740 cm^{-1}. The more noticeable changes observed after AN treatment are the depleting of the 3566 cm^{-1} sample and the progressive increase of the 3740 cm^{-1} band with respect to the other three bands in the 3600 cm^{-1} region.

Figure 4.8. FTIR spectra in the OH region for the zeolite samples. a) HT600, b) ANT120, c) ANT180, d) ANT180-EDTA. Positions for the main bands are indicated with dashed lines. Spectra were taken at 150 °C after evacuation in vacuum at 500 °C.

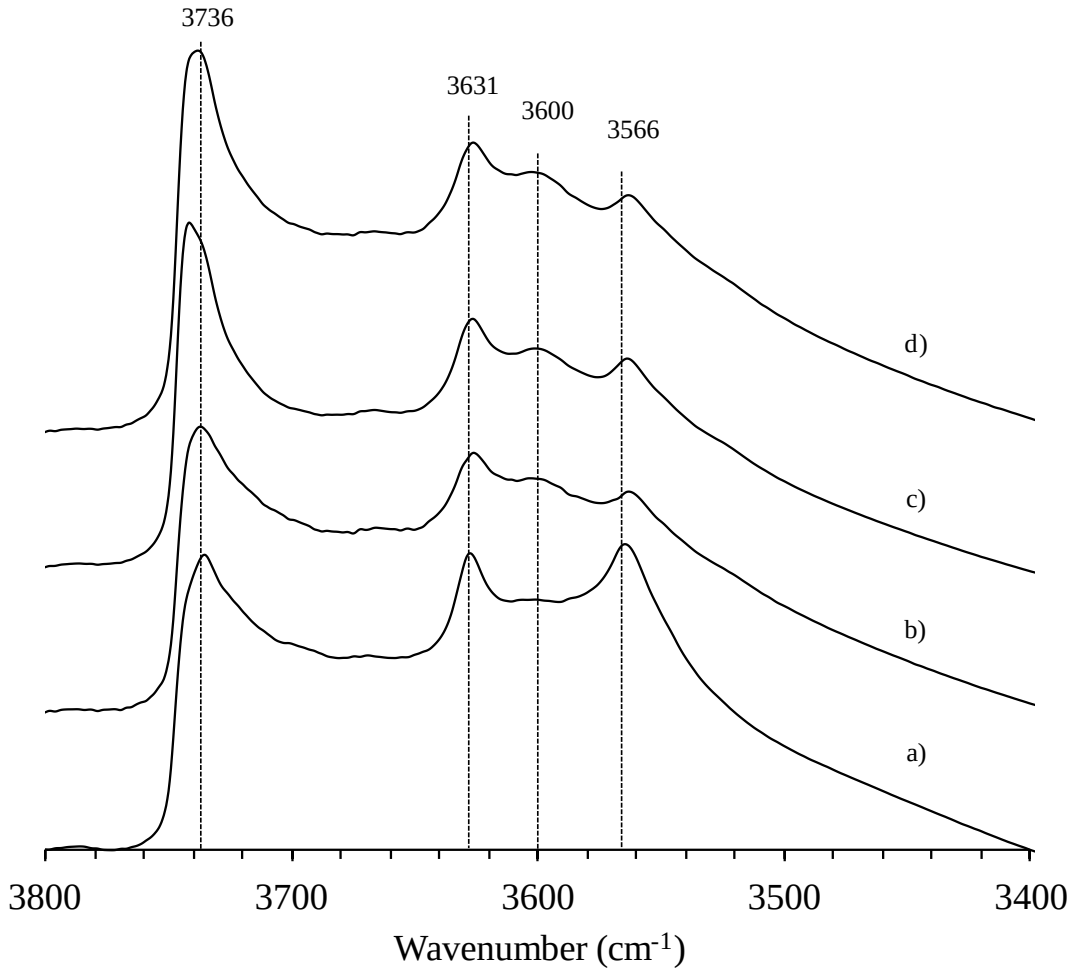

The increase of the intensities of vibrations ascribed to silanol groups indicates that the AN treatment causes progressive development of structural defects. These kind of

hydroxyl groups are considered to be weakly acidic and therefore the FTIR results are consistent with information obtained from the NH_3-TPD profiles that showed increment in the concentration of weak acid sites. Interestingly, a close inspection of the silanol region allows identifying that in AN-treated samples (spectra b and c) the band at 3744 cm^{-1}, ascribed to isolated external terminal Si–OH in silicon-rich amorphous debris [30], progressively increases with respect to the signal at 3736 cm^{-1} assigned to terminal Si-OH groups attached to the framework [31]. This result also confirms the formation of extraframework species. The effect of the further treatment with EDTA to zeolite ANT180 is mainly noticeable in the development of structural defects, as indicated by the increase in the intensity of the band at 3736 cm^{-1} ascribed to terminal silanols (**Figure 4.8d**). This finding is consistent with the results presented in chapter 3 (section 3.3.8.1**).**

4.3.7.3. Acidity from FTIR measurements of adsorbed pyridine

The spectra of the zeolite samples in the region of the bands associated to Brønsted and Lewis acid sites after adsorption and desorption of pyridine is included in **Appendix B3**. Acidity results obtained by pyridine adsorption-desorption followed by FTIR spectroscopy are reported in **Table 4.4**. AN treatment leads to solids with slightly lower Brønsted acid sites content. At the same time, the proportion of medium- and strong-strength Brønsted acid sites increased as expressed by increasing B_{medium}/B_{total} and B_{strong}/B_{total} ratios. This is consistent with the findings obtained from the NH_3-TPD profiles. Lewis to Brønsted acid site ratio increases after AN treatment, which is in accord with the increase in the octahedral-to-tetrahedral Al species regions ratio observed in the ^{27}Al MAS NMR spectra for these samples (**Figure 4.6**). Further treatment with EDTA to sample ANT180 causes an increase of the Brønsted acid sites population and a reduction of the amount of Lewis acid sites.

The depletion of the total amount of Brønsted acid sites is likely a direct consequence of the destruction of some regions of the zeolite crystals. The enhancement of the acidity after EDTA treatment is most probably a result of the extraction of some EFAl species acting as site-blocking moieties. This behavior agrees well with literature reports [22] and the results presented in chapter 3 (section 3.3.8.3).

Summing up, consistent information was obtained by NH_3-TPD, FTIR in the hydroxyl region and pyridine adsorption in regard to the acid characteristics of the studied

zeolites. AN treatment yields to solids with lower total acidity and increased L/B ratios presumable due to the increment in the amount of some EFAl species. Creation of species of weak acid nature was detected in AN-treated samples. EDTA subsequent treatment showed to enhance the acid properties of the starting zeolite.

Table 4.4. Acidity measurements by pyridine adsorption-desorption monitored by FTIR.

Zeolite		Total (mmol/g)[a]	Medium (mmol/g)[b]	Strong (mmol/g)[c]
HT600	Brønsted (B)	0.41	0.28	0.06
	Lewis (L)	0.39		
	L/B	0.95		
	B_{medium}/B_{total}	0.68		
	B_{strong}/B_{total}	0.15		
ANT120	Brønsted (B)	0.37	0.28	0.08
	Lewis (L)	0.40		
	L/B	1.08		
	B_{medium}/B_{total}	0.76		
	B_{strong}/B_{total}	0.23		
ANT180	Brønsted (B)	0.35	0.28	0.08
	Lewis (L)	0.40		
	L/B	1.14		
	B_{medium}/B_{total}	0.79		
	B_{strong}/B_{total}	0.22		
ANT180-EDTA	Brønsted (B)	0.47	0.37	0.13
	Lewis (L)	0.35		
	L/B	0.75		
	B_{medium}/B_{total}	0.78		
	B_{strong}/B_{total}	0.28		

[a] Total acid sites (after pyridine desorption at 150 °C).

[b] Medium-strength acid sites (after pyridine desorption at 300 °C).

[c] Strong-strength acid sites (after pyridine desorption at 500 °C).

4.3.8. Properties of NiMoP-supported catalysts

The main textural properties and the chemical composition of the hydrocracking catalysts are presented in **Table 4.5**. Textural properties of the catalysts vary in line with the observed trend for the modified zeolites (**Table 4.1**). The Ni/Mo ratio was similar for all catalysts. As in chapter 2 and 3, further characterization by UV-Vis DRS, LRS (Raman) and XPS was performed to the hydrocracking catalysts. The results are included in **Appendix D**. The data indicate only minor differences in regard to the dispersion of the NiMo-oxide components, the metal-support interaction and the sulfidation behavior of these materials.

Table 4.5. Textural properties and chemical compositions of NiMoP-supported catalysts.

Catalyst	Textural properties		Chemical composition			
	S_{BET} (m^2/g)	V_{total} (cm^3/g)	NiO (wt.%)	MoO_3 (wt.%)	$\%P_2O_5$ (wt.%)	Ni/Mo
NiMoP/(HT600 + Alumina)	288	0.30	2.3	14.1	1.9	0.33
NiMoP/(ANT120 + Alumina)	303	0.33	2.5	15.6	1.9	0.31
NiMoP/(ANT180 + Alumina)	316	0.37	2.5	14.2	2.0	0.34
NiMoP/(ANT180-EDTA + Alumina)	355	0.34	2.1	12.2	1.9	0.33

4.3.9. Performance of the hydrocracking catalysts

A progressive deactivation trend was observed for all catalysts and was ascribed to the cumulative poisoning of the acid sites by ammonia coming from the decomposition of nitrogen compounds present in the feed and the progressive formation of coke. Hydrocracking activities of NiMoP-supported catalysts after 80 h on stream are presented in **Table 4.6**.

The NiMoP/(HT600 + Alumina) catalyst is the least active and shows the lowest middle distillate yield. For catalysts based on the ANT120 and ANT180 zeolites, the conversion of the 370 $°C^+$ fraction slightly increases with respect to the one prepared with the HT600 zeolite. Even so, the middle distillates yield is remarkably enhanced for these catalysts. The higher the temperature used in the AN treatment of the zeolite, the higher the middle distillates yield showed by the hydrocracking catalyst. Activity for the catalyst based on the ANT180-EDTA zeolite is significantly increased yielding to higher naphtha yields with respect to the catalyst based on the ANT180 zeolite.

Taking into account that the same procedure was used for loading the (de)hydrogenation function components and that the catalysts contain similar amounts of metals and the same amount of zeolite, the VGO hydrocracking performances shown by the catalysts can be reasonably attributed to the effects of the treatment method on the textural and acid properties of the USY zeolites. Additionally, characterization results for the NiMoP-supported catalysts did not show significant differences in regard to the (de)-hydrogenation function components.

Table 4.6. Hydrocracking activities of NiMoP-supported catalysts.

Catalyst	Conversion of 370 °C$^+$ cut (%)[a]	Yields (wt.%)	
		Middle distillates[b]	Naphtha[c]
NiMoP/(HT600 + Alumina)	45	17	28
NiMoP/(ANT120 + Alumina)	46	21	25
NiMoP/(ANT180 + Alumina)	48	23	26
NiMoP/(ANT180-EDTA + Alumina)	54	22	32

[a] Values reported after 80 h on stream.

[b] Based on the 180-370 °C cut wt.% in the liquid fraction of products.

[c] Based on the IBP-180 °C cut wt.% in the liquid fraction of products. The gas yields were less than 5% in all cases.

Following a general approach, increasing the zeolite mesopore surface area implies better accessibility for the VGO feedstock molecules and, therefore, enhanced activity since more acid sites are expected to become available to participate in the hydrocracking reaction [13]. However, in the present study although the mesopore surface area was more than doubled and tripled for the zeolites ANT120 and ANT180, respectively, the increase in VGO hydrocracking activity was relatively small. In fact, AN treatment slightly decreased the total amount of Brønsted acid sites. These observations lead to state that the accessibility to the VGO compounds was not extensively enhanced with the AN treatments. One possible reason to explain this behavior is that the extraframework silicon and aluminum material resulting from the destruction of parts of the zeolite crystals during steaming and increased with AN treatment obstruct the micro and mesopore system. Only when the AN-treated zeolites are subjected to further treatment with EDTA the benefit in activity of increasing mesoporosity is actually notorious. This additional treatment with EDTA is able to unblock the mesopore and micropore system due to the removal of polymerized EFAl species. The positive effect of EDTA treatment on accessibility of USY zeolite has been recently discussed [14]. In the present study, this further EDTA treatment step seems necessary to exploit the enhanced mesoporosity developed by the AN treatment in the hydrocracking of the selected feedstock.

The mechanism of creation of mesoporosity in USY zeolites by AN treatment has not been studied. Only some notions are known about the effect of parameters such as

temperature, time and pH on the development of mesopore volume during AN treatment [32]. This treatment resembles some features of others modification processes, such as steaming combined with mild acid leaching or desilication in terms of the preservation of the framework aluminum content and acidity [33]. As in desilication, ammonium nitrate solutions can cause hydrolysis of ≡Si–O–Si≡ bonds yielding to the formation of small pores even at lower temperature and AN concentration than those used in the present study [34]. Since hydrocracking activity results point out that the majority of the mesopores created with AN treatment are not effectively reachable by the VGO compounds, intra-crystalline cavity-like mesopores are therefore likely to be present in AN-treated zeolites. According to de Jong et al. [13], desilication of USY zeolites with NaOH tends to create sponge-like small mesopores of 3 nm in average. In the present work, the pore size distributions of the zeolite treated at 180 ºC by AN shows mesopores of sizes around 8 nm. Thus, desilication treatment by NaOH and AN treatment differs in the sizes of the mesopores created. Qin et al. [33] observed the development of crater-like mesopores also at ca. 8 nm in NH_4NaY zeolites modified by $(NH_4)_2SiF_6$ resulting from intensive out-of-control surface dealumination. However, it is unlikely that the same kind of mesopores are created by AN since both the nature and size of $(NH_4)_2SiF_6$ are different. AN treatment also differs to desilication, acid leaching and other chemical modification methods in that the extraframework material created during the development of mesoporosity remains deposited in the pore system. Additionally, no migration of extraframework species takes place since the surface Si/Al ratio remains fairly unaltered. Recently, Aelst et al. [35] have reported the development of mesoestructured USY zeolites by NH_4OH treatment followed by thermal treatment. They proposed that the process at the atomic level involves the transformation of regions of crystalline zeolite into mesopores surrounded by a dense amorphous phase. Although the modifications processes are expected to proceed through different mechanisms, some similarities between the NH_4OH and AN treatments appear to exist. The possible amorphization at the surface of mesopores of the zeolites by AN treatment would explain the creation of EFAl species observed by ^{27}Al MAS NMR (**Figure 4.6**), the formation of weak acid species indicated by NH_3-TPD curves (**Figure 4.6**), the depletion in total Brønsted acid sites (**Table 4.6**), the development of external silanol groups attached to extraframework silica-rich species indicated by FTIR (**Figure 4.8**) and the changes in morphology suggested by HRTEM

images (**Figure 4.4**). Additionally, having in mind that the subsequent EDTA treatment to the AN-treated sample restores the microporosity to the value of the parent steam treated zeolite, the creation of dense layer of amorphous material blocking the micropore mouths would also explain the depletion of micropore volume caused by AN treatment (**Table 4.1**). The presence of an amorphous phase at the micropore mouths and the mesopores in AN-treated samples seems therefore reasonable.

The existence of both condensed EFAl species at the external surface of the zeolite crystals already formed during the steaming steps and an new amorphous phase at the mesopores created with the AN-treatment could also impact the selectivity profiles of the hydrocracking catalysts. In fact, this amorphous phase could limit the extent of secondary cracking of the VGO feedstock molecules resulting in higher middle distillates yields. Therefore, the observed selectivity trend for the set of catalysts based on the AN-treated zeolites could also be explained by the progressive amorphization as a result of mesopore development. On the other hand, since the further EDTA treatment results in the release of some strong-strength Brønsted acid sites (**Table 4.4**), it seems likely that the increased selectivity to naphtha observed in the catalysts based on the ANT180-EDTA zeolite is due to this behavior. In general terms, the treatment conditions used to modify the zeolites in the present study derive in solids with moderate middle distillate selectivity in the hydrocracking of the selected feedstock. Certainly, this feature and the observed deactivation trend could be enhanced by better adjusting the ratio of (de)-hydrogenation over cracking function. Nevertheless, a modification strategy that combines AN and EDTA treatments seems suitable to develop USY zeolites with enhanced activity and middle distillates selectivity in the hydrocracking of real feedstocks.

4.4. CONCLUSIONS

Chemically modified USY zeolites were obtained by AN treatment under hydrothermal conditions. Further treatment with Na_2H_2-EDTA to a selected AN-treated zeolite was also performed. AN treatment considerably enhanced the mesopore volume of parent steam-treated zeolite. AN treatment also caused the creation of extraframework species of weak acid nature. NiMoP based hydrocracking catalysts were prepared using the modified zeolites and evaluated in the hydrocracking of a heavy VGO. Hydrocracking

activity results of the NiMoP supported catalysts indicate that although AN treatment significantly develops mesoporosity, this sole treatment was not effective to enhance the accessibility of VGO compounds to the acid sites. This behavior was ascribed to deficient connection of the created mesopores with the external surface of the zeolite crystals. However, the catalysts based on AN treated zeolites showed significantly higher middle distillates yields than the one based on the steam-treated zeolite. The creation of an amorphous phase at the mesopore surface was suggested to support this observation. A mild EDTA treatment to an AN-treated zeolite showed to be beneficial to improve hydrocracking activity. This was attributed to the enhanced access to acid sites after the removal of polymerized EFAl species. Finally, a modification strategy that combines AN and EDTA treatments is proposed to design USY-based catalysts with enhanced activity and middle distillates selectivity in the hydrocracking of real feedstock.

REFERENCES

[1] E. Benazzi, L. Leite, N. Marchal-George, H. Toulhoat, P. Raybaud, Journal of Catalysis 217 (2003) 376–387.

[2] S. Van Donk, A.H. Janssen, J.H. Bitter, K.P. de Jong, Catalysis Reviews 45 (2003) 297-319.

[3] D. Verboekend, G. Vilé, J. Pérez-Ramírez, Advanced Functional Materials 22 (2012) 916-928.

[4] K. Li, J. Valla, J. Garcia-Martinez, ChemCatChem 6 (2014) 46-66.

[5] K. Na, M. Choi, R. Ryoo, Microporous and Mesoporous Materials 166 (2013) 3-19.

[6] R. Chal, C. Gérardin, M. Bulut, S. van Donk, ChemCatChem 3 (2011) 67-81.

[7] X.-w. Chang, L.-f. He, H.-n. Liang, X.-m. Liu, Z.-f. Yan, Catalysis Today 158 (2010) 198-204.

[8] M.-C. Silaghi, C. Chizallet, P. Raybaud, Microporous and Mesoporous Materials 191 (2014) 82-96.

[9] Q. Cui, Y. Zhou, Q. Wei, X. Tao, G. Yu, Y. Wang, J. Yang, Energy & Fuels 26 (2012) 4664-4670.

[10] K. Sato, Y. Nishimura, K. Honna, N. Matsubayashi, H. Shimada, Journal of Catalysis 200 (2001) 288–297.

[11] A.V. Abramova, E.V. Slivinskii, Y.Y. Goldfarb, A.A. Panin, E.A. Kulikova, G.A. Kliger, Kinetics and Catalysis 46 (2005) 758–769.

[12] H. Shimada, K. Sato, K. Honna, T. Enomoto, N. Ohshio, Catalysis Today 141 (2009) 43–51.

[13] K.P. de Jong, J. Zečević, H. Friedrich, P.E. De Jongh, M. Bulut, S. Van Donk, R. Kenmogne, A. Finiels, V. Hulea, F. Fajula, Angewandte Chemie 122 (2010) 10272-10276.

[14] J.L. Agudelo, B. Mezari, E.J.M. Hensen, S.A. Giraldo, L.J. Hoyos, Applied Catalysis A: General 488 (2014) 219-230.

[15] D.A. Cooper, T.W. Hastings, E.P. Hertzenberg, Stabilized zeolite having structure of zeolite y and mesopore volume contained in mesopores of specified diameter, US Patent 5,601,798, 1997.

[16] C.B.a.L.B. McCusker, Database of Zeolite Structures, The International Zeolite Asociation (IZA), http://www.iza-structure.org/databases/, 2015.

[17] A. Janssen, A. Koster, K. De Jong, The Journal of Physical Chemistry B 106 (2002) 11905-11909.

[18] R. Beyerlein, C. Choi-Feng, J. Hall, B. Huggins, G. Ray, Topics in Catalysis 4 (1997) 27-42.

[19] A.N. van Laak, S.L. Sagala, J. Zečević, H. Friedrich, P.E. de Jongh, K.P. de Jong, Journal of Catalysis 276 (2010) 170-180.

[20] J. Van Aelst, M. Haouas, E. Gobechiya, K. Houthoofd, A. Philippaerts, S.P. Sree, C.E. Kirschhock, P. Jacobs, J.A. Martens, B.F. Sels, The Journal of Physical Chemistry C 118 (2014) 22573-22582.

[21] K. Tarach, K. Góra-Marek, J. Tekla, K. Brylewska, J. Datka, K. Mlekodaj, W. Makowski, M. Igualada López, J. Martínez Triguero, F. Rey, Journal of Catalysis 312 (2014) 46-57.

[22] N.P. Rhodes, R. Rudham, Journal of the Chemical Society, Faraday Transactions 89 (1993) 2551-2557.

[23] J.C. Groen, J.A. Moulijn, J. Pérez-Ramírez, Journal of Materials Chemistry 16 (2006) 2121-2131.

[24] L. Aouali, J. Teanjean, A. Dereigne, P. Tougne, D. Delafosse, Zeolites 8 (1988) 517-522.

[25] T. Fleisch, B. Meyers, G. Ray, J. Hall, C. Marshall, Journal of Catalysis 99 (1986) 117-125.

[26] M.J. Remy, D. Stanica, G. Poncelet, E.J.P. Feijen, P.J. Grobet, J.A. Martens, a.P.A. Jacobs, J. Phys. Chem. 100 (1996) 12440-12447.

[27] A. Gola, B. Rebours, E. Milazzo, J. Lynch, E. Benazzi, S.L.L. Delevoye, C. Fernandez, Microporous and Mesoporous Materials 40 (2000) 73-83.

[28] B. Wouters, T.-H. Chen, P. Grobet, Journal of the American Chemical Society 120 (1998) 11419-11425.

[29] N. Katada, Y. Kageyama, K. Takahara, T. Kanai, H.A.B. , M. Niwa, Journal of Molecular Catalysis A: Chemical 211 (2004) 119–130.

[30] A. Janin, M. Maache, J. Lavalley, J. Joly, F. Raatz, N. Szydlowski, Zeolites 11 (1991) 391-396.

[31] I. Halasz, M. Agarwal, B. Marcus, W.E. Cormier, Microporous and mesoporous materials 84 (2005) 318-331.

[32] D.A. Cooper, T.W. Hastings, E.P. Hertzenberg, Stabilized zeolite having structure of zeolite y and mesopore volume contained in mesopores of specified diameter, Google Patents, 1997.

[33] Z. Qin, B. Shen, X. Gao, F. Lin, B. Wang, C. Xu, Journal of Catalysis 278 (2011) 266-275.

[34] E. Sacaliuc-Parvulescu, H. Friedrich, R. Palkovits, B.M. Weckhuysen, T.A. Nijhuis, Journal of catalysis 259 (2008) 43-53.

[35] J. Van Aelst, M. Haouas, E. Gobechiya, K. Houthoofd, A. Philippaerts, S.P. Sree, C.E. Kirschhock, P.A. Jacobs, J.A. Martens, B.F. Sels, The Journal of Physical Chemistry C (2014).

5. GENERAL DISCUSSION

The previous chapters showed several ways in which it is possible to adjust the activity and selectivity of a hydrocracking catalyst by using modified USY zeolites. Hydrothermal treatment was coupled to three chemical treatments to prepare modified USY zeolites of different characteristics. Chapter 2 dealt with hydrothermal treatment coupled to mild acid leaching with HCl. In chapter 3, hydrothermal treatment was coupled to Na_2H_2-EDTA leaching. Chapter 4 dealt with hydrothermal treatment coupled to ammonium nitrate (AN) treatments. The combination of AN and EDTA treatments was also evaluated. In the present chapter the main effects of each method on the properties of the USY zeolites are summarized and the impacts of the treatments on the VGO hydrocracking activity and middle distillates yield are compared.

First, hydrothermal treatment showed to be an efficient method to dealuminate the zeolite in a controlled way by adjusting the treatment temperature. VGO hydrocracking activity could be modulated by this treatment. Hydrothermal treatment mainly alters the total number of Brønsted acid sites of the zeolite structure. Besides, this treatment also influences the development of secondary pore system. In addition, the treatment temperature has a direct impact on the type and amount of EFAl formed. All these phenomena had a significant effect on the performance of the zeolites as hydrocracking catalyst components. According to literature, the dealumination step of the USY zeolite can also be made by direct chemical treatments with compounds such as $SiCl_4$, $(NH_4)_2SiF_6$, H_4EDTA, oxalic acid, etc [1-6]. However, these procedures guarantee neither the development of a secondary system of pores with similar characteristics to those obtained by hydrothermal treatment, nor the formation of certain EFAl species that can act synergistically in the cracking catalysis. In fact, some of these treatments lead to solids with poor cracking activity [7]. Therefore, hydrothermal treatment seems to be the most proper initial process for obtaining zeolites to be used as components of hydrocracking catalysts. Some literature studies have also used zeolites obtained by hydrothermal treatment coupled to chemical treatments [8-11]. Although it has been shown that highly dealuminated zeolites have good selectivity to middle distillates, its cracking activity is significantly depleted. It was evidenced that performing the hydrothermal treatment step at 700 ºC induces a drastic depletion of the number of

Brønsted acid sites. This would yield to the need to operate at higher process temperatures, which is disadvantageous. Consequently, for the studies of chapter 3 and 4 moderately dealuminated zeolites were prepared to avoid critical deterioration of their cracking activity. Nevertheless, the possible use of a moderately dealuminated zeolites with improved properties by subsequent chemical treatments as hydrocracking catalyst components, would be determined considering the fulfillment of the fixed levels of activity, stability and middle distillates yield.

It was shown in this work that EFAl formed during hydrothermal treatment have both positive and negative effects on the hydrocracking catalytic activity. The EFAl species that agglomerate on the surface of the zeolite crystals and the mesopores adversely affect the catalytic activity by limiting the accessibility of the molecules present in the VGO feedstock to the zeolite acid sites. Therefore, a step of partial removal of EFAl seems necessary to restore the accessibility and thus exploit the potential catalytic activity of the zeolite. This positive effect of partial removal of EFAl was evidenced with both acid leaching and EDTA treatment. On the other hand, the presence of some EFAl species showed to be essential to maintain the catalyst activity. In chapter 3, it was shown that the phasing out of EFAl causes a gradual decrease in activity. When severe processing conditions are used in EDTA treatment, EFAl species apparently involved in cracking catalysis are removed. Consequently, the hydrocracking behavior of the catalysts based on EDTA-treated zeolites led us to conclude that developing supports with increased mesoporosity and strong acid character does not assure higher hydrocracking activity of a real feedstock.

In terms of middle distillates yield, the removal of EFAl is detrimental as it results in the exposure of strong acid sites, which tend to the production of more naphtha. Additionally, in chapter 4 it was shown that the presence of some EFAl species in the zeolite formed by ammonium nitrate treatment appeared to favor the yield to middle distillates during VGO hydrocracking. Since the exposure of strong acid sites to the VGO compounds favors the production of naphtha, a good balance between weak and strong acid sites at the surface and the mesopores of the zeolite seems necessary. Ammonium nitrate treatment seems to be the most suitable method to achieve that acidity balance.

In general terms, it was difficult to associate the changes in the zeolite properties caused by each chemical treatment to the activity and selectivity in VGO hydrocracking. The

complexity of setting which property of the zeolite mainly determines the hydrocracking performance emerges from the fact that various phenomena occur simultaneously during each chemical treatment. For instance, the EFAl extraction by either EDTA treatment or acid leaching have significant effect on both acid sites strength and density, but also on the textural properties of the zeolites. The size and nature of the leaching agent and the strength of the chemical treatment also have effect on the homogeneity of the EFAl removal process. For EFAl extraction with EDTA diffusional limitations are present and, therefore, the process preferentially occurs on the external surface of the zeolite and mesopores at mild treatment conditions. In contrast, for treatment with HCl, the extraction of EFAl is expected to be more homogeneous throughout the zeolite crystal. The EFAl leaching agents also differ in the kind of species they mostly remove. It was observed that under the experimental conditions used for EDTA treatment, this agent removes EFAl species in penta and hexa-coordinated environments. Meanwhile, the mild acid leaching mainly extracted EFAl species in hexa-coordinated environment (octahedral aluminum). Acid leaching also caused additional dealumination of the zeolite structure. In contrast, EDTA proved to be a selective agent for the removal of EFAl without significantly altering the aluminum content of the framework. These results remarked the importance of the right selection of the leaching agent and of establishing proper treatment conditions depending on the characteristics of the parent materials, for instance the nature of the EFAl species and their degree of polymerization. For the case of ammonium nitrate treatment the phenomena that occur are significantly different from those observed with acid leaching or EDTA treatment. This treatment method showed to be effective to develop mesoporosity in the zeolites. Additionally, the characterization data of the AN-treated zeolites also showed that this procedure induces the formation of new EFAl species due to the destruction of certain regions of the zeolite structure. The activity data suggested that a preferential amorphization occurs at the outer surface of the zeolite crystal and its mesopores. The occurrence of this phenomenon would explain the limited increase in VGO hydrocracking activity and the higher middle distillates yield.

In short, in spite of the difficulty in attributing the changes in activity and selectivity exclusively to factors such as the degree of mesoporosity, total acidity or amount of EFAl, some key findings emerged clearly. For example, that the presence of certain EFAl species is linked to the activity and selectivity shown by the hydrocracking

catalysts and that higher mesoporosity does not imply better hydrocracking performance.

Having synthesized the main features of the chemical treatment used in this study, it follows to set up what could be the most effective method to enhance the VGO hydrocracking activity and middle distillates yield taking as the references the catalysts prepared from the hydrothermally treated zeolites. **Figure 5.1** shows the dependence of middle distillates yield on VGO conversion for the catalysts based on the modified zeolites of the present study. Clearly, the most active catalysts are those prepared from the EDTA-treated zeolites. The ones that produce more middle distillates are those based on AN-treated zeolites. However, the comparison among catalysts of chapter 2 and catalysts of chapters 3 and 4 is restricted since they were tested under different temperature and severity conditions.

Figure 5.1. Dependence of middle distillates yield on VGO hydrocracking conversion for the catalysts based on the modified zeolites of the present study. Dashed lines between points are helps to the eye (not a tendency line).

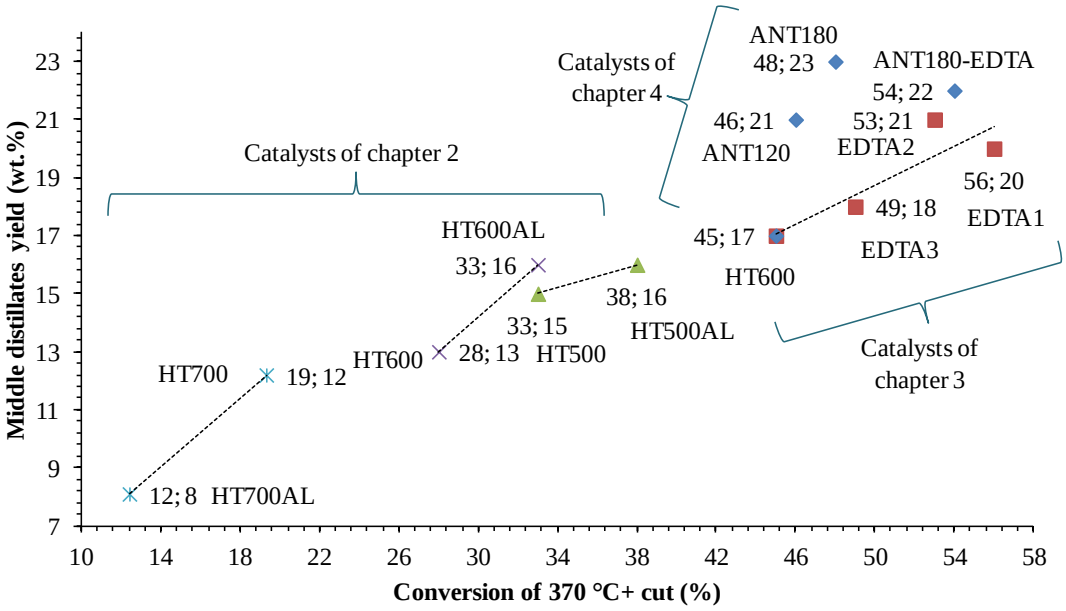

Table 5.1 better summarizes the results of activity and yield to middle distillates and naphtha. For catalysts based on chemically-treated zeolites, **Table 5.1** also includes the changes in conversion and yields relative to the catalyst based on the corresponding hydrothermally treated zeolite. The comparison in terms of relative change of activity

and yield among all catalysts is then acceptable. It is observed that the largest increases in conversion are shown by the catalysts based on EDTA-treated zeolites. The increase in activity induced by this agent is greater when moderate treatment conditions are used. However, the increase in activity is mainly reflected in higher naphtha yield. Catalysts based on zeolites leached with HCl show an intermediate increase in conversion and yields to middle distillates and naphtha. Meanwhile, for the catalysts based on ammonium nitrate treated zeolites the changes in activity are smaller, but the middle distillate yield increments are higher than those observed with the other catalysts. These catalysts are the only ones that induce a decrease in naphtha yield at a similar conversion level. Further treatment with EDTA to the AN-treated zeolite (ANT180) leads to a more active catalyst. However, as for the catalyst based on the EDTA1 zeolite, the increased activity is reflected in higher production of naphtha. Even so, the detriment in middle distillates yield is small.

Table 5.1. VGO hydrocracking activity results for the catalysts based of the modified zeolites of the present study.

Catalyst	Conversion of 370 °C^{+} cut (%)	Middle distillates yield (wt.%)	Naphtha yield (wt.%)	Δ conversion (%)	Δ M.D. yield (%)	Δ Naphtha yield (%)
NiMoP/(HT500 + Alumina)	33	15	19	base	base	base
NiMoP/(HT500AL + Alumina)	38	16	22	+5	+1	+3
NiMoP/(HT600 + Alumina)	28	13	15	base	base	base
NiMoP/(HT600AL + Alumina)	33	16	17	+5	+3	+2
NiMoP/(HT700 + Alumina)	19	12	8	base	base	base
NiMoP/(HT700AL + Alumina)	12	8	4	-7	-4	-4
NiMoP/(HT600 + Alumina)	45	17	28	base	base	base
NiMoP/(EDTA1 + Alumina)	56	20	36	+11	+3	+8
NiMoP/(EDTA2 + Alumina)	53	21	32	+8	+4	+4
NiMoP/(EDTA3 + Alumina)	49	18	31	+4	+1	+3
NiMoP/(ANT120 + Alumina)	46	21	25	+1	+4	-3
NiMoP/(ANT180 + Alumina)	48	23	26	+3 (base)	+6 (base)	-2 (base)
NiMoP/(ANT180-EDTA + Alumina)	54	22	32	+9 (+6)	+5 (-1)	+4 (+6)

Overall, the data suggest that for increasing the activity of a hydrothermally treated zeolite, the most effective chemical treatment would be mild EDTA leaching. Meanwhile, to increase the middle distillate yield the most effective method appears to be ammonium nitrate treatment. Finally, to increase both activity and middle distillates yield, the combined treatment with ammonium nitrate and EDTA seems appropriate. Evidently, the above statements are restricted by the experimental range of conditions used for each chemical treatment. A fairer comparison of the results would be done by normalizing them according to, for example, the strength of treatment. However, due to the very different nature of the agents and the diverse phenomena observed during each treatment, that kind of normalization is not plausible. Even so, the hydrocracking performance trends indicate that the catalysts studied here are likely susceptible to further improvements by adjusting the zeolite treatment conditions. For example, although it was observed that acid leaching yield to smaller increments in activity than EDTA treatment, it seems reasonable to expect that adjusting the severity of the treatment, similar enhancements in activity by both methods could be obtained. Analogously, for the case of the catalyst based on ANT180-EDTA zeolite, it seems possible to obtain an even more active and selective catalyst to middle distillates by adjusting the severity of the treatments. Nevertheless, the convenience analysis of the treatment strategies for developing zeolites with improved properties for the use as catalyst components should also consider other factors such as the level of deterioration of the zeolite, the complexity/flexibility of the method, the cost of reagents, the needed infrastructure and the production of harmful by-products.

The hydrocracking catalysts of the present thesis are also susceptible to improvements in other properties such as the balance between the hydrogenating and cracking functions. As mentioned before, the product distribution is also linked to the efficiency of the (de)hydrogenation function relative to the acid function. Thus, when applying supports with enhanced acid strength, it is necessary to provide a stronger (de)hydrogenation function to balance this acidity. Then, it seems possible to overcome the observed deactivation tendency of the catalysts based on EDTA-treated and AN-treated zeolites and to increase their middle distillate yields by optimizing the zeolite and metals content. All in all, the selection of any strategy to get hydrocracking catalysts with enhanced activity and middle distillate selectivity would involve a whole techno-economical study of the different alternatives.

REFERENCES

[1] A.V. Abramova, E.V. Slivinskii, Y.Y. Goldfarb, A.A. Panin, E.A. Kulikova, G.A. Kliger, Kinetics and Catalysis 46 (2005) 758–769.

[2] X.-w. Chang, L.-f. He, H.-n. Liang, X.-m. Liu, Z.-f. Yan, Catalysis Today 158 (2010) 198-204.

[3] D. Verboekend, G. Vilé, J. Pérez-Ramírez, Advanced Functional Materials 22 (2012) 916-928.

[4] C.S. Triantafillidis, A.G. Vlessidis, N.P. Evmiridis, Ind. Eng. Chem. Res. 39 (2000) 307-319.

[5] H.K. Beyer, Molecular Sieves,Vol. 3, Springer-Verlag, Berlin, 2002.

[6] S. Van Donk, A.H. Janssen, J.H. Bitter, K.P. de Jong, Catalysis Reviews 45 (2003) 297-319.

[7] R. Beyerlein, G. McVicker, L. Yacullo, J. Ziemiak, The Journal of Physical Chemistry 92 (1988) 1967-1970.

[8] R. Bezman, Catalysis Today 13 (1992) 143-156.

[9] K.P. de Jong, J. Zečević, H. Friedrich, P.E. De Jongh, M. Bulut, S. Van Donk, R. Kenmogne, A. Finiels, V. Hulea, F. Fajula, Angewandte Chemie 122 (2010) 10272-10276.

[10] J. Francis, E. Guillon, N. Bats, C. Pichon, A. Corma, L. Simon, Applied Catalysis A: General 409 (2011) 140-147.

[11] P. Dik, O. Klimov, G. Koryakina, K. Leonova, V.Y. Pereyma, S. Budukva, E.Y. Gerasimov, A. Noskov, Catalysis Today 220 (2014) 124-132.

6. GENERAL CONCLUSIONS

This thesis attempted to contribute to the better understanding of the relationship between USY properties and VGO hydrocracking reactivity. Systematic hydrocracking studies with a real feedstock were performed with catalysts based on modified USY zeolites obtained by three selected chemical treatments. The main insights that were obtained with the present work are:

- A direct association exists between the degree of framework dealumination and hydrocracking activity for the catalysts based on steam treated zeolites. The lower the framework aluminum content, the lower the hydrocracking catalytic activity.
- Acid leaching and EDTA treatment showed to be beneficial to improve the hydrocracking activity because of the enhanced access to acid sites after the removal of polymerized EFAl species. Specific to the conversion of heavy feeds is that accessibility of the mesopores and availability of acid sites on the external surface of the zeolite crystals are key to good hydrocracking performance.
- The presence of certain EFAl species for the hydrocracking of real feedstocks is necessary to achieve high catalytic activity. The positive/negative effect observed in VGO hydrocracking for the catalysts based on the modified zeolites depends on the conditions used during the EFAl removal step.
- The severe removal of EFAl by either acid leaching or EDTA treatment is detrimental to middle distillates production as it results in the exposure of strong Brønsted acid sites, which tend to overcrack the feedstock.
- Ammonium nitrate treatment can be suited to obtain USY zeolites with improved properties that induce increased middle distillates yields. However, this treatment was not efficient to enhance the accessibility of VGO compounds to the acid sites.
- Even with zeolites with increased mesoporosity and stronger acid character, higher hydrocracking activity of a real feedstock is not guaranteed.

- The combination of different treatment methods can result in USY-based catalysts with enhanced activity and middle distillates selectivity in the hydrocracking of real feedstocks.

LIST OF PUBLICATIONS

In peer–reviewed journals:

- On the effect of EDTA treatment on the acidic properties of USYzeolite and its performance in vacuum gas oil hydrocracking. J.L. Agudelo, B. Mezari, E.J.M. Hensen, S.A. Giraldo, L.J. Hoyos. Applied Catalysis A: General 488 (2014) 219–230.
- Influence of steam–calcination and acid leaching treatment on the VGO hydrocracking performance of faujasite zeolite. J.L. Agudelo, E.J.M. Hensen, S.A. Giraldo, L.J. Hoyos. Fuel Processing Technology 133 (2015) 89–96.

Presentations in scientific events:

- Oral
  - Effect of USY zeolite modifications on activity and middle distillates selectivity in the hydrocracking of a heavy feedstock. J.L. Agudelo, S.A. Giraldo, L.J. Hoyos. 244th ACS National Meeting & Exposition, August 19 − 23, 2012, Philadelphia (PA) – USA.
  - Hydrocracking of a Heavy Feedstock Using Modified USY Zeolite–Based Catalysts, J.L. Agudelo, E.J.M. Hensen, S.A. Giraldo, L.J. Hoyos. The American Institute of Chemical Engineers (AIChE) Annual Meeting, November 3 – 8, 2013, San Francisco (CA) – USA.
  - *Evaluación de la incertidumbre asociada al refinamiento por Rietveld para calculo de tamaño unidad de celda en zeolitas USY*. J.L. Agudelo, A.M. Careño, L.J. Hoyos, S.A. Giraldo, J.A. Henao. *XIII Seminario latinoamericano de análisis por técnicas de difracción de rayos X*, November 18 – 23, 2012, Santa Marta – Colombia.

- Poster
  - Effect of USY zeolite modifications on activity and middle distillates selectivity in the hydrocracking of a heavy feedstock. J.L. Agudelo, S.A.

Giraldo, L.J. Hoyos. 244th ACS National Meeting & Exposition, Sci-Mix session, August 19 − 23, 2012, Philadelphia (PA) – USA.

- *Efecto del tratamiento hidrotérmico y del lavado ácido sobre las características de acidez y textura de la zeolita Y*. J.L. Agudelo, S.A. Giraldo, A.Centeno, L.J. Hoyos. *VII simposio colombiano de catálisis*. September 29 – October 1, 2011, Cartagena – Colombia.

APPENDIX A.

DESCRIPTION OF THE CHARACTERIZATION TECHNIQUES

A.1. X-RAY DIFFRACTION ANALYSIS (XRD)

X-ray diffraction is one of the oldest and most frequently applied techniques in catalyst characterization. X-ray diffraction is a nondestructive technique that is widely used for structure determination of crystalline materials. The X-ray diffraction pattern may be used to provide information about the electronic distribution of atoms throughout the zeolites structure. The diffraction of the X-rays from a given solid crystal planes creates a scattering pattern, which is specific of the periodic arrangement of regular arrays of atoms in that solid. Each type of crystalline solid has unique characteristic X-ray diffraction pattern, which is typically utilized as a "fingerprint" for its identification and classification [1-3]. The theory of XRD is provided in specialized books [4, 5].

The XRD pattern of a powdered sample is measured with a stationary X-ray source (usually Cu Kα) and a movable detector, which scans the intensity of the diffracted radiation as a function of the angle 2θ between the incoming and the diffracted beams. When working with powdered samples, an image of diffraction lines occurs because a small fraction of the powder particles will be oriented such that by chance a certain crystal plane is at the correct angle θ with the incident beam for constructive interference.

The basis for X-ray diffraction is the property of electromagnetic radiation. The formula of Bragg's law is applied to interpret the XRD-data:

$$\lambda = 2dSin\theta_{hkl}$$

Where, λ is the wavelength of the incident X-ray beam, θ_{hkl} is the scattering or Bragg angle between the incident X-ray beam and the crystal planes, and d is the spacing between parallel planes in the atomic lattice. The *hkl* values have to be assigned to each of the reflections to determine the size and shape of the unit cell. The indices *hkl* of a plane in the crystal system are also called Miller-Bravais indices. The peak position 2θ can be calculated by using the following expression:

$$\theta_{hkl} = arcSin(\lambda/2d_{hkl})$$

For a cubic unit cell such as zeolite Y the relationship between the *hkl*, *d*-values and the unit cell parameters *a*, *b*, *c*, α, β and γ can be derived from the unit cell parameters in a straightforward manner, according to the following crystal data for zeolite Y:

1- The dimensions: a = b = c.

2- The angles: alpha (α) = beta (β) = gamma (γ) = 90°.

Thus,

$$d_{hkl} = \frac{a_0}{\sqrt{N}}$$

Where,

$$\sqrt{N} = \sqrt{h^2 + k^2 + l^2}$$

And a_0 is the lattice parameter "dimension of unit cell". For crystals with cubic symmetry, the size of unit cell can be determined from the angular positions of the reflections. Therefore,

$$a_0 = \lambda \sqrt{h^2 + k^2 + l^2}/2 \sin \theta_{hkl}$$

Because the A1-O bond length is larger than the Si-O bond length this lattice constant a_0 will increase with increasing the framework A1 content of the zeolite.

The peak width β in radians (often measured as full width at half maximum, FWHM) is inversely proportional to the crystallite size L_{hkl}. This is expressed by the Scherrer equation:

$$L_{hkl} = \frac{\lambda}{\beta cos\theta_{hkl}}$$

Figure A.1 indicates the main features of a XRD pattern and the information that could be derived from its analysis. A 2θ range of 3° to 50° is usually adequate to cover the most important regions of the XRD pattern, and each peak represents at least the one diffraction. The XRD diffraction of any sample must occur at the same peak position for the standard sample in order to identify the structure unit cell dimensions.

The relative intensities of the peaks (I_{rel}) are related to the level of sample crystallization, and are determined by the type and position of all atoms in the unit cell. In other words, changing just one atom e.g. by ion exchange, will influence the intensities of all reflections.

The widths of the peaks are related to the size of crystallite, i.e. they can give an indication of the crystalline quality of the sample.

The background of a powder pattern can also give an indication about the amorphous materials, whether they are present in the sample or not. As a rule, a highly crystallized zeolite samples must have quite a flat baseline.

Figure A.1. The major features of the XRD pattern and the information that could be derived from its analysis.

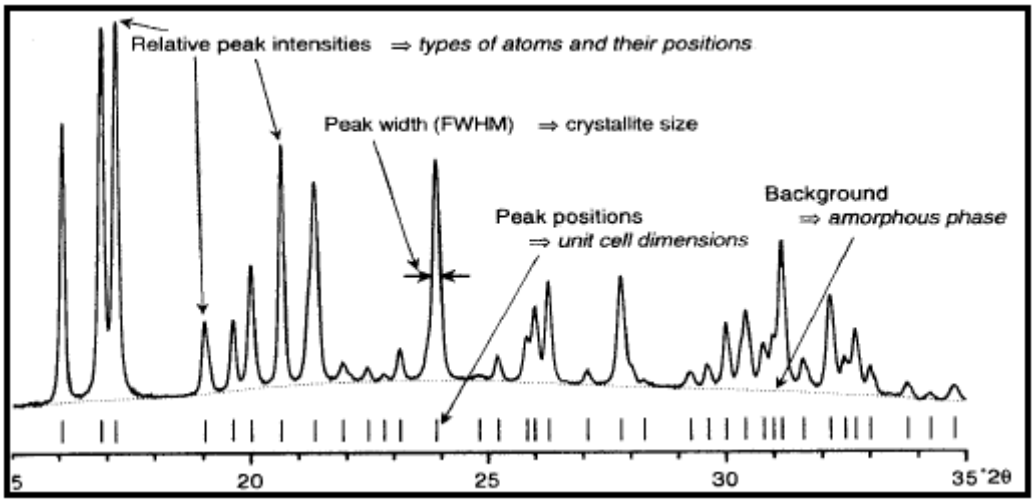

A.2. MAGIC ANGLE SPINNING NUCLEAR MAGNETIC RESONANCE (MAS NMR) ANALYSIS

High resolution solid-state NMR, principally ^{29}Si NMR and ^{27}Al NMR, have been employed to investigate the framework of zeolites [2]. NMR-technique is used in zeolite science to provide information about the structural environment (i.e. chemical surrounding) of an atomic nucleus present within the zeolite framework and/or non-framework, which cannot be obtained by using X-ray diffraction [1, 3].

The technique is based on the principle that nuclei in a magnetic field absorb energy from electromagnetic (EM) pulses and then radiate this energy at a specific resonance frequency, which is collected as signals [6]. Thus specific quantum mechanical magnetic properties of an atomic nucleus can be obtained, and given by the NMR spectrum. The atomic nuclei of materials spin under the influence of an external alternating magnetic field (B_0) inside the NMR equipment. Diminishing the dipolar interaction between the magnetic moments of certain nucleus and other neighboring nuclei together with reducing the chemical shift anisotropy (CSA) – that is related to the electronic charge distribution around the resonance nucleus, can only be achieved by

employing the magic angle spinning (MAS) technique. Practically, this spinning magnetic technique can fully remove or at least significantly reduce the line broadening interactions, and thereby high resolution NMR spectra of solids with perfect separate resonance frequency lines for the structural environment of nuclei can be acquired. Magic angle rotation of the sample occurs between 54°44′ – 54°74′, with respect to the direction of (B_0) [3].

The chemical shift (δ) is one of the most important parameter in the NMR spectra, which is a dimensionless number and typically quoted in parts per million (ppm). It can provide useful information on the type and number of neighboring atoms and the bonding geometry. In order to get the correct magnitude of the δ, the resonance frequency of the sample nucleus is measured relative to that for a certain nucleus in a standard chemical. Therefore, external reference material as a chemical shift standard may be used to set up the NMR machine prior to run the experiment. The most common references used with liquid and solid state NMR are: tetramethylsilane, $Si(CH_3)_4$ and aluminum nitrate, $Al(NO_3)_3 \cdot 9H_2O$ (aqueous).

The three most common atoms within the zeolite framework are silicon, aluminum and oxygen, which can be measured through their naturally occurring isotopes ^{29}Si, ^{27}Al, and ^{17}O, respectively. The ^{29}Si and ^{27}Al nuclei are normally used to study the aluminosilicate framework of the zeolites, and generally the ^{27}Al NMR spectrum is much simpler than ^{29}Si NMR spectrum - as the AlOAl linkages are forbidden (Lowenstein's rule) and it is always utilized to follow the localization of Al species within the zeolite structure.

The ^{29}Si MAS NMR-spectra are generally used to determine the distribution of silicon species in the zeolite framework. The classification of the silicon peaks is illustrated in **Figure A.2**. This spectrum ordinarily consisted of one to five peaks as there are five possible environments of Si(nAl) units in the framework of zeolite. As a rule, decreasing the number of Al-atoms (n) leads to an increase in the intensities of Si peaks at the right side of the spectrum. Conversely, the peaks are systematically shifted to low field (i.e. present less negative δ-values by raising their intensities in the left side of spectrum), if Al atoms replace one or more Si atoms.

The equation based on the ^{29}Si NMR spectrum to determined the quantitative molar ratio of framework tetrahedral Si and Al in zeolite $(Si/Al)_{framework}$ was presented in section 2.2.3.4.

Figure A.2. ^{29}Si MAS NMR spectrum for a typical zeolite [3].

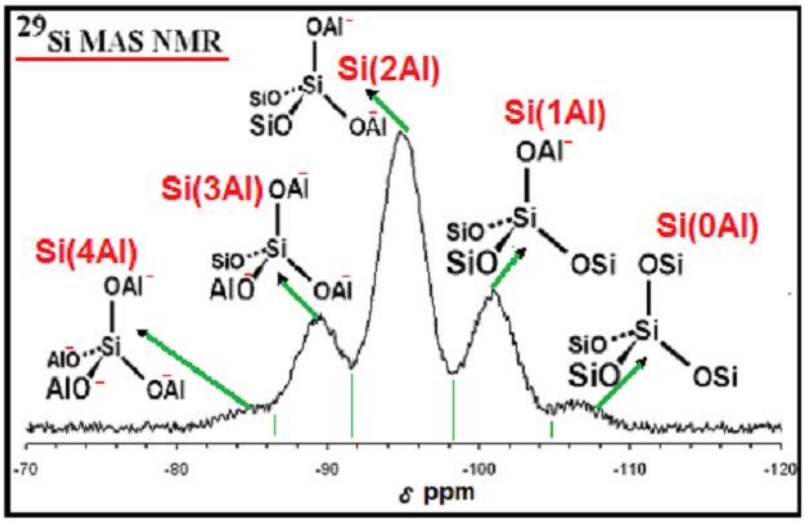

A.3. GAS ADSORPTION MEASUREMENT USING NITROGEN – BET ISOTHERM ANALYSIS

BET-surface area measurements are generally based on the phenomenon of gas adsorption-desorption isotherm [7]. The two processes are based on the same principle, but one is reversed to the other. The adsorption takes place when the gas molecules contact the surface of the solid material and a film of the adsorbate is formed. The gas atoms are taken up by the solid surface e.g. the accumulation of N_2 gas molecules on the zeolite surface. Adsorption is different to absorption, in which molecules diffuse into a liquid or solid to form a solution and that's why, it refers to a volume rather than a surface. In essence, the process simultaneously encompasses both adsorption and absorption is called sorption.

Irving Langmuir in 1920 published a theory to develop the sorption data, which is known as a Langmuir isotherm. The theory assumed that the adsorbed gas at a fixed temperature and gas pressure could be adsorbed from only one layer of adsorbate on the solid surface. In 1938, Brunauer, Emmett and Teller modified and optimized Langmuir's theory by using the hypothesis of multilayer gas adsorption. Thus, a new theory was evolved, which was called the BET isotherm. The pore structure and the total surface area, which includes all the internal structure of zeolite, can be calculated using BET method.

For surface area measurements, a BET isotherm is commonly used:

$$\frac{p}{(p_0 - p)V} = \frac{1}{cV_{mon}} + \frac{(c-1)p}{cV_{mon}\,p_0}$$

Where p and p_0 are the equilibrium and saturation pressures, V_{mon} is the volume of adsorbate required for forming a monolayer on the substrate surface, and c is the BET constant. c is a constant which is large when the enthalpy of desorption for the surface is larger than the enthalpy of desorption of the liquid adsorbate:

$$c = \exp\left(\frac{E_1 - E_L)}{RT}\right)$$

Where E_1 is the heat of adsorption of the first layer and E_L is the heat of adsorption of subsequent layers. By knowing the volume of adsorbed gas, which is required to form a monolayer on the surface and the area which each gas molecule occupies, one can calculate the surface area [6]. The adsorbates usually used for surface area measurements are nitrogen and argon that have a cross section of 0.162 nm^2 and 0.138 nm^2, respectively. In the case of zeolite materials, external and total surface areas are determined by collecting a BET isotherm for the sample before and after calcination. Internal surface area can then be calculated as the difference between the total and external surface areas.

The micropore volumes of zeolites can be determined using a t-plot method. This method consists of a comparison of the amount adsorbed with the statistical thickness of the adsorbed layer of a known reference isotherm at the same relative pressure. The total pore volume is calculated by measuring the volume of nitrogen adsorbed at p/p_0 near unity. At this relative pressure, adsorbate is assumed to be condensed inside the pores of the zeolite. The measured total pore volume of zeolite is larger than the micropore volume due to condensation of adsorbate in the intercrystalline voids between zeolite crystals, or, in the case of hierarchical zeolite, in the mesopores. Thus the total pore volume is often assumed to be the sum of micropore and mesopore volumes in the case of hierarchical zeolite materials. The distribution of pore volumes with respect to the pore size is called a pore size distribution.

For pore size distributions, the pore geometry, such as cylindrical, spherical or slit shape, needs to be taken into account. BJH model for pore size distribution

measurements assumes a cylindrically shaped pore. The BJH model assumes that condensation of adsorbate in pores of smaller diameter occurs at lower partial pressures and larger pores are filled with adsorbate as the pressure increases. Conversely, adsorbate desorbs from pores of larger size as the partial pressure decreases.

The shape of the adsorption or desorption branch may be mechanistically attributed to the pore structure of a solid. Such that the analysis of the adsorption-desorption hysteresis loop is essential in order to get a complete picture about the main structure of the pores in the sample. The formation of mesopores, less of micropores, within the structure normally gives rise to adsorption-desorption hysteresis loops.

A representative nitrogen sorption isotherm is shown in **Figure A.3**. The first data points of the adsorption branch are used for BET surface area calculation. The highest adsorption point is used for calculations of the total pore volume. For pore size distribution modeling the adsorption, desorption or both curves can be used depending on the model. The *t*-plot micropore volume calculation uses the low and mid-pressure section of the adsorption branch.

Figure A.3. A representative nitrogen sorption isotherm. The main information that can be obtained from the isotherm is indicated.

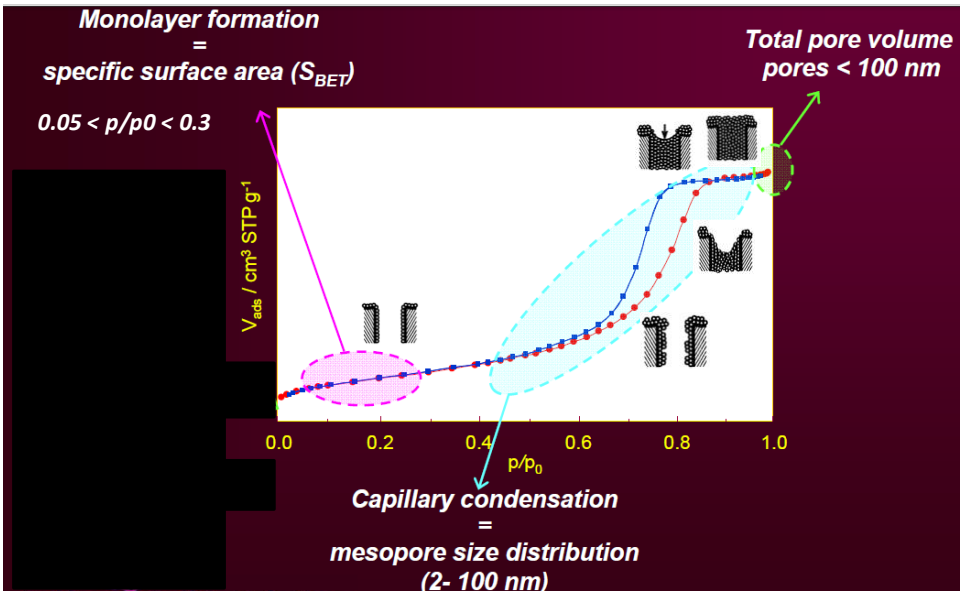

A.4. TEMPERATURE PROGRAMMED DESORPTION OF AMMONIA (NH_3-TPD) ANALYSIS

This method is one of the several techniques that can be utilized to characterize the total acidity of zeolite samples. However, this technique cannot differentiate between Brönsted and Lewis acid sites.

During the TPD analysis, the acid sites are saturated with a NH_3. Due to its small molecular dimensions (0.37 nm × 0.40 nm × 0.31 nm) – this probe can simply pass through windows greater than 0.4 nm such as in zeolite Y.

The NH_3-TPD curve generally consists of two peaks, a low temperature peak and a high temperature peak. Nevertheless such peaks cannot be clearly resolved for all kinds of zeolite materials. An indicating value of the number of acid sites can be mathematically obtained by integrating the area under the peaks, as this area is proportional to the number of adsorbed ammonia molecules. The low temperature peak can be used to represent the desorption of ammonia from the weak acid sites (i.e. aluminum species or hydrogen bridging bonds). Thus, the area under low temperature peak consists of physisorbed ammonia physically bonded ammonia to the sample. The high temperature peak can be used to represent the desorption of ammonia molecules from the strong acid sites (i.e. protonic acidity). Thus, the area under the high temperature peak consists of chemisorbed ammonia.

A.5. INDUCTIVELY COUPLED PLASMA - OPTICAL EMISSION SPECTROSCOPY

Elemental composition of zeolite materials can be quantified by using the Inductively Coupled Plasma - Optical Emission Spectroscopy (ICP-OES) technique. The basis for ICP-OES is using a high power radio frequency signal to generate an electromagnetic field in which a carrier gas (typically argon) is ionized and converted into a plasma state with temperatures of several thousand Kelvins. Then a studied solution is injected in the plasma beam and the atoms are excited and emit electromagnetic radiation, usually in UV and visible ranges. The emitted photons are then detected using a photomultiplier tube or a charge-coupled device (CCD) detector. In the resulting spectrum, the intensity of the wavelengths is compared with the intensities produced by standards with known concentrations of the studied element and its concentration in the analyzed solution is calculated.

For ICP-OES measurements, solid materials need to be dissolved first. In the case of zeolites, the solids are dissolved using a hydrofluoric acid solution, and then the solution is neutralized with boric acid to prevent the loss of silicon which forms volatile SiF_4. Standard solutions of the studied elements, are then prepared, either separately or, in case of their compatibility, in mixtures. The instrument is calibrated using the standards and the samples are then analyzed.

A.6. TRANSMISSION ELECTRON MICROSCOPY (TEM)

Electron microscopy (EM) is another powerful tool for studying zeolite materials. Parameters, such as particle size and shape, surface morphology, degree of aggregation presence of other phases, distribution of metal or metal oxide clusters and more can be determined using scanning and transmission electron microscopes. Electron microscopes operate using principles similar to those used in light microscopy. The advantage of EM is that the wavelength of electrons is much smaller than the wavelength of visible light, which results in much higher achievable resolutions and allow obtaining images of nanoscale specimen. The beam of electrons is generated using an electron gun and then passes through a series of magnetic lenses and apertures in order to obtain a well-focused beam, which "illuminates" the sample. In transmission electron microscopy (TEM) the beam passes through the sample deposited on a thin metal grid typically coated with a thin layer of carbon and reaches the detector. The image collected in bright field imaging mode gives contrast information about the sample, in which thicker areas or areas with higher atomic number will be darker and vice versa.

A.7. FOURIER TRANSFORM INFRARED SPECTROSCOPY (FTIR)

Fourier Transform Infrared spectroscopy is the spectroscopy that deals with the infrared region of the electromagnetic spectrum [8-11], which is light with a longer wavelength and lower frequency than visible light. It covers a range of techniques, mostly based on absorption spectroscopy. As with all spectroscopic techniques, it can be used to identify and study chemicals. For a given sample which may be solid, liquid, or gaseous, the method or technique of infrared spectroscopy uses an instrument called an infrared spectrometer (or spectrophotometer) to produce an infrared spectrum. A basic IR spectrum is essentially a graph of infrared light absorbance (or transmittance) on the

vertical axis vs. frequency or wavelength on the horizontal axis. Typical units of frequency used in IR spectra are reciprocal centimeters (usully called wave numbers), with the symbol cm^{-1}. A common laboratory instrument that uses this technique is a Fourier transform infrared (FTIR) spectrometer. The term Fourier transform infrared spectroscopy originates from the fact that a Fourier transform (a mathematical process) is required to convert the raw data into the actual spectrum.

The most common form of the technique is transmission infrared spectroscopy, in which the sample consists typically of 10 to 100 mg of catalyst, pressed into a self-supporting disk of approximately 1 cm^2 and a few tenths of a millimeter thickness [9, 11].

FTIR spectroscopy is the most direct method to study type, density and acidity of hydroxyl groups in zeolites [2]. The frequency of the stretching vibration of a hydroxyl group (νOH) is a function of the force constant between the O and H atoms and, thus, reflects the type and, at least in a homologous series, the acid strength of the hydroxyl group. In such a series of hydroxyl groups a weaker O-H bond, i.e., a more acidic hydroxyl group, is reflected by a lower stretching frequency.

An application of FTIR in the characterization of zeolites results from the fact that the wavenumber of an O-H stretching vibration is strongly influenced by (i) the type of coordination of the oxygen (terminal versus bridging oxygen), (ii) the structural environment of the hydroxyl group, i.e., the type of zeolite lattice, and (iii) the perturbation of the OH group through the surroundings by lattice or extra-lattice oxygen. Two types of silanol groups (Si-OH groups) are usually present on zeolites:

(i) OH groups on the outer surface terminating the zeolite crystal (**Figure A.4**):

Figure A.4. Schematic representation of terminal silanol groups [2].

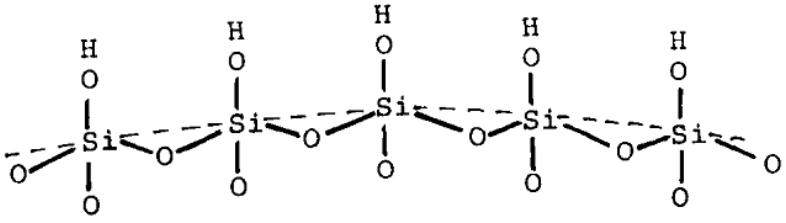

(ii) OH groups on structural defects resulting from an incomplete condensation or from the removal of lattice atoms (**Figure A.5**). One type of silanol groups is formed when a

Si-0-Si bond is broken by a reaction with water. This type of silanol groups is always present as pairs. Silanol groups can be formed if a T-atom is missing in the structure. This type of defect leads to a cluster of four silanol groups or a so-called hydroxyl nest (**Figure A.6**).

Figure A.5. Silanol groups formed when a Si-0-Si bond is broken by a reaction with water [2]

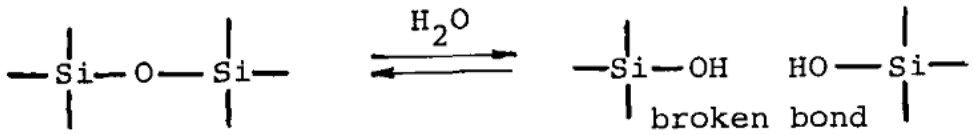

Figure A.6. Silanol groups forming a hydroxyl nest [2].

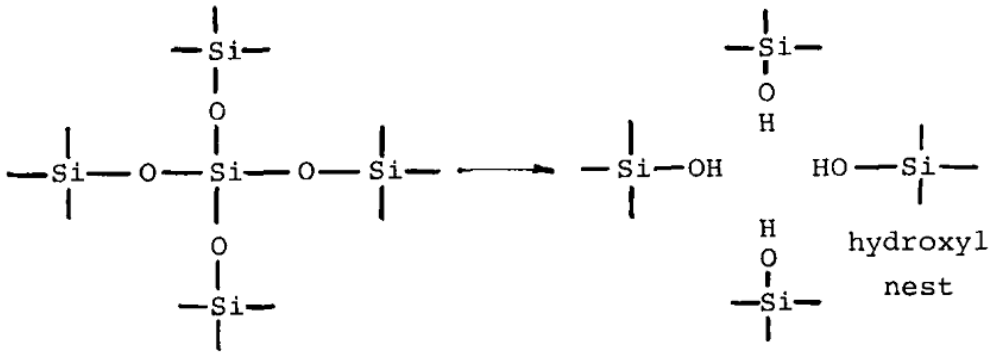

The frequency of the OH stretching vibrations of silanol groups on the external surface is in the range of 3740-3745 cm^{-1}, while that of silanol groups related to defects depends on their local environment [1]. The presence of hydrogen bonding interactions shifts the frequency to 3500 cm^{-1}, while isolated silanol groups are only slightly shifted to lower frequencies, i.e., 3735-3715 cm^{-1}, compared to the silanol groups on the external surface. Silanol groups on the external surface are always observed in the IR spectra of zeolites. Their relative intensity depends on the primary size of the zeolite particles, i.e., samples with a large particle size show a relatively low intensity of the Si-OH groups on the external surface and vice versa.

Hydroxyl protons acting as Brønsted acid sites, i.e., as proton donors, are located on oxygen bridges connecting a tetrahedrally coordinated silicon and aluminum cation on framework positions. These OH groups are commonly referred to as structural or

bridging OH groups (Si-(OH)-Al) [12]. In aluminosilicate-type zeolites, the 4+ charge on framework silicon atoms and the 2- charges on the four coordinating oxygen atoms lead to neutral framework tetrahedra ($SiO_{4/2}$). If, however, the silicon cation in the framework is substituted by a cation with a 3+ charge, typically with an aluminum cation, the formal charge on that tetrahedron changes from neutral to 1-($A10_{4/2}^{-}$). This negative charge is balanced by a metal cation or a hydroxyl proton forming a weak Lewis acid site or a strong Brønsted acid site, respectively. Bridging hydroxyl groups are observed on most types of zeolites between 3650 and 3550 cm^{-1}.

A.8. X-RAY PHOTOELECTRON SPECTROSCOPY (XPS)

XPS is among the most frequently used techniques in catalysis. This technique uses electrons as information carriers. In X-ray photoelectron spectroscopy, the sample is exposed under ultra high vacuum conditions to a monochromatic X-ray radiation, typically produced by MgKα (1253.6 eV) or A1Kα (1486.3 eV) radiation and the energy spectrum of the ejected primary electrons is measured. X-ray photons ionizes core or valence band levels, and the kinetic energy E_k of the emitted photoelectrons is quantified [1]. The energy balance is given by:

$$E_k = h\nu - E_b - \phi$$

This equation permits the electron-binding energy E_b (relative to the Fermi level) to be measured when the photon energy hν and the work function ø of the spectrometer are known. The binding energies are characteristic for each chemical element and, therefore, XPS can be used to analyze the composition of the sample. This technique has also been named ESCA (electron spectroscopy for chemical analysis). The probing depth of XPS varies between 1.5 and 6 nm according to the mean free path of the photoelectrons and, thus depends on the element being probed. The energy levels of the core electrons depend on the chemical state and environment of the atoms. Thus, the binding energies are not only element-specific, but also contain information on the (partial) charge of the elements.

A.9. UV-VIS DIFFUSED REFLECTANCE SPECTROSCOPY (DRS)

Reflectance spectroscopy is very closely related to UV-Vis spectroscopy, in that both of these techniques use visible light to excite valence electrons to empty orbitals. The difference in these techniques is that in UV-Vis spectroscopy one measures the relative change of transmittance of light as it passes through a solution, whereas in diffuse reflectance, one measures the relative change in the amount of reflected light off of a surface.A solution that is completely clear and colorless has essentially 100% transmission of all visible wavelengths of light, which means that it does not contain any dissolved components that have (allowed) electronic transitions over that energy range. By the same line of reasoning, a white powder effectively reflects 100% of all visible wavelengths of light that interacts with it. However, if the material has electronic energy levels that are separated by an energy in the visible region, then it may absorb some of light energy to move electrons from the filled energy level (valence band) into this empty level (conduction band). This causes a relative decrease in the amount of light at that particular energy, relative to a reference source. In other words, the % transmission/reflectance will decrease.

Fig A.7. presents the common setup for UV-Vis DRS measurements. With integrating spheres, measurement is performed by placing the sample in front of the incident light window, and concentrating the light reflected from the sample on the detector using a sphere with a barium sulfate-coated inside. The obtained value becomes the reflectance (relative reflectance) with respect to the reflectance of the reference standard white board, which is taken to be 100%. When light is directed at the sample at an angle of 0°, specular reflected light exits the integrating sphere and is not detected. As a result, only diffuse reflected light is measured.

A.10. LASER RAMAN SPECTROSCOPY

Whilst in infrared spectroscopy a molecule absorbs photons with the same frequency as its vibrations, Raman spectroscopy – in contrast – is based on the inelastic scattering of photons, which lose energy by exciting vibrations in the sample [9]. The scattering process is illustrated schematically in **Figure A.8**. In this process, monochromatic light of frequency ν_0 falls onto a sample, where the majority of the photons undergoes

Rayleigh scattering (i.e., scattering without energy exchange) [9]. In a quantum mechanical picture it is as if the molecule is excited to an unstable state with energy $h\nu_0$ above the ground state, from which it decays back to the ground state. No energy is exchanged between the molecule and the photon. However, when the excited molecule decays to the first vibrational level with frequency ν_{vib}, it effectively takes an amount of energy equal to $h\nu_{vib}$ away from the photon. Hence, the scattered light exhibits intensity at the frequency $\nu_0 - \nu_{vib}$; this Raman peak is called the ‘‘Stokes band’’. If the collision with a photon brings a vibrationally excited molecule to the unstable state of energy $h\nu_0 + h\nu_{vib}$, it may decay to the ground state, transferring a net amount of energy $h\nu_{vib}$ to the photon, which leaves the sample with a higher frequency equal to $\nu_0 + \nu_{vib}$. This peak, which is termed the ‘‘anti-Stokes band’’, has much lower intensity than the Stokes band, because the fraction of vibrationally excited molecules is usually small.

Figure A.7. Measurement of Diffuse reflection including specular reflection using an integrating sphere.

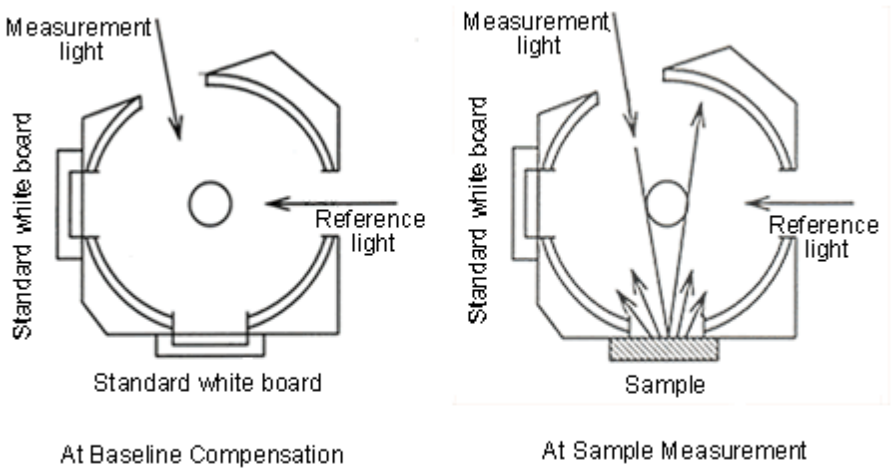

Raman spectroscopy provides insight into the structure of oxides, their crystallinity, the coordination of metal oxide sites, and even the spatial distribution of phases through a sample, when the technique is used in microprobe mode. As the frequencies of metal–oxygen vibrations in a lattice are typically found to range between a few hundred and 1000 cm^{-1}, and thus are difficult to investigate with infrared spectroscopy, the Raman approach is clearly the best for this purpose. Molybdenum, being a constituent of many

hydrotreating and partial oxidation catalysts, is among those elements most studied by Raman spectroscopy.

Figure A. 8. The Raman effect. Monochromatic light of frequency ν_0 is scattered by a sample, either without losing energy (Rayleigh band) or inelastically, in which a vibration is excited (Stokes band), or a vibrationally excited mode in the sample is de-excited (anti-Stokes band) [9].

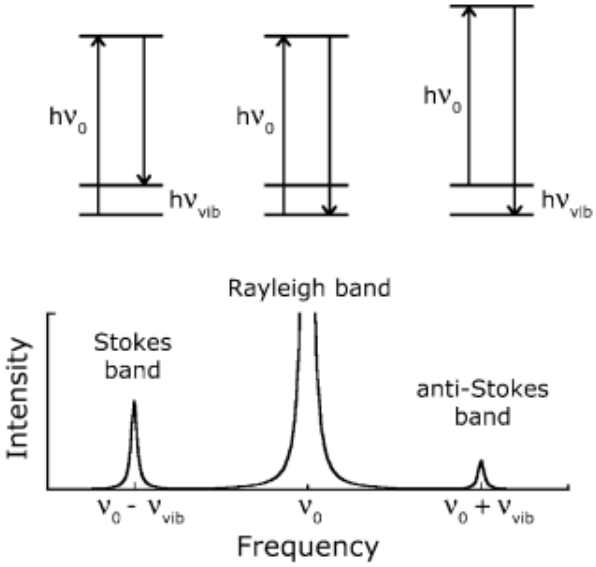

APPENDIX B.

FTIR SPECTRA OF THE ZEOLITE SAMPLES IN THE REGION OF THE BANDS ASSOCIATED TO BRØNSTED AND LEWIS ACID SITES AFTER ADSORPTION AND DESORPTION OF PYRIDINE

B.1. FTIR SPECTRA OF ZEOLITES OF CHAPTER 2.

Figure B.1. FTIR spectra of the zeolite samples of chapter 1 in the region of the bands associated to Brønsted and Lewis acid sites, after adsorption of pyridine at 150 °C and subsequent desorption for 1 h at 150 °C, 300 °C and 500 °C. Spectra are shown after subtraction of the spectrum of the corresponding calcined sample.

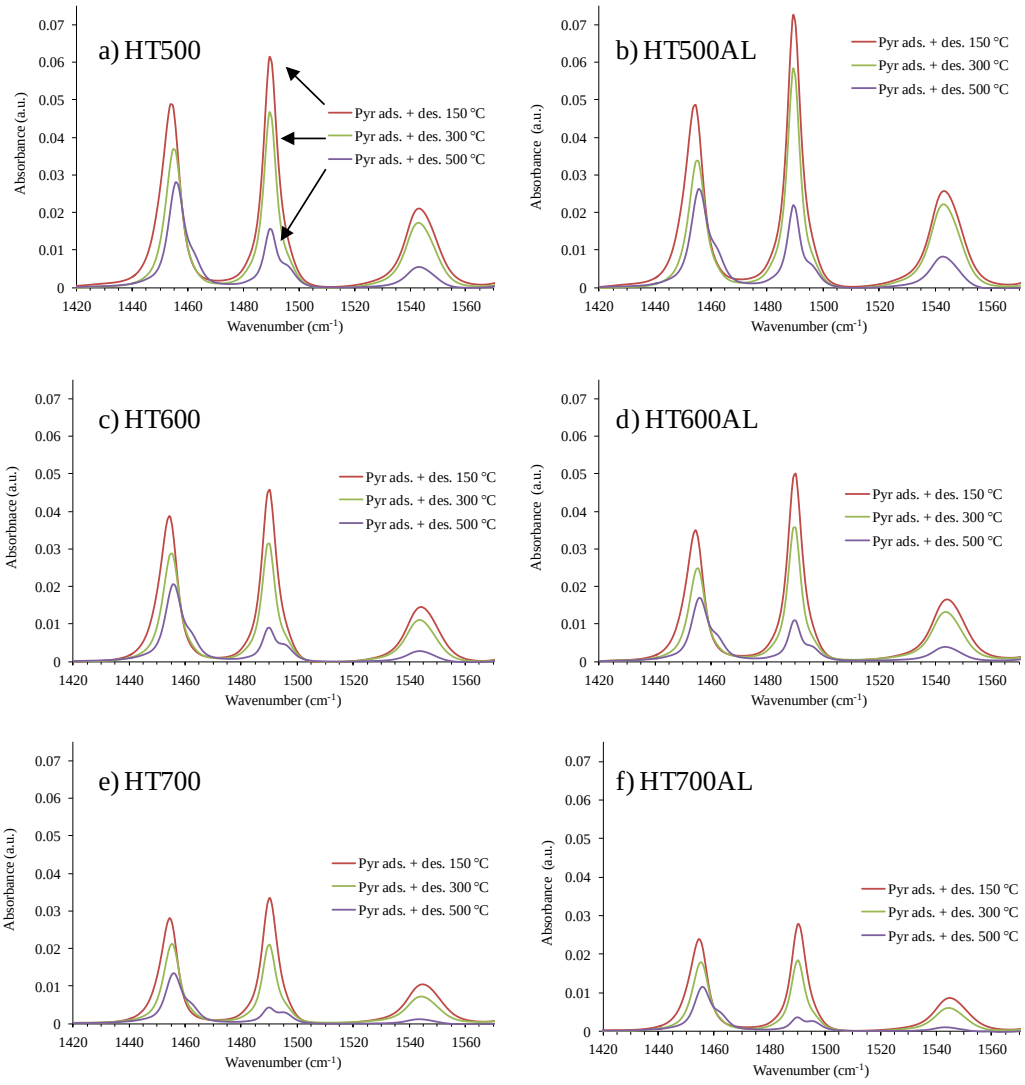

B.2. FTIR SPECTRA OF ZEOLITES OF CHAPTER 3.

Figure B.2. FTIR spectra of the zeolite samples of chapter 3 in the region of the bands associated to Brønsted and Lewis acid sites, after adsorption of pyridine at 150 °C and subsequent desorption for 1 h at 150 °C, 300 °C and 500 °C. Spectra are shown after subtraction of the spectrum of the corresponding calcined sample.

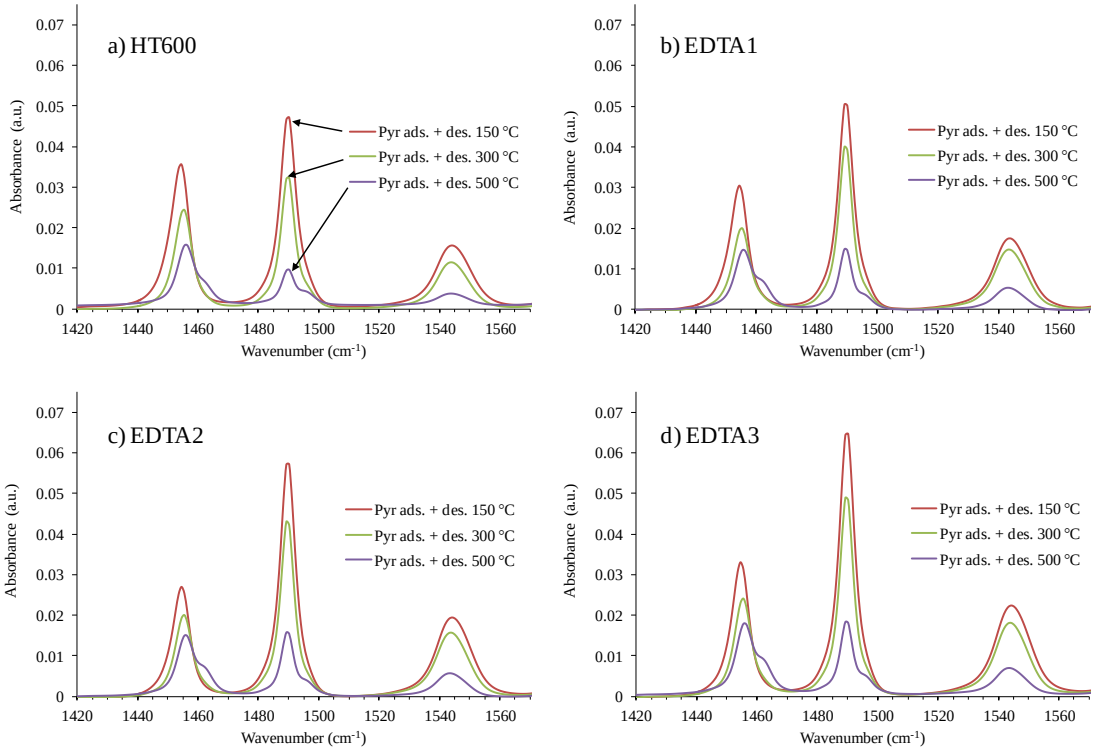

B.3. FTIR SPECTRA OF ZEOLITES OF CHAPTER 4.

Figure B.3. FTIR spectra of the zeolite samples of chapter 4 in the region of the bands associated to Brønsted and Lewis acid sites, after adsorption of pyridine at 150 °C and subsequent desorption for 1 h at 150 °C, 300 °C and 500 °C. Spectra are shown after subtraction of the spectrum of the corresponding calcined sample.

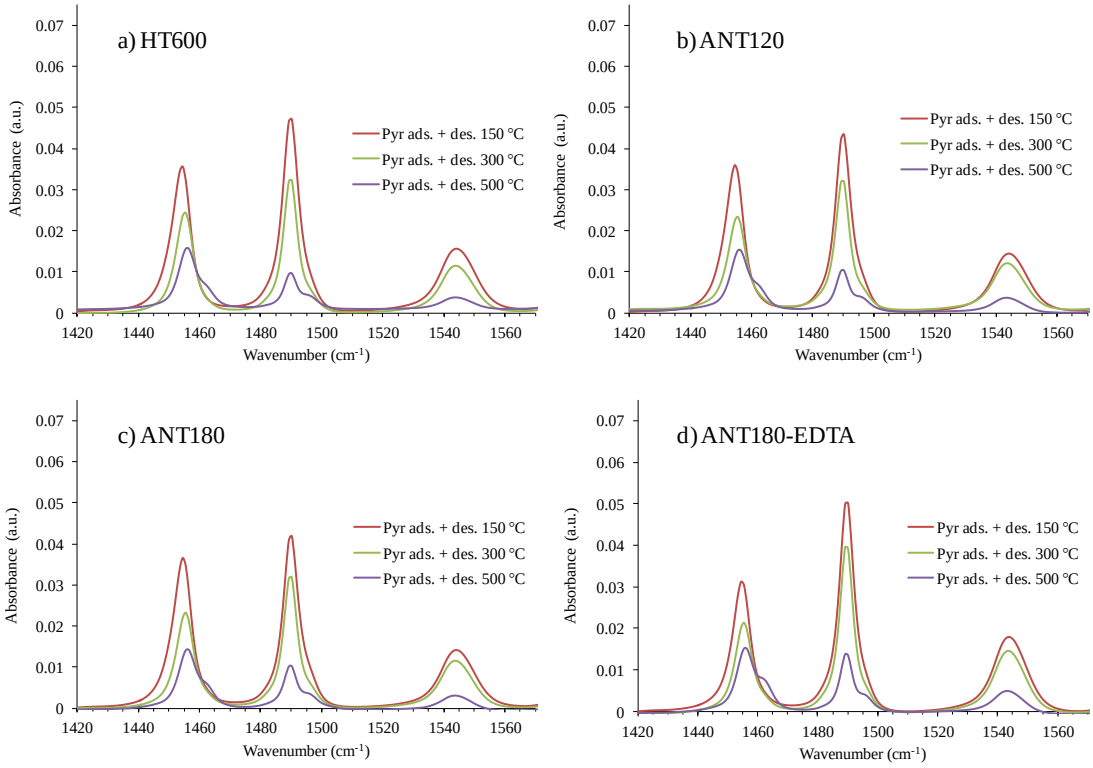

APPENDIX C

CHARACTERIZATION RESULTS FOR NIMOP-SUPPORTED CATALYSTS OF CHAPTER 3

C.1. UV-VIS DRS SPECTROSCOPY

Figure C.1. UV-Vis DRS spectra of the supported NiMoP catalysts in oxide form. a) NiMoP/(HT600+Alumina), b) NiMoP/(EDTA1+Alumina), c) NiMoP/(EDTA2+Alumina) and d) NiMoP/(EDTA+Alumina). The inset shows a magnification in the 550 – 800 nm region.

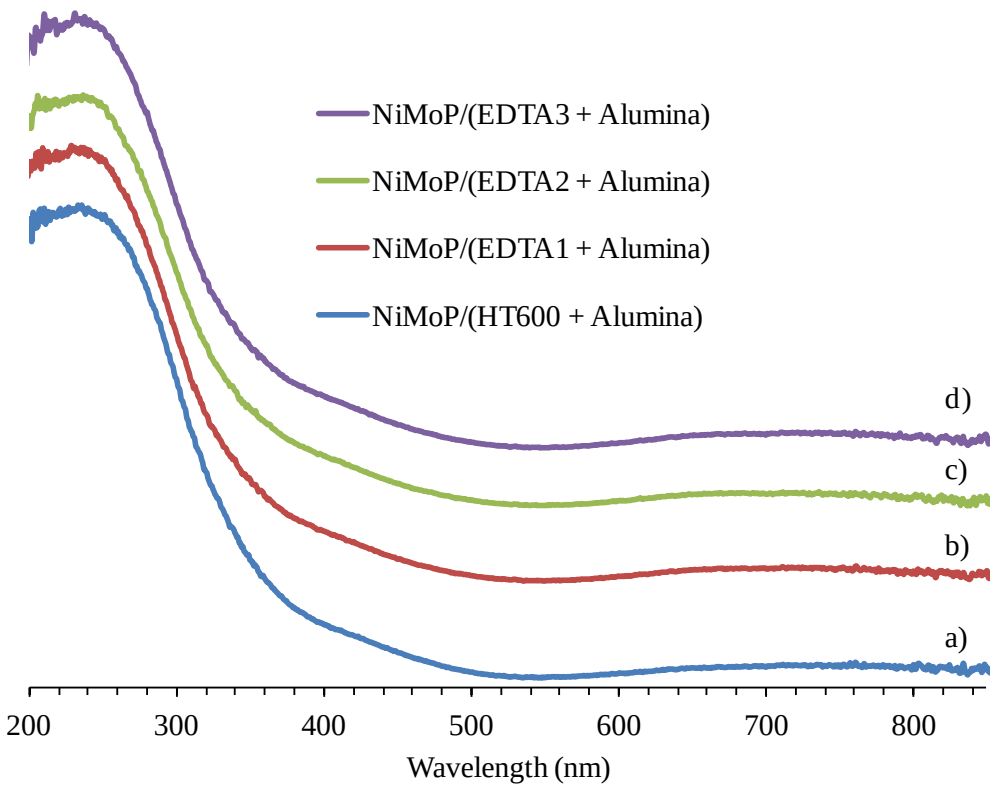

C.2. LASER RAMAN SPECTROSCOPY (LRS)

Figure C.2. Laser Raman spectra of the NiMoP supported catalysts (oxide state). a) NiMoP/(HT600 + Alumina), b) NiMoP/(EDTA1 + Alumina), c) NiMoP/(EDTA2 + Alumina), d) NiMoP/(EDTA3 + Alumina).

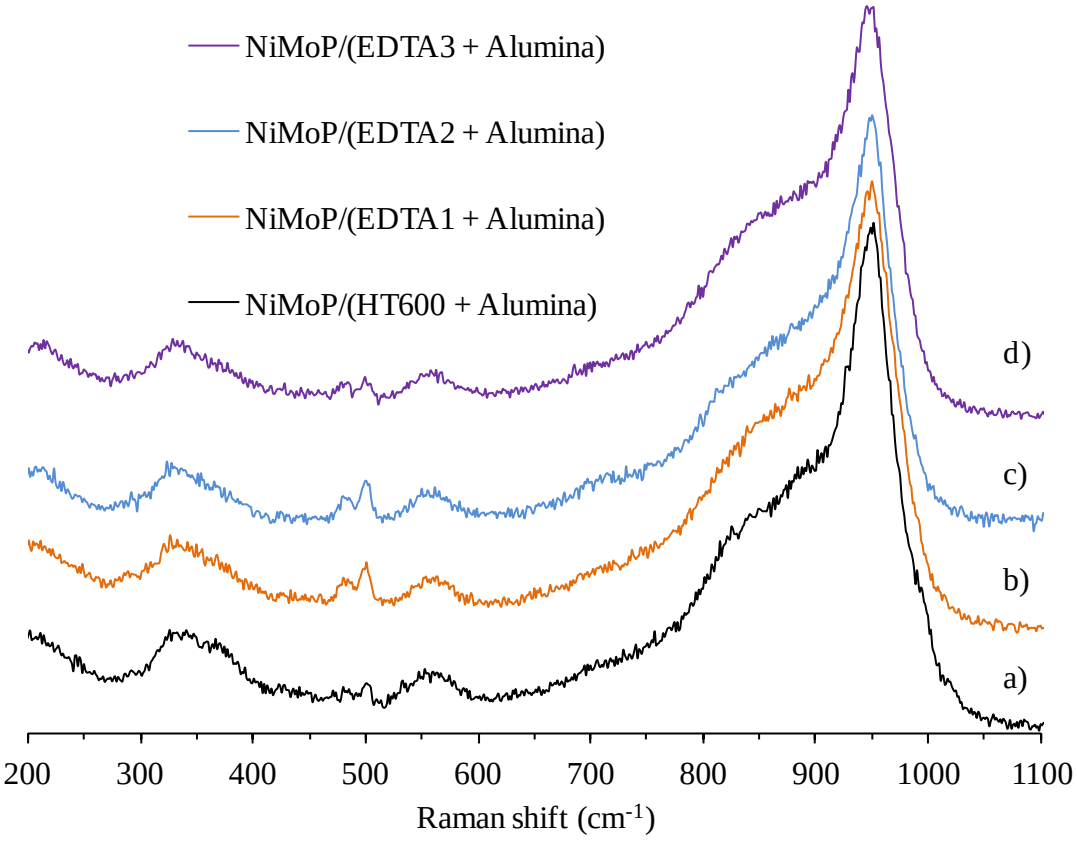

C.3. XPS SPECTROSCOPY OF SULFIDED NIMOP CATALYSTS

Figure C.3. XPS Mo 3d spectra of the NiMoP sulfide catalysts: (a) NiMoP/(HT600+Alumina), b) NiMoP/(EDTA1+Alumina), c) NiMoP/(EDTA2+Alumina), d) NiMoP/(EDTA3+Alumina). The spectra were decomposed into oxide, oxysulfide and sulfide components, as shown in a).

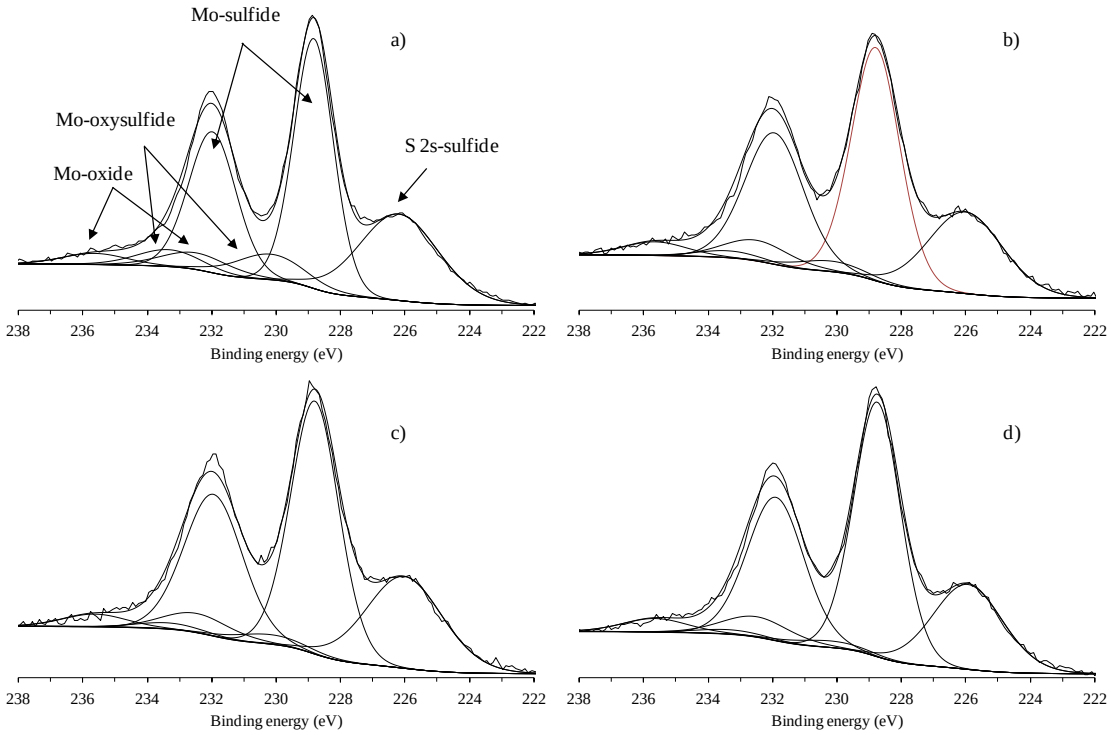

Figure C.4. XPS Ni 2p spectra of the NiMoP sulfide catalysts: a) NiMoP/(HT600+Alumina), b) NiMoP/(EDTA1+Alumina), c) NiMoP/(EDTA2+Alumina), d) NiMoP/(EDTA3+Alumina).

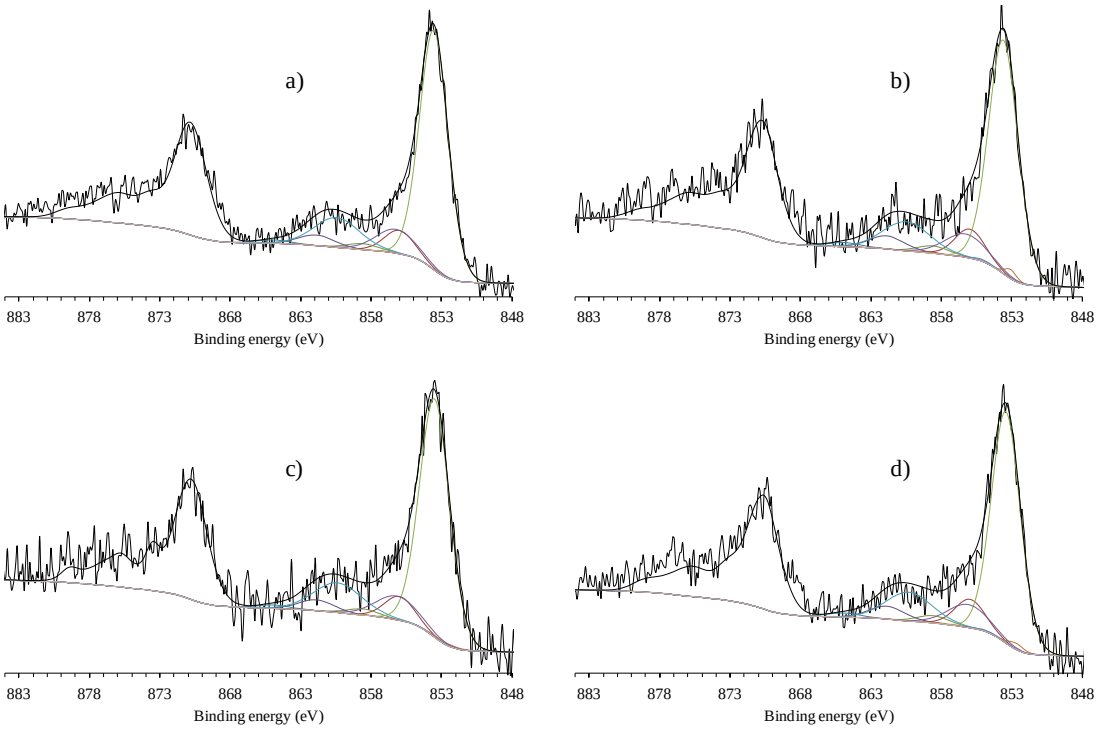

Table C.1. XPS parameters of the different contributions Mo 3d and Ni 2p obtained for supported NiMoP catalysts in sulfided state.

		NiMoP/(HT600+Alumina)	NiMoP/(EDTA1+Alumina)	NiMoP/(EDTA2+Alumina)	NiMoP/(EDTA3+Alumina)
Mo^{IV}	BE (eV)	228.8	228.8	228.8	228.8
	at%	78	85	87	87
Mo^{V}	BE (eV)	230.2	230.2	230.2	230.2
	at%	13	5	4	3
Mo^{IV}	BE (eV)	232.5	232.5	232.5	232.5
	at%	9	10	9	10
NiMoS phase	BE (eV)	853.6	853.6	853.5	853.4
	at%	88	84	87	84
NiSx	BE (eV)	852.7	853.1	852.7	852.7
	at%	0	2	1	1
Ni^{II}-Oxide	BE (eV)	856.0	856.0	856.0	856.0
	at%	12	14	12	15
Mo/Ni		6.4	6.2	6.3	6.4
S/Mo		2.5	2.4	2.5	2.5

APPENDIX D.
CHARACTERIZATION RESULTS FOR NIMOP-SUPPORTED CATALYSTS OF CHAPTER 4

D.1. UV-VIS DRS SPECTROSCOPY

Figure D.1. UV-Vis DRS spectra of the supported NiMoP catalysts in oxide form. a) NiMoP/(HT600 + Alumina), b) NiMoP/(ANT120 + Alumina), c) NiMoP/(ANT180 + Alumina). Data not available for NiMoP/(ANT180-EDTA + Alumina) catalyst.

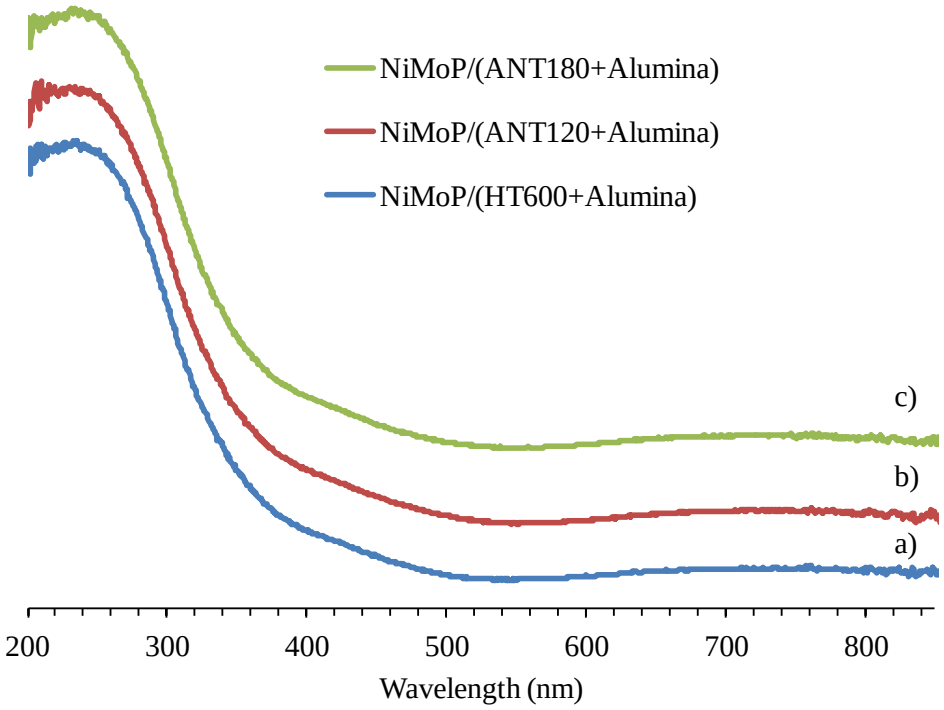

D.2. LASER RAMAN SPECTROSCOPY (LRS)

Figure D.2. Laser Raman spectra of the NiMoP supported catalysts (oxide state). a) NiMoP/(HT600 + Alumina), b) NiMoP/(ANT120 + Alumina), c) NiMoP/(ANT180 + Alumina). Data not available for NiMoP/(ANT180-EDTA + Alumina) catalyst.

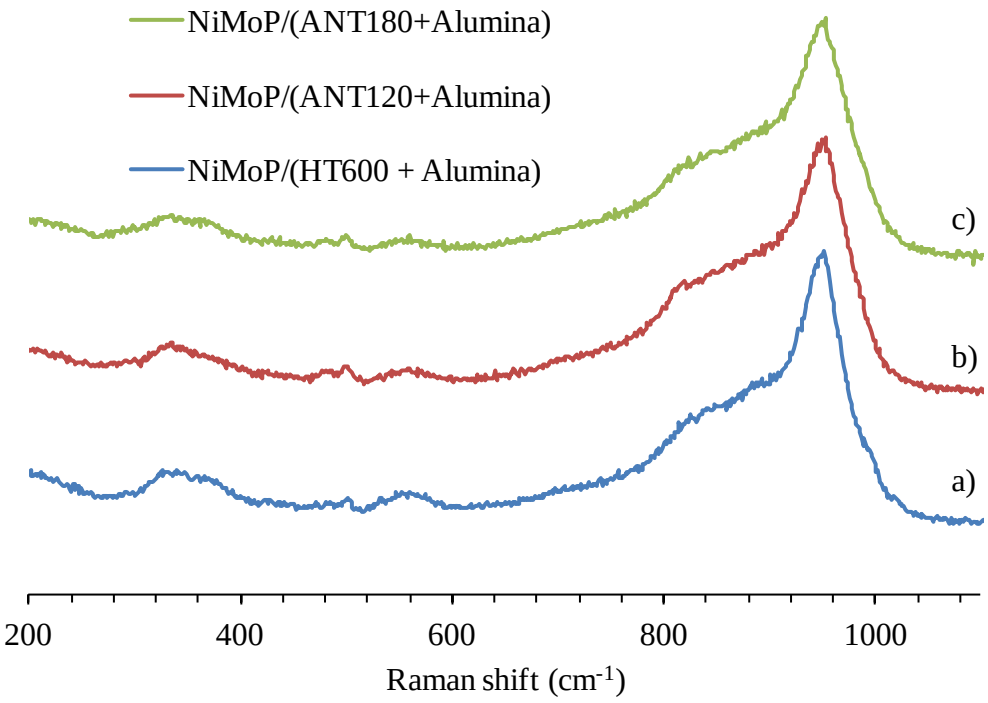

D.3. XPS SPECTROSCOPY OF SULFIDED NIMOP-SUPPORTED CATALYSTS

Figure D.3. XPS Mo 3d spectra of the NiMoP sulfide catalysts: a) NiMoP/(HT600+Alumina), b) NiMoP/(ANT120+Alumina), c) NiMoP/(ANT180+Alumina). The spectra were decomposed into oxide, oxysulfide and sulfide components, as shown in a). Data not available for NiMoP/(ANT180-EDTA + Alumina) catalyst.

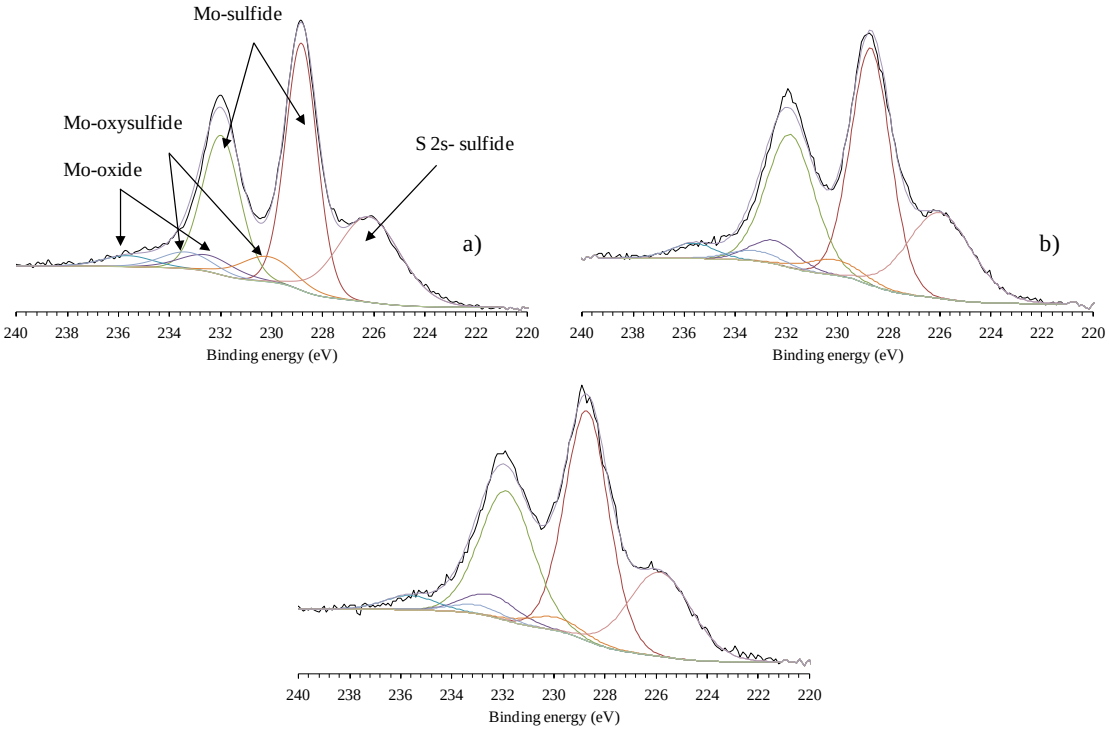

Figure D.4. XPS Ni 2p spectra of the NiMoP sulfide catalysts: a) NiMoP/(HT600+Alumina), b) NiMoP/(ANT120+Alumina), c) NiMoP/(ANT180+Alumina). Data not available for NiMoP/(ANT180-EDTA + Alumina) catalyst.

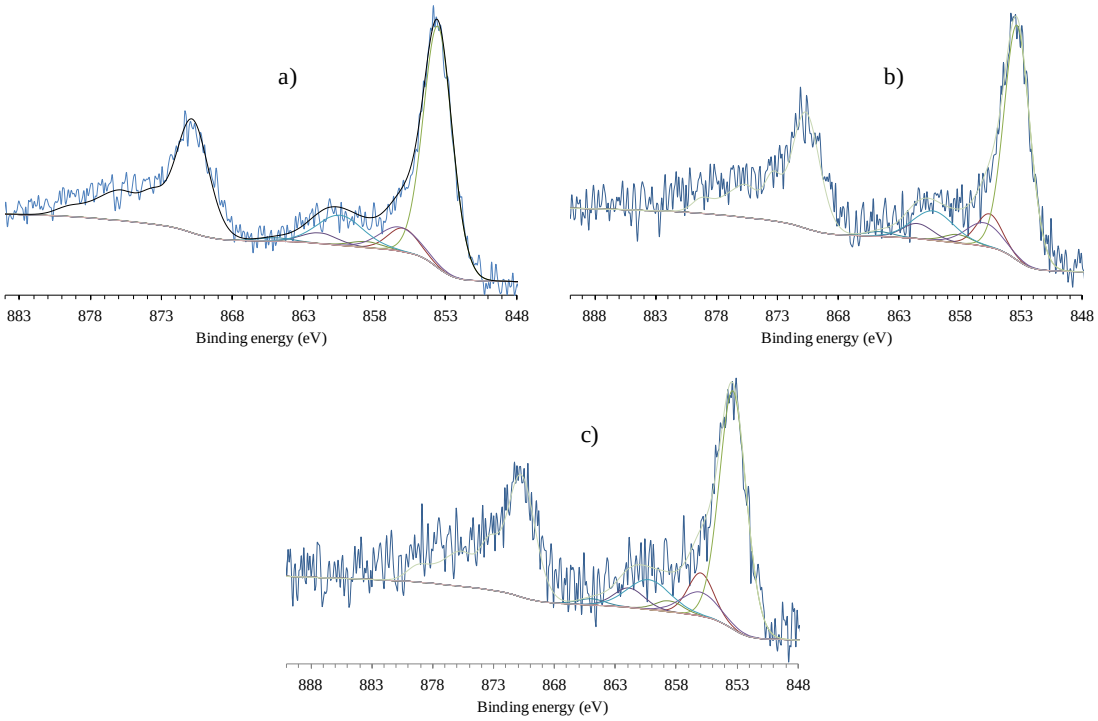

Table D.1. XPS parameters of the different contributions Mo 3d and Ni 2p obtained for supported NiMoP catalysts in sulfided state.

		NiMoP/(HT600+Alumina)	NiMoP/(ANT120+Alumina)	NiMoP/(ANT180+Alumina)
Mo^{IV}	BE (eV)	228.8	228.7	228.7
	at%	78	83	85
Mo^{V}	BE (eV)	230.2	230.1	229.9
	at%	13	7	6
Mo^{IV}	BE (eV)	232.5	232.5	232.5
	at%	9	9	10
NiMoS phase	BE (eV)	853.6	853.3	0.0
	at%	88	83	80
NiSx	BE (eV)	852.7	852.7	853.1
	at%	0	0	0
Ni^{II}-Oxide	BE (eV)	856.0	855.6	856.0
	at%	12	16	19
Mo/Ni		6.4	6.6	6.5
S/Mo		2.5	2.5	2.4

REFERENCES

[1] A. Jentys, J. Lercher, Studies in Surface Science and Catalysis 137 (2001) 345-386.

[2] J.H.C. van Hooff, J.W. Roelofsen, in: E.M.F. H. van Bekkum, J.C. Jansen (Eds.), Studies in Surface Science and Catalysis, Elsevier, 1991, pp. 241-283.

[3] B.Y.S. Al-zaidi, The effect of modification techniques on the performance of zeolite-Y catalysts in hydrocarbon cracking reactions, PhD thesis dissertation, University of Manchester, 2011.

[4] J. Als-Nielsen, D. McMorrow, Elements of modern X-ray physics, John Wiley & Sons, 2011.

[5] C. Suryanarayana, M.G. Norton, X-ray diffraction: a practical approach, Cambridge Univ Press, 1998.

[6] A. Petushkov, Synthesis and characterization of nanocrystalline and mesoporous zeolites, PhD thesis dissertation. The University of Iowa, 2011.

[7] J. Rouquerol, F. Rouquerol, P. Llewellyn, G. Maurin, K.S. Sing, Adsorption by powders and porous solids: principles, methodology and applications, Academic press, 2013.

[8] J. Weitkamp, L. Puppe, Catalysis and zeolites: fundamentals and applications, Springer Science & Business Media, 1999.

[9] J.W. Niemantsverdriet, Spectroscopy in catalysis, John Wiley & Sons, 2007.

[10] G. Leofanti, G. Tozzola, M. Padovan, G. Petrini, S. Bordiga, A. Zecchina, Catalysis today 34 (1997) 307-327.

[11] J. Ryczkowski, Catalysis Today 68 (2001) 263-381.

[12] J. Weitkamp, M. Hunger, Acid and base catalysis on zeolites, Elsevier: Amsterdam, The Netherlands, 2007, pp. 787-835.